Atmospheric Pressure Spatial Atomic Layer Deposition of Metal Oxides for Different Applications

by

Poojitha Durgamahanti

A thesis

presented to the University of Waterloo

in fulfillment of the

thesis requirement for the degree of

Master of Applied Science

in

Mechanical and Mechatronics Engineering

Waterloo, Ontario, Canada, 2024

© Poojitha Durgamahanti 2024

Author's Declaration

This thesis consists of material all of which I authored or co-authored: see Statement of Contributions included in the thesis. This is a true copy of the thesis, including any required final revisions, as accepted by my examiners.

I understand that my thesis may be made electronically available to the public.

Statement of Contributions

I, Poojitha Durgamahanti was the main author for all chapters, which were written under the supervision of Dr. Kevin Musselman. Chapter 1 and 2 were not written for publication. Chapter 3 and chapter 4 are currently being prepared for submission to journals. I conceptualized the project, deposited and optimized silicon oxide thin films and performed atomic force microscopy (AFM) measurements. Exceptions to sole authorship of material are as follows:

- Craig A. Wheaton and Kerim Samedov synthesized diisopropylaminosilane (DIPAS) precursor for the silicon oxide depositions.
- Osamah Kharsah synthesized the MoS_2 via atmospheric-pressure chemical vapor deposition under the supervision of Dr. Marika Schleberger.
- André Maas synthesized the WS_2 via atmospheric-pressure chemical vapor deposition under the supervision of Dr. Marika Schleberger.
- Jixi Zhang assisted with the Raman and PL measurements under the supervision of Dr. Rodney Smith.
- Farman Ullah assisted with the ZnO depositions using an atmospheric-pressure spatial atomic layer deposition system.
- Yasaman Jarrahizadeh synthesized exfoliated WS_2 samples under the supervision of Dr. Axel Lorke.

Abstract

Atmospheric-pressure spatial atomic layer deposition (AP-SALD) is an emerging technique for the rapid, open-air deposition of metal-oxide thin films. In this thesis, I study two metal oxides, namely silicon oxide and zinc oxide, for use in two different applications.

Silicon oxide (SiO_x) is first studied. It is a highly versatile material used in different applications. However, its conventional growth and deposition methods often require very high temperature or the use of plasma. In this thesis, I present a plasma-free, low-temperature process for depositing high-quality SiO_x thin films using AP-SALD. An aminodisilane precursor, diisopropylaminosilane ($SiH_3N(C_3H_7)_2$, DIPAS), was synthesized and tested with different oxidants such as ozone and 30% hydrogen peroxide aqueous solution. Initial attempts with hydrogen peroxide solution resulted in precursor condensation and the formation of nano crystallite SiO_x contaminated with organic molecules, indicating that the deposition process is oxidant limited. In contrast, using ozone as the oxidant facilitated the deposition of high quality amorphous SiO_x films. The microstructure was highly dependent on the deposition temperature, transitioning from nano crystallites at lower temperatures to amorphous films at temperatures of 70°C to 100°C. X-ray photoelectron spectroscopy (XPS) confirmed the deposition of continuous SiO_x films at 70°C or above using ozone, and the growth per cycle was ~1 Å/cycle, consistent with atomic layer deposition (ALD) of SiO_x. This work shows that high-quality SiO_x films can be produced by AP-SALD using DIPAS and ozone, without the aid of plasma or any surface functionalization, at low growth temperatures (T >= 70°C).

For the second study, I investigate the nucleation and growth mechanism of ZnO on different 2D materials. Uniform deposition of metal oxides on 2D materials is a crucial step to realize the integration of 2D materials in practical devices. In this study, I investigate the nucleation and growth of ZnO on 2D transition metal dichalcogenides, specifically MoS_2 and WS_2. The ZnO depositions were carried out using an atmospheric-pressure spatial atomic layer deposition system operated in atmospheric-pressure spatial chemical vapor deposition (AP-SCVD) mode at 100°C. The nucleation of ZnO was found to be different on MoS_2 and WS_2, whereby the ZnO nuclei formed larger clusters and nanoribbon on MoS_2 as compared to WS_2. AP-SCVD led to rapid ZnO nucleation on both CVD-grown MoS_2 and WS_2 in as little as 5 AP-SCVD oscillations and complete film closure was achieved on CVD-grown WS_2 flakes in less than 60 AP-SCVD oscillations. This was attributed to the higher precursor partial pressures and uniform precursor delivery afforded by the AP-SCVD process. Raman and

photoluminescence (PL) spectroscopy revealed that AP-SCVD is a benign process that doesn't damage the underlying 2D materials and rather helps to passivate defects via oxygen/water adsorption from the air, when performed in the appropriate temperature window. Deposition of the ZnO was found to impact the optical and structural properties of CVD-grown MoS_2 and WS_2 differently. For the MoS_2-ZnO heterostructure, electron doping and strain dominate, resulting in a reduction in the PL of MoS_2, whereas for the WS_2-ZnO, strain and dielectric screening have a larger impact, resulting in an enhanced PL.

Acknowledgements

I would like to express immense gratitude to my supervisor, Prof. Dr. Kevin Musselman, for giving me the opportunity to pursue MASc studies under his guidance. His passion for research and the intensity with which he works has always been a source of inspiration for me. He has generously given me his valuable time and made sure his office door is always open for discussions. His guidance, valuable insights, and approach to problem-solving were invaluable in forming my early research career. The most important lesson I've learned from him is dedication and patience, which I will carry with me throughout my life. I will be forever indebted to him for this opportunity.

I would also like to thank all my colleagues and friends for a very pleasant and friendly work environment. I would like to acknowledge their invaluable contribution, encouragement, and constant support. I can definitely say that they made my transition to Canada as an international student very smooth.

My sincere thanks to Farman for always being there to solve any SALD-related issues and for engaging in insightful research discussions; Ahmed for his help with all academic-related matters, providing guidance whenever I needed it; Jun and Tobiloba for their constant support during my exchange in Germany; and Jhi for connecting with me on LinkedIn and helping me make one of the best decisions of my life—pursuing master's under Prof. Kevin's supervision.

పప్పా నా హృదయ పూర్వక ధన్యవాదములు ఎందుకు అంటే నాకు ఉన్నత స్థాయి విద్యను ప్రోత్సహించి చదివించి నందుకు. అమ్మా నాకోసం ఎంతో ఆసరాగా నిలబడి, నా చదువు కోసం పూర్తి సహకారం అందించావు చాలా చాలా ధన్యవాదములు.

My heartfelt thank you to Akka for shaping the person I am today and for always having my back and Ivan bhaiyya for his unwavering support.

Dedication

To almighty God and my idol Dr. A.P.J Abdul Kalam sir whose life and teachings continue to inspire me every day.

Table of Contents

Author's Declaration ii

Statement of Contributions iii

Abstract iv

Acknowledgements vi

Dedication vii

List of Figures x

List of Tables xiii

List of Abbreviations xiv

Chapter 1 Introduction 1

1.1 Introduction to atmospheric-pressure spatial atomic layer deposition 1

1.2 Metal oxides and their applications 5

1.2.1 Introduction to silicon dioxide in the packaging industry 6

1.2.2 Introduction to 2D materials and their heterostructures with metal oxides 8

1.3 Thesis structure 10

Chapter 2 Experimental Methods 11

2.1 Atmospheric-pressure spatial atomic layer deposition 11

2.1.1 AP-SALD of silicon oxide 13

2.1.2 Atmospheric-pressure spatial chemical vapor deposition (AP-SCVD) of zinc oxide 14

2.2 Synthesis of 2D materials 15

2.2.1 Chemical vapor deposition of WS_2 and MoS_2 16

2.2.2 Exfoliation of WS_2 and MoS_2 18

2.3 Characterization 18

2.3.1 Atomic force microscopy 19

2.3.2 Ellipsometry 20
2.3.3 X-ray photoelectron spectroscopy 21
2.3.4 Scanning electron microscopy and energy dispersive x-ray spectroscopy (SEM/EDS) 22
2.3.5 Raman spectroscopy 22
2.3.6 Photoluminescence spectroscopy 23
Chapter 3 Atmospheric pressure spatial atomic layer deposition of silicon oxide using DIPAS and ozone 24
3.1 Introduction 24
3.2 Precursor selection 24
3.3 DIPAS synthesis 25
3.4 Film Characterization 27
3.5 Results and discussion 28
3.5.1 Peroxide-30 as an oxidant 28
3.5.2 Ozone as an oxidant 31
Chapter 4 Rapid nucleation of ZnO deposited using an atmospheric-pressure spatial atomic layer deposition system on 2D -MoS_2 and WS_2 38
4.1 Introduction 38
4.2 Results and discussion 38
4.2.1 ZnO nucleation on CVD-grown MoS_2 and WS_2 38
4.2.2 Structural and optical properties of CVD-grown monolayer MoS_2 and WS_2 46
Chapter 5 Conclusions and Future Work 56
5.1 Conclusions 56
5.2 Future work 57
References 58

List of Figures

Figure 1. (a) ALD reaction cycle (b) Growth per cycle as a function of temperature..... 2
Figure 2. (a) Conventional ALD, where the precursors are separated in time, as compared to (b) spatial ALD, where the precursors are separated in space. Reproduced with permission from J. Vac. Sci. Technol. A. 2011;30(1). doi:10.1116/1.3670745. Copyright 2011, American Vacuum Society.... 4
Figure 3. Gas manifold injector..... 5
Figure 4. (a) MoS_2 layer structure (Mo atom and S atom are represented by black and yellow, respectively), (b) top view (honeycomb lattice). Reproduced from Springer Nature, *Trans Indian Inst Met* 76, 195–204 (2023). http://creativecommons.org/licenses/by/4.0/.[36] (c) WS_2 layer structure (W atom and S atom are represented by blue and yellow, respectively), (d) top view. Reproduced from John Wiley and Sons, Advanced Electronic Materials, Vol 7 (2020).[34] 9
Figure 6. Schematic of sheet-to-sheet AP-SALD system..... 14
Figure 7. Schematic of AP-SCVD of ZnO on TMDCs using lab-scale AP-SALD system. 15
Figure 8. (a) CVD-reaction mechanism, where the precursors are introduced together on the substrate. (b) ALD reactions are split into two sequential half reactions. 16
Figure 9. AP-CVD tube furnace schematic 17
Figure 10. Schematic of atomic force microscopy 19
Figure 11. Emission of a photoelectron during XPS 21
Figure 12. Diisopropylamino silane (DIPAS) molecular structure. 25
Figure 13. (a) Reaction scheme for DIPAS synthesis. (b)1H NMR spectrum for DIPAS. 27
Figure 14. Nano crystallites deposited using DIPAS and peroxide-30 at room temperature. (a) AFM image on silicon substrate. (b) XPS survey, (c) Si 2p spectrum, and (d) O 1s spectrum on an ITO/glass substrate. 29
Figure 15. XRD data for depositions at room temperature using DIPAS and peroxide-30 and using DIPAS and ozone at 100°C. 30
Figure 16. Depositions using DIPAS and ozone. (a) Thickness and GPC as a function of ozone-generator voltage and deposition temperature. (b) Thickness and GPC as a function of DIPAS bubbling rate. 31
Figure 17. (a) Cloudy film texture as observed by eye at T= 28°C. b) Dark grey SiO_x film texture as observed by eye at T= 100°C. 32
Figure 18. Microstructures produced using DIPAS and ozone at different temperatures. 34

Figure 19. (a) XPS survey, (b) Si 2p spectrum, and (c) O 1s spectrum for a silicon oxide film deposited using DIPAS and ozone at 100°C on an ITO/glass substrate..... 35
Figure 20. (a) Backscattered SEM image of nano crystallites deposited on a Si substrate at room temperature using DIPAS and ozone. EDS spectra at (b) spot 1 – nano crystallite phase, (c) spot 2 - substrate, and (d) spot 3 - nano crystallite phase. 37
Figure 21. AFM images and line scans of CVD-grown (a-d) MoS_2 and (e-h) WS_2 with varying quantities of ZnO deposited via AP-SCVD. 39
Figure 22. ZnO nucleation for 35 AP-SCVD oscillations on (a) CVD-MoS_2 and (b) CVD-WS_2. These measurements were done under similar conditions, i.e., similar deposition and AFM parameters (scan size, frequency etc.). 40
Figure 23. ZnO deposition on exfoliated WS_2 with varying numbers of AP-SCVD oscillations. (a) Pristine, (b) 25 oscillations, (c) 35 oscillations, and (d) 60 oscillations. 41
Figure 24. ZnO deposition on exfoliated MoS_2 with varying numbers of AP-SCVD oscillations. (a) Pristine, (b) 25 oscillations, (c) 35 oscillations, and (d) 60 oscillations. 42
Figure 25. Preferential nucleation of ZnO on flake edges of (a) CVD-MoS_2 (5 AP-SCVD oscillations) and (b) CVD-WS_2 (25 AP-SCVD oscillations). 43
Figure 26. AFM images of ZnO deposited by 5 oscillations of AP-SCVD on (a) CVD-MoS_2 and (b) CVD-WS_2 at 100°C. A larger reactor-substrate spacing of 150 µm (compared to 110 µm in Figures 21 and 25) was used to further increase the deposition rate. 45
Figure 27. Raman spectra for (a) CVD-MoS_2 and (b) CVD-WS_2 before and after simulated AP-SCVD conditions. 46
Figure 28. (a) PL spectra of CVD-MoS_2 (pristine vs. AP-SCVD simulated conditions). Deconvoluted spectra of (b) pristine CVD-MoS_2 and (c) CVD-MoS_2 after simulated AP-SCVD conditions. (d) PL spectra of CVD-WS_2 (pristine vs. AP-SCVD simulated conditions). Deconvoluted spectra of (e) pristine CVD-WS_2 and (f) CVD-WS_2 after simulated AP-SCVD conditions. 47
Figure 29. (a) PL spectra of differently shaped flakes before and after simulated AP-SCVD processing. Non-triangular CVD-MoS_2 flakes (e.g., “Flake 2” in c)) show a comparatively larger increase in PL than triangular flakes (e.g., “Flake 1” in b)). 49
Figure 30. (a) Raman and (b) PL spectra of CVD-MoS_2 before and after ZnO deposition; (c) Raman and (d) PL spectra of CVD-WS_2 before and after ZnO deposition. 50

Figure 31. PL spectra for pristine CVD-WS_2, CVD-WS_2 annealed in air, and CVD-WS_2 after the deposition of ZnO using 300 AP-SCVD oscillations, at annealing and deposition temperatures of (a) 50°C, (b) 100°C, (c) 150°C, (d) 200°C and (e) 250°C 54
Figure 32. Change in PL intensity of CVD-WS2 after annealing or ZnO deposition at different temperatures. 55

List of Tables

Table 1. Nucleation of ZnO on MoS_2 and WS_2 44

Table 2. Intensity ratios of exciton (A^0) and trion (A^-) PL peaks for CVD-MoS_2 and CVD-WS_2 before and after simulated AP-SCVD treatment 48

List of Abbreviations

AFM	Atomic force microscopy
ALD	Atomic layer deposition
AP-CVD	Atmospheric pressure chemical vapor deposition
AP-SALD	Atmospheric pressure spatial atomic layer deposition
AP-SCVD	Atmospheric-pressure spatial chemical vapor deposition
CVD	Chemical vapor deposition
DEZ	Diethyl zinc
DIPAS	Di-isopropyl amino silane
EDS	Energy dispersive spectroscopy
GPC	Growth per cycle
PE-ALD	Plasma-enhanced atomic layer deposition
PL	Photoluminescence
SEM	Scanning electron microscopy
TMDC	Transition metal dichalcogenide
XPS	X-ray photoelectron spectroscopy
XRD	X-ray diffraction

Chapter 1
Introduction

1.1 Introduction to atmospheric-pressure spatial atomic layer deposition

As technology advances towards increased miniaturization, functional nanomaterials are becoming an integral part of our daily lives. The rise of the "Internet of Things" has accelerated this trend, necessitating smaller and more integrated devices. While advances in vacuum-based deposition and printing technology have aided in this downsizing, widespread use of nanomaterials demands more cost-effective alternatives.

One important class of nanomaterials that is already finding use in a variety of industries is thin films. Their versatility is evident in everything including food packaging, where they are used as protective coatings[1,2] and the fashion industry where they contribute to novel, high-performance textiles[3,4]. Thin films also play an important role in the electronics industry where they are used in energy storage technologies[5–7] as well as improved display technologies[8,9]. Their diverse applications make them indispensable in both ordinary everyday products and cutting-edge developments.

There are several established techniques to synthesize thin films, one of them being conventional atomic layer deposition or *temporal* atomic layer deposition (ALD). ALD is a well-established technique first developed in 1974 by Tuomo Suntola[10]. This technique is a subset of chemical vapor deposition (CVD) and has become a commercially critical thin-film deposition techniques due to its ability to deposit high-quality thin films with precise atomic-scale thickness control, uniformity and layer conformality[11].

In addition to this, ALD can normally be conducted at lower temperatures than CVD due to its unique self-limiting reaction mechanism (discussed below). Over time, ALD precursors have been designed with greater surface reactivity while avoiding any thermally triggered CVD-like reactions on the substrate so that the process follows a sequential deposition cycle, layer by layer.[12]

The ALD process is typically performed under vacuum. The two reacting precursors are stored separately, and the precursor delivery mechanism varies depending on the type of the system. A conventional ALD cycle (Figure 1) begins with introduction of precursor “A” into the vacuum chamber, where it would ideally saturate the substrate surface by adsorbing on all the active sites on the substrate.

Once the surface is exposed to precursor "A" to fully cover the surface, the entire chamber is purged with an inert gas such as argon (Ar) or nitrogen (N_2). This purging step helps remove any excess precursor that didn't react with the substrate. Following the purge step, precursor "B" is introduced in the chamber. Precursor "B" reacts with the adsorbed layer of precursor "A" to ideally form one atomic-layer-thick monolayer of the desired material. This is followed by a second purge step, which ensures the removal of excess of precursor "B" along with by-products produced during the chemical reaction. The purge steps are very essential to avoid any CVD growth in the chamber and to ensure that the adsorber layer of precursor "A" exclusively reacts with the precursor "B" to form a monolayer, namely "AB". The cyclic process is continued until the desired thickness is achieved, with each cycle depositing one monolayer. This technique is known for its precise thickness growth at the atomic level because each monolayer growth is precisely controlled by the number of cycles involved in the deposition process.

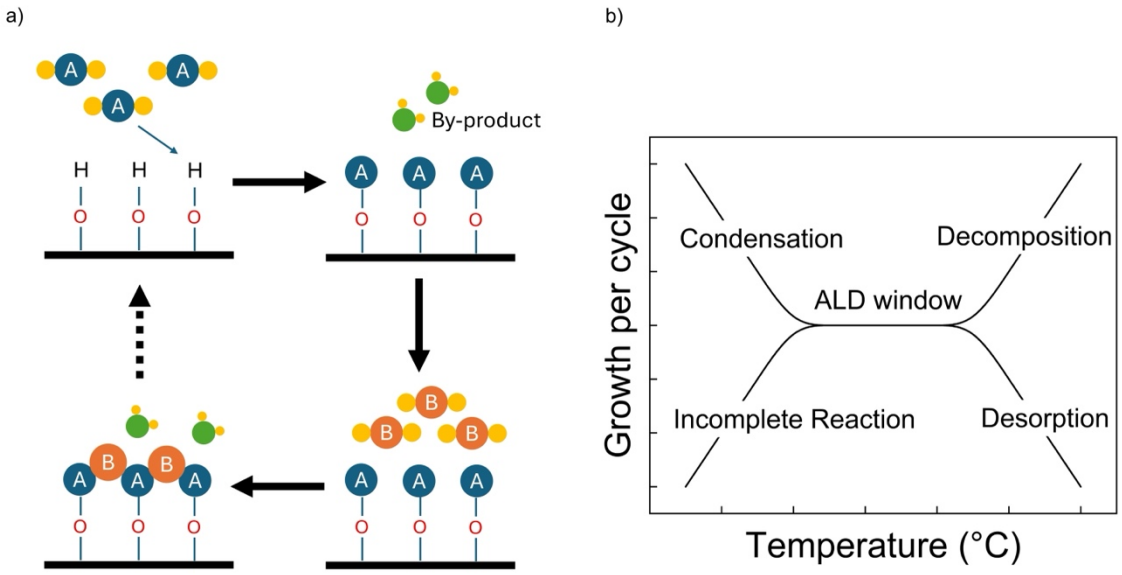


Figure 1. (a) ALD reaction cycle (b) Growth per cycle as a function of temperature

The development of the ALD process necessitates careful consideration of precursor selection, composition, reaction temperature, and numerous other factors. Before starting the experiment, precursor selection must be performed to determine the best precursor and co-reactant combination. After the thin film is grown, the film's composition must be evaluated and checked to ensure that the

deposited material is of the desired composition. This analysis can be performed using a variety of techniques, including XPS, EDS, etc. Varying the reaction temperature has a major impact on material properties and growth behavior. It is always recommended to ensure that the response occurs within the ALD regime or window. In this temperature frame, the growth per cycle is constant, and the self-limiting reactions dominate (Figure 1b.). Outside the ALD window, precursor condensation can occur at lower temperatures, where precursor molecules physically adsorb onto the substrate due to insufficient thermal energy for chemical reactions. This is undesirable as it compromises the precision and uniformity of ALD processes. Conversely, at higher temperatures, precursor decomposition may take place, breaking down the precursor molecules without triggering the intended chemical reactions. This can negatively impact the film's composition, leading to undesired by-products, contamination, or non-uniform growth.

Given the ALD process discussed above and its associated advantages, it is important to understand that its application is largely limited to high-value-added products due to the high costs associated with the process. Most of the time, conventional ALD is performed under low-pressure conditions, requiring expensive and advanced vacuum technology to maintain the controlled environment for the deposition. Therefore, scaling up vacuum equipment to accommodate larger substrates or higher throughput rates can be complex and expensive.

Another limitation of conventional ALD is its slow deposition rate. Since the process involves introducing each precursor followed by purge steps in between, each deposition cycle is time consuming. The separation of precursors in time slows down the process making it less suitable for mass production in cost-sensitive, high-throughput applications.

Spatial atomic layer deposition has emerged as a promising, modified ALD technique that can help overcome the above-mentioned challenge of slow deposition speed. In conventional ALD, the in-between purging steps are the most time-consuming, taking up 50% of the entire cycle time.[12] Also, as previously stated in ALD, precursors are separated in time, requiring enough time to ensure they react completely with each other, further slowing down the overall process. Spatial ALD provides a more efficient alternative in which the precursors are spatially separated, allowing for continuous flow of the precursors over the substrate in different regions (Figure 2). This allows each step to proceed simultaneously, eliminating the slow purge cycles and shortening the deposition time.

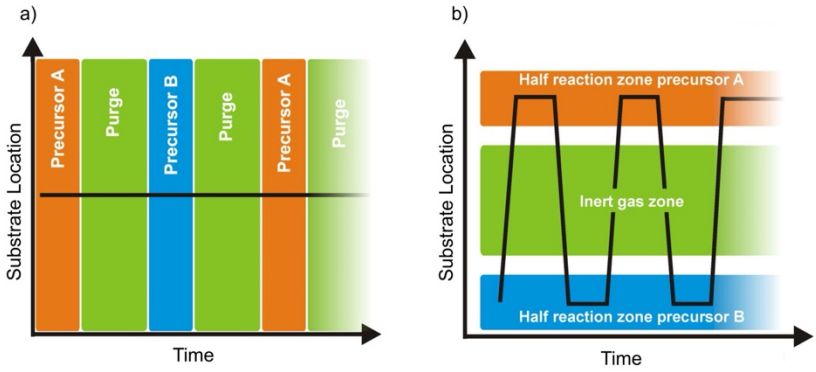


Figure 2. (a) Conventional ALD, where the precursors are separated in time, as compared to (b) spatial ALD, where the precursors are separated in space. Reproduced with permission from J. Vac. Sci. Technol. A. 2011;30(1). doi:10.1116/1.3670745. Copyright 2011, American Vacuum Society.

More recently, atmospheric-pressure spatial atomic layer deposition (AP-SALD), an open-air modification of spatial ALD, has been introduced and can help reduce the need for expensive vacuum equipment, as it is operated in open-air conditions. This makes it a more appealing method from the perspective of scalability and cost effectiveness.

In AP-SALD, a reactor head (a gas manifold injector) is used (Figure 3). It is placed in close proximity with the substrate to avoid intermixing of the precursor gases. Depending on the type of system, either the reactor head or the substrate oscillates, while the other remains stationary. The precursor gases flow parallel to each other and are separated by streams of inert gas, typically acting as a curtain to isolate the reactive precursors. This setup allows the precursors to coat the substrate in a similar manner as conventional ALD, but without the slow purge steps, enabling the faster deposition of thin films. The details of the process are introduced later in Chapter 2.

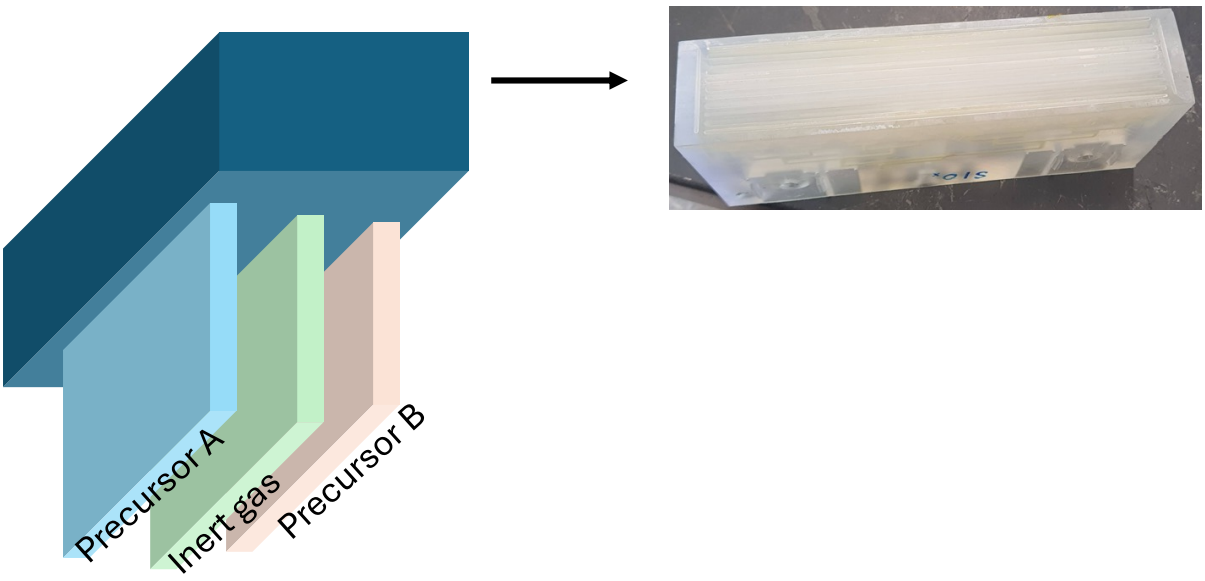


Figure 3. Gas manifold injector

The possible advantages of AP-SALD over conventional ALD can be summarized as follows[12,13]:

- Vacuum-free process - AP-SALD operates at atmospheric pressure, making the process easy to use, simpler to set-up and less expensive.
- Faster deposition rate - Continuous parallel flows of precursors eliminate the long pulse and purge steps, dramatically improving the deposition rate.
- Cost effective - Due to an accelerated, vacuum-free process.
- Scalable - By eliminating the vacuum chamber, it can help accommodate any substrate size and can be adopted for high-throughput processes such as sheet-to-sheet or roll-to-roll manufacturing.
- Flexible - Dopants or any other precursor can be easily introducing by alternating or modifying the injector manifold, providing the opportunity to create laminates and mixed oxide thin films.

1.2 Metal oxides and their applications

As previously stated, thin films are an important class of nanomaterials, with metal-oxide thin films making up a significant portion of this class. Usually, chemical synthesis of metal-oxide thin films is

based on a metal precursor chemically reacting with an oxidant. Metal-oxide-based thin films are widely popular due to their versatile properties, finding application in microelectronics, energy storage, optics, sensors, barrier coating and catalysis.[14,15] The ability to fine tune their properties, such as electrical conductivity, optical properties, barrier properties and chemical reactivity make them integral for these advanced applications.

1.2.1 Introduction to silicon dioxide in the packaging industry

Packaging materials are essential to protect food items, preserve nutrition, and facilitate proper handling, storage, and transport of commercial goods. Most plastics used in food packaging are non-compostable, including polyethylene (PE), high-density polyethylene (HDPE), and low-density polyethylene (LDPE). These materials are strong, thermally stable, and provide food with high-quality protection. However, the increased reliability of non-biodegradable polymers poses significant environmental risks.

Currently, the packaging industry generates 47 percent of plastic waste and remains the dominant sector in terms of plastic production.[16] The use of environmentally friendly and sustainable materials is essential for replacing non-degradable plastics and fulfilling various United Nations Sustainable Development Goals of “Life below water”, “Climate Action” and many more.[17]

A potential solution would be to use compostable and/or fully recyclable materials. However, current compostable and recyclable sustainable packaging materials don’t have adequate gas barrier properties to keep food fresh. Companies worldwide are urgently working to solve this problem due to increasing regulations limiting single-use plastics.[18] Incorporating nanomaterials into biodegradable polymers is one way to achieve the required barrier properties for sustainable packaging.

Over the last few decades, there has been a growing interest in silicon oxide (SiO_x) thin films for barrier films for food packaging. The use of thin SiO_x barrier films on a sustainable substrate is an exciting research field because matching thin inorganic barrier films to substrates creates an impermeable packaging material while remaining flexible, lightweight, and environmentally friendly.

As reported by Zhao et al., SiO_x films are particularly of interest because SiO_x when deposited on top of a biodegradable polymer such as polylactic acid (PLA) increases the water contact angle, which helps make the substrate more hydrophobic and improve the barrier properties.[19] Additionally, this

coating covers the holes and cracks naturally present in the PLA matrix and eventually forms a compact layer, thus enhancing the barrier properties of the PLA.[19]

1.2.1.1 Problem statement and research objectives

Various techniques have been developed to deposit SiO_x films, such as thermal chemical vapor deposition (CVD),[20] plasma-enhanced CVD,[21] and plasma-enhanced atomic layer deposition (PE-ALD)[22] to name a few. However, these processes involve elevated temperatures or the use of plasma, limiting their applicability to certain substrates and applications. Therefore, the ability to deposit high-quality SiO_x thin films using a scalable method at a relatively low temperature is highly desired.

One such scalable method is AP-SALD. As discussed above, AP-SALD separates the precursors spatially, thereby accelerating the deposition process. Also, operating in an open atmosphere facilitates scaling of the substrate size (e.g., roll-to-roll)[23] and allows for a high saturation dose, which further speeds up the process.[24]

Some AP-SALD studies have been carried out to deposit SiO_x using organic precursors. Mione et. al reported the use of plasma-enhanced AP-SALD to deposit SiO_x within the temperature range of 100-250°C. They reported a growth per cycle (GPC) ranging from 1 to 1.2 Å/cycle using bisdiethylaminosilane (BDEAS, $SiH_2[NEt_2]_2$) as the Si precursor and oxygen plasma as the oxidant.[25] In another study, Nguyen et al. successfully deposited SiO_x using trivinylmethoxysilane (TVMS) by modifying the reactor head to incorporate oxygen plasma. They increased the spacing between the reactor head and the substrate, allowing for precursor crosstalk and thus operated in CVD mode.[26] They reported that the use of the modified reactor head and oxygen plasma led to the formation of SiO_2 films at low temperatures ranging from room temperature to 80°C.[26]

While these studies emphasize the significance of AP-SALD, all the reported techniques use plasma as an oxidant source. This damage-inducing process may limit the application of AP-SALD to sensitive substrates such as polymers. Moreover, a plasma-based oxidation process is expensive and might not be appropriate for high-throughput applications such as food packaging. Therefore, the ability to deposit high-quality SiO_x thin films using a scalable method at a relatively low temperature is highly desired.

To the best of our knowledge, a plasma-free AP-SALD processes for SiO_x has not been reported. In this thesis, a custom-built AP-SALD system is used to test the plasma-free deposition of SiO_x films

using di-isopropylaminosilane (DIPAS) and either ozone or 30% hydrogen peroxide aqueous solution (peroxide-30) as the oxidant. A systematic study of this plasma-free process is conducted to understand the effect of various parameters such as temperature, metal-precursor flow rates, and oxidant flow rates on the composition and morphology of the deposited materials.

1.2.2 Introduction to 2D materials and their heterostructures with metal oxides

Another emerging class of nanomaterials are the 2-dimensional or 2D materials. Since the pivotal discovery of graphene, the family of 2D materials has grown[27] with transition metal dichalcogenides (TMDCs) as an emerging class. These semiconducting materials have a chemical formula of MX_2 where M is a transition metal atom such as tungsten (W) or molybdenum (Mo) and X is a chalcogen atom such as sulfur (S), selenium (Se) or tellurium (Te).[28] This class of materials exhibits unique electrical and optical properties due to quantum confinement effects and surface effects and thus is promising for ultra-small and low-power electronics, such as transistors and LEDs.[29] As miniaturization continues, devices based on 2D materials are expected to be more efficient than current Si-based devices.[30]

In this thesis, I focus majorly on two important TMDCs – MoS_2 and WS_2. Both MoS_2 and WS_2 have similar hexagonal crystalline structure. Each monolayer consists of sulphur atoms with the metal atom (molybdenum or tungsten) sandwiched between them, forming an S-M-S structure [31]. Monolayer MoS_2 has a thickness of 0.65 nm[32] (Figure 4a) and a sulfur-to-sulfur distance of 3.16 Å (Figure 4b). [33] WS_2 (Figure 4c and d) has a slightly different thickness of ~ 0.65 nm[34] and a sulfur-to-sulfur distance of 3.153 Å. [35] The atoms within each layer are covalently bonded, however, the layers themselves are bonded by weak van der Waals forces and hence can be isolated easily.

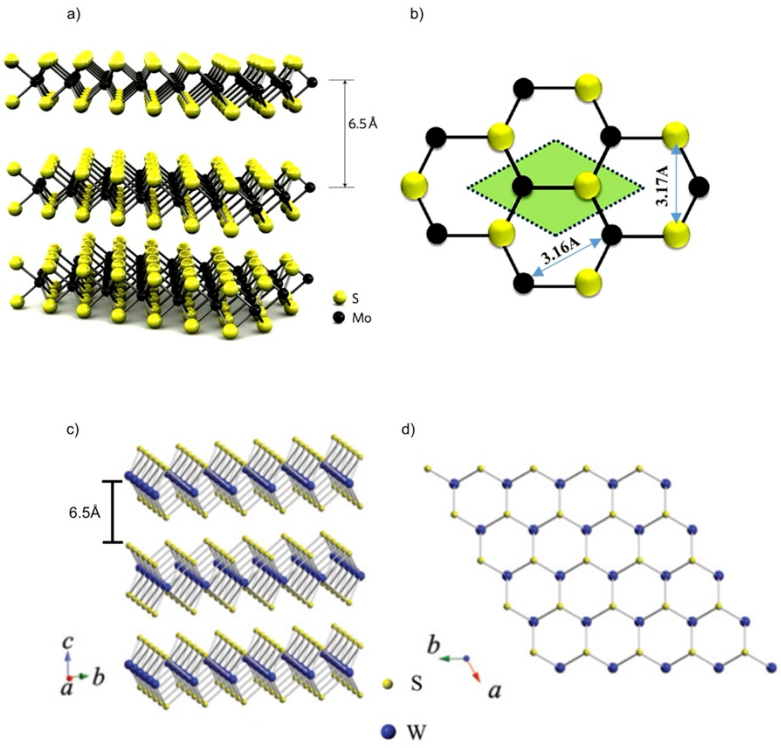


Figure 4. (a) MoS_2 layer structure (Mo atom and S atom are represented by black and yellow, respectively), (b) top view (honeycomb lattice). Reproduced from Springer Nature, *Trans Indian Inst Met* 76, 195–204 (2023). http://creativecommons.org/licenses/by/4.0/.[36] (c) WS_2 layer structure (W atom and S atom are represented by blue and yellow, respectively), (d) top view. Reproduced from John Wiley and Sons, Advanced Electronic Materials, Vol 7 (2020).[34]

Bulk MoS_2 and WS_2 have indirect band gaps; however, when isolated into monolayers, they transition to direct-band-gap materials. Monolayer MoS_2 has a band gap of 1.78 eV to 1.87 eV,[37–39] and WS_2 has a value between 1.9 eV to 2.0 eV[40,32] making them a very attractive choice for electronic devices.

1.2.2.1 Problem statement and research objectives

To use 2D materials, such as TMDCs, in devices, it is important to understand their integration with other functional materials (e.g., oxides) and what impact this has on the properties of the 2D layer. Different systems have been studied to date, including Al_2O_3 or HfO_2 as a high k-dielectric layer on graphene for transistors,[42,43] ZnO on WS_2 for LEDs[44] and ZnO on WSe_2 for photodetectors,[45] among

others. These metal oxides were grown via atomic layer deposition (ALD) due to its ability to grow pinhole-free, conformal thin films with precise thickness control.

However, depositing functional metal oxides, such as Al_2O_3 or ZnO, on 2D materials has proven challenging as the passivated 2D surface lacks dangling bonds which act as nucleation sites for ALD precursors. Previous ALD studies have reported that layer closure for Al_2O_3 on exfoliated monolayer WS_2 surfaces was achieved at a very high thickness, i.e., more than 200 ALD cycles were required to achieve linear growth after nucleation. Different approaches have been attempted to facilitate faster nucleation on the inert surfaces of 2D materials, such as growing a seed layer,[46] using a physical vapor deposition technique that doesn't rely on the presence of surface dangling bonds, and/or pre-treating the 2D material using UV-Ozone or electron beam irradiation;[47] however, these routes can unintentionally dope the 2D material and degrade its properties.

To address these challenges, I investigate the nucleation and growth of ZnO on 2D WS_2 and MoS_2 using an AP-SALD system operated in atmospheric-pressure spatial chemical vapor deposition (AP-SCVD) mode.

1.3 Thesis structure

The primary objective of this thesis is to develop AP-SALD processes for different applications. The thesis is structured in the following way: **Chapter 2** presents a brief introduction to various **experimental and analytical methods** used in the study. **Chapter 3** focuses on developing the **AP-SALD process for silicon oxide deposition** and the discussion of the results. **Chapter 4** focusses on the **nucleation and growth of ZnO on different (2D) materials** and the effect of the ZnO AP-SCVD process on the 2D materials. The **final chapter** presents the **conclusions** of the thesis and suggestions for **future work**.

Chapter 2
Experimental Methods

2.1 Atmospheric-pressure spatial atomic layer deposition

As described previously, AP-SALD is an open-air technique in which the precursors are spatially separated. Most of the time, the wide range of precursors available for ALD can be used for spatial ALD as well. However, it must be remembered that since AP-SALD process is conducted in ambient, precursors that may release harmful by-products should be avoided.

In this work, two custom-built AP-SALD systems were used. For the first study on the deposition of silicon oxide, a sheet-to-sheet system was used that is capable of coating relatively large substrate sizes (~600 cm^2). For the second study of zinc oxide nucleation on 2D materials, a lab-scale AP-SALD system was used since the substrate sizes were comparatively small. The lab-scale system can coat substrate sizes of ~30 cm^2. However, the mechanism for both the systems stays similar.

Starting with the precursor delivery system, the precursors are stored in bubblers. The bubbler has two openings, an inlet and an outlet. Inert gas (nitrogen gas) flows through the inlet and is used to bubble through the precursor. This saturates the gas with vapor of the precursor. The nitrogen gas carries the precursor molecules to the outlet and hence usually precursors with high vapor pressure are used. The precursor bubbler is usually wrapped in a heat jacket to provide enough thermal energy, if required, to generate the required vapor pressure. As the precursor flows out of the bubbler, it is further diluted with an inert carrier gas (nitrogen gas), before being delivered to the reactor head. The precursor delivery is controlled by mass flow controllers (MFCs) that regulate the flow of nitrogen gas.

The precursor gases flow through the reactor head, which has multiple slits, as shown in Figure 5. Each slit is dedicated to a certain gas. The precursor gases (Metal 1, Metal 2, and Oxidizer in Figure 5 are separated in space by inert gas curtains (nitrogen). These inert gas curtains can ensure that the precursor gases do not interact with each other directly but only react on the surface of the substrate. There are some extra slits in the reactor head, which are dedicated exhaust channels (Ex) to remove any excess precursor or by-products formed during the reaction. For the AP-SALD systems used in this

work, the reactor head is stationary, and the substrate is oscillated underneath the reactor on a heated substrate stage.

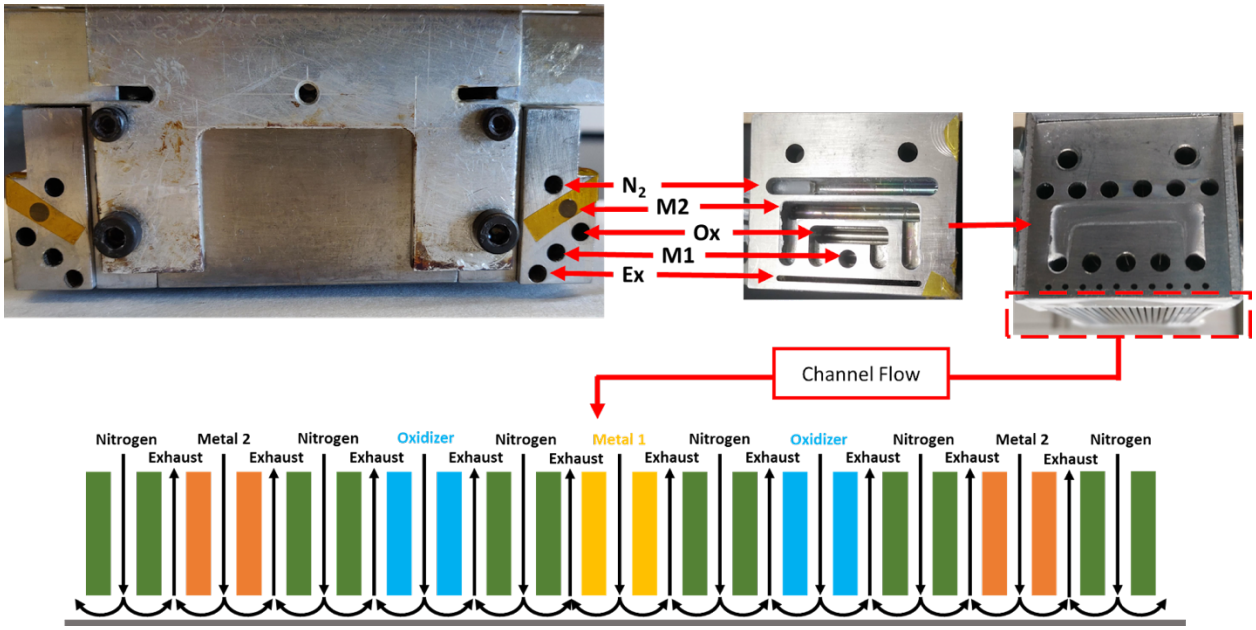


Figure 5. Reactor head channel flow for lab-scale AP-SALD system

Each precursor has a dedicated zone, and the oscillating substrate moves through each of these zones to replicate the pulsing sequence in conventional ALD (Figure 5). For example, diethyl zinc and water will react together to deposit ZnO. The substrate oscillation is continued until the desired thickness is achieved.

The deposition process steps for AP-SALD are as follows. Before starting each deposition, it is made sure that the tubes connecting different parts such as MFCs to the bubbler, the bubbler to the reactor heads etc. are purged with nitrogen gas to ensure no oxygen is left. The purge cycle generally takes around 10 minutes and helps make sure the whole system is clean and residue free. Once the purging is completed, the other parameters such as the flow rate, stage temperature and the distance between the reactor head and substrate are set. The latter is important as the spacing governs if the system operates in ALD mode. At an optimum spacing, the precursor gases experience the least amount of turbulence and are well isolated from each other by the inert gas curtains. A spacing that is too high or too low can cause turbulence and lead to interaction of the precursors in the gas phase, leading to CVD-type growth. A low vacuum is used to hold the substrate in place on the heated stage. The bubblers are

finally opened, and the system is ready for the first deposition. At the end of all the depositions, the system is again purged with nitrogen gas to remove any residues behind.

2.1.1 AP-SALD of silicon oxide

The custom-built sheet-to-sheet AP-SALD system (Figure 6) was used for SiO_x depositions. In this system, a reactor head with dimensions of 145 mm × 31 mm × 64 mm was kept fixed and the substrate was oscillated beneath it on a stage that was heated from room temperature up to 100°C. DIPAS was used as the Si precursor and was bubbled using high-purity nitrogen at flow rates ranging from 80 to 550 sccm. The bubbled DIPAS was combined with a nitrogen carrier line for a total flow of 800 sccm from one outlet channel on the underside of the reactor, unless specified otherwise. Hydrogen peroxide or ozone was used as the oxidant and delivered to two outlet channels. The hydrogen peroxide (30% w/w in water, peroxide-30) was bubbled with 100 sccm of nitrogen and combined with a 300 sccm carrier flow. For experiments conducted with ozone, an ATLAS -30 UHC ozone generator was utilized to produce ozone from 92.5% oxygen gas (balance nitrogen). The generator is expected to produce ozone at a rate of 22.48 g/h when operating at maximum voltage (100V) and 20 psig gas pressure. The ozone generator's potentiometer was adjusted between 10 to 80 V to control the ozone generation percentage, and the oxygen/ozone flowmeter was set to 300 sccm. To prevent ozone exposure, the reaction chamber was completely sealed. The DIPAS bubbling rate was consistently kept elevated compared to the ozone generation rate. This approach guaranteed that all produced ozone reacted with surplus DIPAS, limiting the presence of unreacted ozone. As shown in Figure 6, inert nitrogen curtains and exhaust channels were used to separate the DIPAS and oxidants. The nitrogen curtain gas-flow rate was kept constant at 3000 sccm, which was divided between 2 outlet channels. All gas outlet channels were 1 mm wide and 130 mm long. 1.5mm-wide exhaust channels were used to help remove excess precursor. The substrate oscillation speed was set to 30 mm/sec and the path length depended on the size of the substrate, which was roughly 60 mm in length, implying it required 4 seconds to complete one AP-SALD oscillation, which is equivalent to two temporal ALD cycles.

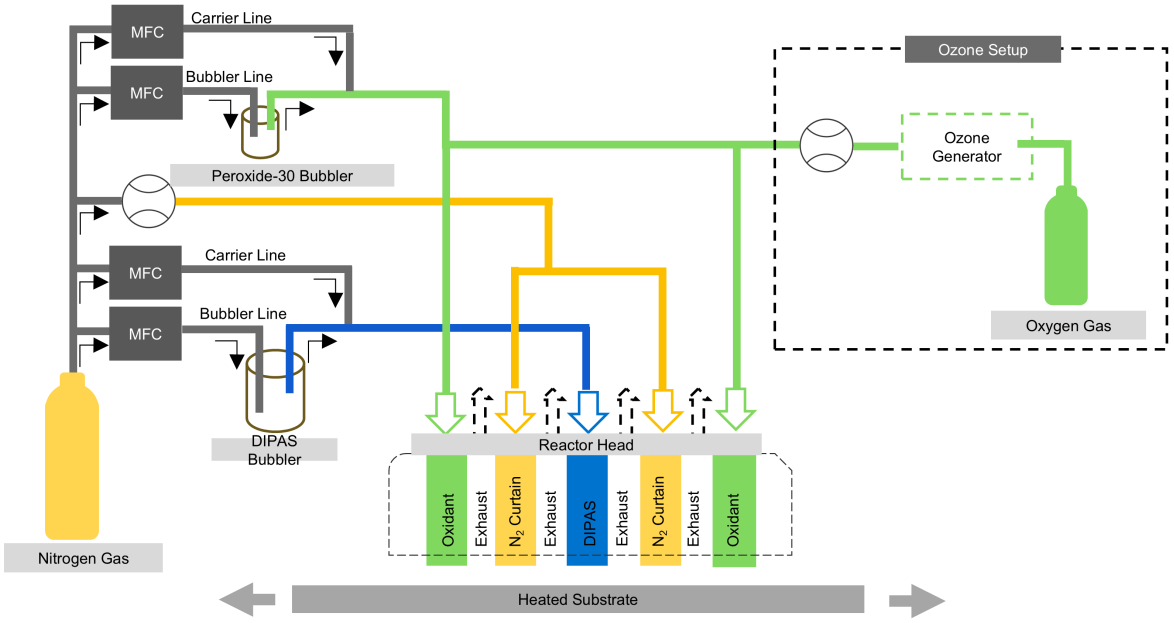


Figure 5. Schematic of sheet-to-sheet AP-SALD system

2.1.2 Atmospheric-pressure spatial chemical vapor deposition (AP-SCVD) of zinc oxide

From our previous discussion we know that the deposition rate for AP-SALD is higher than for conventional ALD, as the slow chamber-evacuation and purge steps are eliminated. It can be further increased by operating the same system in AP-SCVD mode.[48,49] This can be done by varying process parameters, such as the spacing between the reactor head and substrate, the substrate oscillation speed, or the precursor flow rates to facilitate some mixing of the precursors in the gas phase. The presence of both precursors on the substrate facilitates CVD-type film deposition without compromising on the quality of the film; AP-SCVD is known to produce conformal and pinhole-free films similar to those achieved with ALD.[48]

In this study a custom-built AP-SALD/SCVD system was used to deposit ZnO on top of WS_2 and MoS_2 (Figure 7). In this system the substrate moves underneath the stationary reactor head. Diethyl zinc (DEZ, 96%, Thermo Scientific Chemicals) and distilled water were used as a zinc precursor and oxidant, respectively. The reactant gases were mixed with high-purity nitrogen (5.0 rated) as a carrier gas and were introduced simultaneously to the underside of the reactor head, but spatially separated by inert N_2 gas curtains and exhaust channels, which help remove excess precursors and reaction products.

DEZ was bubbled with high-purity N_2 at 40 sccm and was diluted by 200 sccm of N_2 carrier gas for a total flow of 240 sccm. Similarly, the water was bubbled at 45 sccm and combined with a N_2 carrier flow of 200 sccm, resulting in a total flow of 245 sccm at the outlet channels. As shown in Figure 7, 1200 sccm of high-purity N_2 was delivered to five inert N_2 curtains to minimize mixing of the DEZ and water. The spacing between the reactor head and substrate was maintained at ~110µm, unless specified otherwise, a spacing that results in some intermixing of the precursors in the gas phase leading to CVD-like deposition. The substrate stage was heated to 100°C and the DEZ and water bubblers were kept at room temperature. ZnO was deposited on top of both MoS_2 and WS_2 by oscillating the substrate stage 25, 35 and 60 times. The term oscillation used here represents the back-and-forth movement of the substrate. Therefore 1 oscillation is equivalent to 2 cycles in a conventional ALD system.

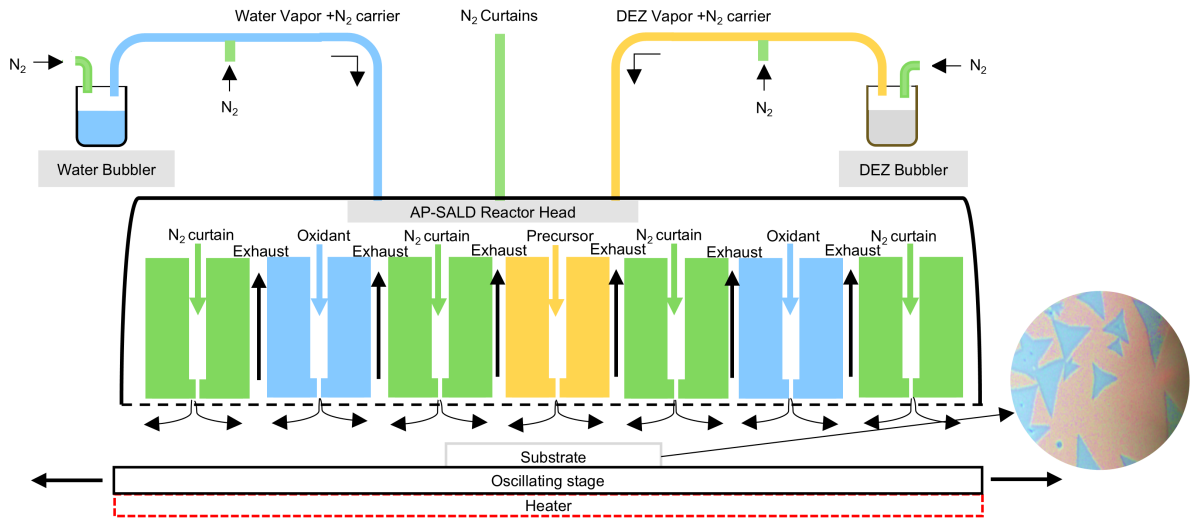


Figure 6. Schematic of AP-SCVD of ZnO on TMDCs using lab-scale AP-SALD system.

2.2 Synthesis of 2D materials

For the study of ZnO nucleation on 2D materials, WS_2 and MoS_2 were synthesized by CVD and by mechanical exfoliation.

2.2.1 Chemical vapor deposition of WS_2 and MoS_2

Chemical vapor deposition is one of the most established techniques to grow large area 2D materials on a supporting substrate. Unlike ALD, in CVD the precursors are introduced in the chamber together, as shown in Figure 8.

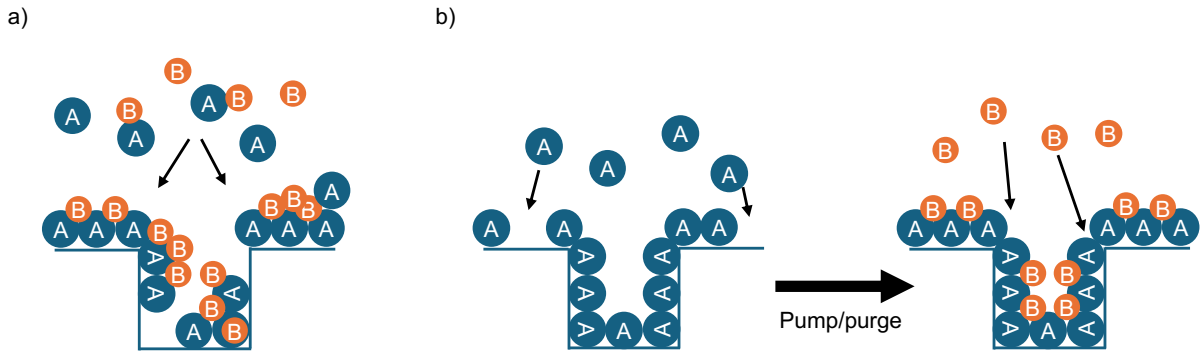


Figure 7. (a) CVD-reaction mechanism, where the precursors are introduced together on the substrate. (b) ALD reactions are split into two sequential half reactions.

In a typical CVD process, the precursor material is usually transferred in the gas phase, which is achieved via thermal heating. An inert gas is used as the carrier gas, which helps carry the reactants in the gas phase and the mass transport of the reactants (in the gas phase) is achieved by diffusion on the substrate. The reactants then react to form the desired film.

In this study, both WS_2 and MoS_2 flakes were grown via atmospheric-pressure chemical vapor deposition (AP-CVD) in a tube furnace (Figure 9) at University of Duisburg-Essen. The substrates used were highly doped p-type Si substrates with a 285-nm layer of thermally grown SiO_2. The substrates were cut to a size of approximately 15 mm x 15 mm and ultrasonicated for 10 minutes in acetone. After ultrasonication, a 2% cholic acid sodium solution was spin-coated onto the substrates, for both MoS_2 and WS_2, acting as a seeding promoter.

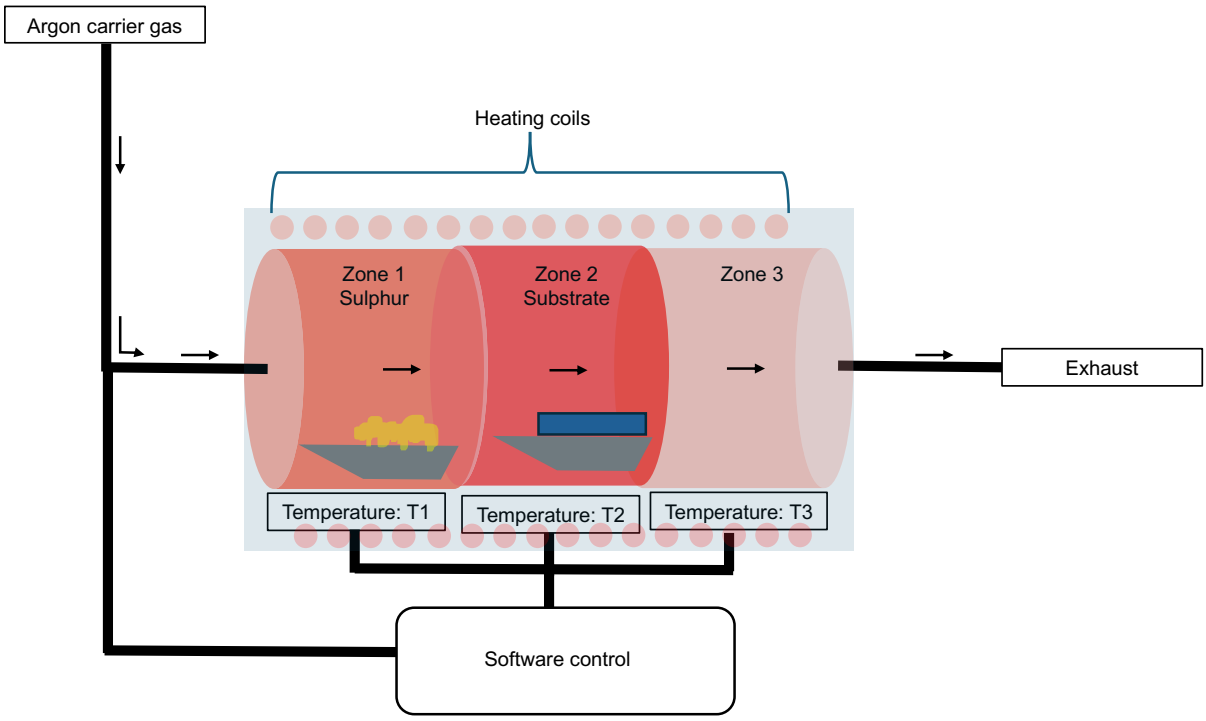


Figure 8. AP-CVD tube furnace schematic

For MoS_2, a drop of aqueous ammonium heptamolybdate (AHM) solution (1:1) was then placed on the substrates. A single drop of roughly 2 mm diameter at the edge was sufficient. The substrates were then annealed at 300 °C for 24 minutes in an oxygen-rich environment to convert AHM into MoO_3, which serves as the precursor for MoS_2.

Similarly, for WS_2, a fully saturated aqueous solution of ammonium metatungstate was used. A microliter pipette was used to drop several droplets (approximately 1 mm diameter) of the solution on the substrate, as the flakes tend to grow in the vicinity of the precursor. The samples were then annealed in air at 500 °C for 30 minutes to obtain WO_3.

The growth process was conducted in a three-zone hot-wall tube furnace (ThermConcept ROK 70/750/12-3z). In the first zone, 100 mg of S powder (99.98% purity, Sigma Aldrich) was placed in an alumina crucible at 150 °C. The coated substrates were placed in alumina combustion boats in the second zone, where a temperature of 750 °C was used for the growth of MoS_2 and 800 °C for WS_2. The tube was purged with 500 sccm of Ar gas (99.9% purity) to remove O_2 and H_2O before the CVD process commenced and was maintained at that flow during deposition. The growth process lasted 30 minutes,

after which the furnace was rapidly cooled to 100 °C. Finally, the samples were retrieved from the CVD furnace.

2.2.2 Exfoliation of WS_2 and MoS_2

Mechanical exfoliation of 2D materials is a technique in which the layered materials, bonded by weak van der Waals forces in the vertical direction, can be easily "peeled off" using adhesives such as a scotch tape. This technique is known to produce almost defect-free 2D materials, retaining their original properties, however, it is not scalable. Here, WS_2 and MoS_2 were exfoliated as reference materials to examine the ZnO nucleation in comparison to that on CVD-grown WS_2 and MoS_2.

Bulk MoS_2 crystal (supplied by SPI supplies) was exfoliated using adhesive tape. This led to the exfoliation of multilayers. Another piece of tape was then used to exfoliate a few layers from the multilayer MoS_2, and the process was repeated a few times. The tape carrying the MoS_2 flakes was then gently placed onto a Si substrate (76.2mm Si, N-type, P doped <100>, 1-10ohms-cm, SSP prime). Later, these samples were dipped in acetone, to remove the tape and adhesive residue, leaving few-layer MoS_2 flakes. The substrate was dried and examined under an optical microscope, using color contrast to identify and locate monolayer and few-layer MoS_2 flakes.

Similarly, bulk WS_2 crystals (supplied by HQ Graphene) were mechanically exfoliated using adhesive tape at University of Duisburg-Essen. Silicon with a 100-nm-thick SiO_2 layer was used as a substrate. The SiO_2/Si wafers were cut and then cleaned using nitrogen gas, followed by heating on a hot plate at 80°C for 10 minutes. A bulk WS_2 crystal was pressed onto the tape, which was then peeled away, removing layers of WS_2. To further reduce the thickness of these layers, the tape was repeatedly folded and unfolded, gradually thinning the WS_2 until monolayer or few-layer flakes were obtained. The tape carrying the WS_2 flakes was then gently placed onto the heated substrate and left for approximately 5 minutes to transfer the flakes to the substrate. The tape was then carefully peeled off, leaving WS_2 flakes deposited on the substrate surface. The substrate was then examined under an optical microscope, using color contrast to identify and locate monolayer and few-layer WS_2 flakes.

2.3 Characterization

Different characterization techniques were used for measurements and analysis in this thesis. The operating principle of each method is explained followed by the experimental details.

2.3.1 Atomic force microscopy

Atomic force microscopy (AFM) is widely used for studying the topography and roughness of thin films at the nanoscale. The working principle of an AFM is that a sharp tip is used to probe the sample surface (Figure 10). As the tip approaches the surface, the close-range forces become dominant which influence the attraction/deflection of the tip. To measure the deflection of the tip, a laser and a photodetector setup is used. The laser beam is shined upon the cantilever that holds the sharp tip. The surface of the cantilever is polished, to reflect the laser onto a four-quadrant photodetector. Any deflection in the tip caused due to unevenness of the surface or the force experienced between the tip and the sample is recorded by the position sensitive photodetector.[50] The tip is scanned over the surface of the sample and topographical information of the sample surface is recorded.

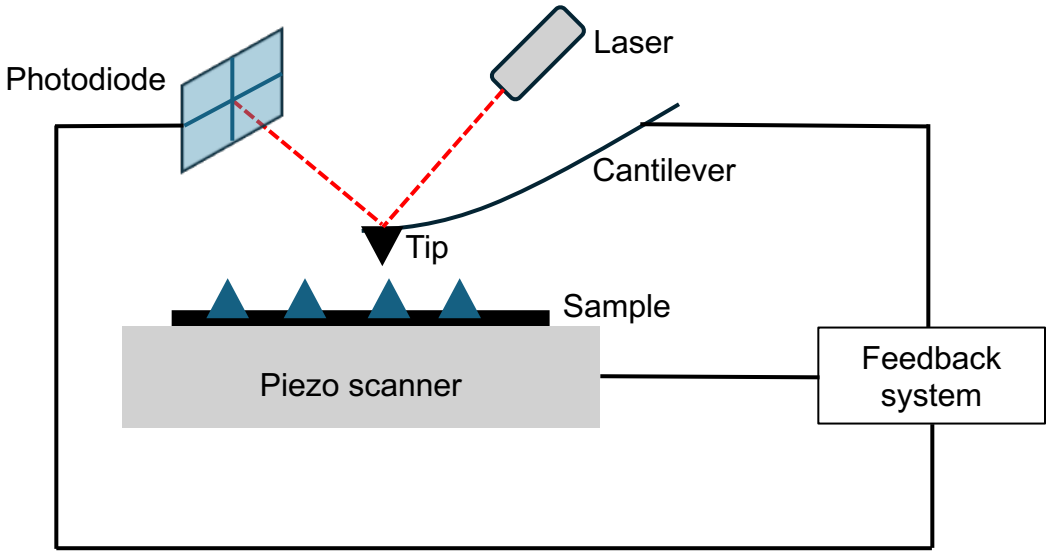


Figure 9. Schematic of atomic force microscopy

There are three modes in which the AFM is operated: [51]

- Contact mode: In this mode, the distance between the tip and the samples is kept constant by piezoelectric adjustment of the sample position in the vertical direction. Since the distance between the sample and the tip is very small, the repulsive forces become dominant. However, this mode can damage sensitive samples.
- Non-contact mode: The cantilever with the tip is kept in oscillation at its resonance frequency just above the sample surface. When the distance between the tip and the sample changes,

the frequency of the oscillation is changed accordingly. A feedback loop is used to adjust the sample position and maintain a constant frequency.

- Tapping mode: In this mode, the oscillation of the cantilever is kept constant as in the non-contact mode, however the oscillation frequency is much higher. The tip approaches the surface by lightly tapping the surface so that repulsive forces become significant. Depending on the sample topography, the oscillation of the cantilever changes, which is then adjusted using a feedback loop and recorded to produce the final image.

In this thesis the microstructure and roughness of the deposited films were studied using atomic force microscopy (Bruker, Dimension FastScan) using the Bruker's ScanAsyst mode, which is a proprietary Bruker algorithm that uses the advantages of both the contact mode and tapping mode. However, unlike tapping mode, the cantilever operates in non-resonant mode thus avoiding filtering effects and also gives an advantage of direct force control. The key parameters are automatically selected and constantly adjusted without any manual intervention. For this study, the scan frequency was kept constant and was set to 0.5 Hz and the lines per scan was kept constant at 512 unless otherwise stated. The images were processed using Nanoscope Analysis software. Usually, the processing steps included flattening or levelling the images to correct unevenness caused during the scanning process. The threshold for flatness was adjusted to the images and varied. The built-in tools, such as roughness measurement and section analysis, were used. To determine the film roughness, the images were cropped, and the substrate was neglected during roughness calculations.

2.3.2 Ellipsometry

Ellipsometry is an optical tool that uses the change in polarization state to measure the thickness and optical constants of a thin-film sample. An elliptically polarized light was shined on the sample surface and undergoes changes in the phase and amplitude.[52] This change in polarization state is measured in terms of Ψ and Δ, representing the amplitude ratio and phase difference respectively, between the p- and s-polarized components of the reflected or transmitted light.[53] A mathematical model is constructed based on the Fresnel equation to predict the optical constant of the film. By fitting these predicted values to the experimental values, an estimation of the optical constants and the thickness are obtained.[52] For this work, a Filmsense FS-1 ellipsometer was used with a standard built in model "SiO2 on Si" for measuring the thickness of SiO_x films.

2.3.3 X-ray photoelectron spectroscopy

X-ray photoelectron spectroscopy (XPS) is a surface-sensitive chemical analysis tool. The working principle of XPS is based on the photelectric effect. When x-rays of known energy bombard the surface of the material, it leads to absorption of part of this energy by the electrons of the sample (in the form of kinetic energy) and the electrons can be ejected from the sample (Figure 11).[54] Almost all the elements from the periodic table (except for H_2 and He) can be measured/characterized using XPS.

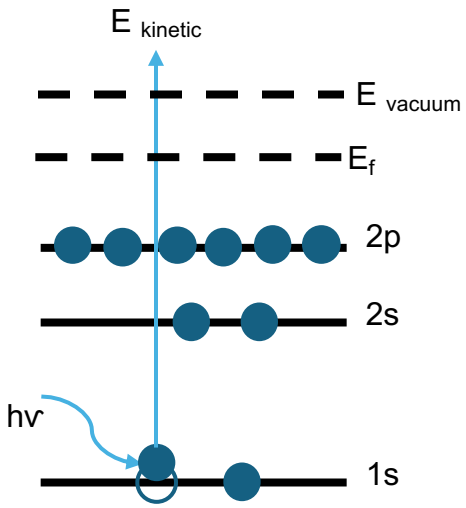


Figure 10. Emission of a photoelectron during XPS

The energy of the bombarding x-ray is given by:[54]

$h\nu$ = Binding Energy + Kinetic Energy + Work function of spectrometer (constant)

Given all the knowns, i.e., the wavelength of the incident beam and the work function of the spectrometer, the kinetic energy of the outbound beam is measured during the experiment. Later, binding energy can be calculated from the above equation and hence the element along with its chemical state can be determined.

In this work, XPS measurements were conducted using a Nexsa G2 Surface Analysis System from Thermo Scientific. The X-ray source used was monochromatic Al K-alpha (10 - 400 µm spot size). The results were analyzed using CasaXPS software and the energy scale was calibrated using C1s as the reference.

2.3.4 Scanning electron microscopy and energy dispersive x-ray spectroscopy (SEM/EDS)

Scanning electron microscopy (SEM) is an imaging technique which uses an electron beam to image the surface of the sample. The electron beam rasters over the surface and interacts with the atoms of the sample. It mainly uses two types of signals to produce images, namely, secondary electrons and backscattered electrons. Secondary electrons are produced from the sample as a result of inelastic interaction and contain topographical information, whereas the back scattered electrons are the electrons reflected after elastic interaction between the sample and the electron beam.[55] Since the back scattering depends on the mass of the nucleus, it contains compositional information, producing a different contrast than the secondary-electron topography contrast image.

During the interaction between the electron beam and the sample, characteristic x-rays, unique to each element, are also produced. The energy of the x-rays and their intensity are detected and measured to produce an elemental map. This technique is known as energy dispersive spectroscopy (EDS).[56]

SEM/EDS are usually used as a combined technique to analyze both the topographical and compositional information of the materials. In this study, a Merlin SEM (Zeiss) was used with an electron beam energy of 2kV. EDS data were obtained with an EDAX Octane detector.

2.3.5 Raman spectroscopy

Raman spectroscopy is a non-destructive analytical technique based on the Raman scattering effect first introduced by the Indian Physicist, C.V. Raman. It is based on the observation that when molecules interact with light, they scatter light in all directions. Much of the scattered light has the same frequency as the incident light, however a small fraction of scattered light has a change in frequency due to in-elastic collisions between the incident light and the molecules in the sample.[57] Therefore, we can say that the energy of the scattered photon after inelactic interaction is $h\nu - E_{vibration}$, where $E_{vibration}$ is the energy of a phonon generated during this process. This frequency shift is unique to the materials and is measured as the Raman shift.

For the characterization of 2D materials, Raman spectroscopy is known to be a very important technique. Based on Raman spectroscopy, one can comment on the number of layers in the material, the effect of doping, stress-strain properties, presence of defect etc.[31,58–60] MoS_2 and WS_2 have similar in-plane E^1_{2g} and out-of-plane A_{1g} modes due to their similar crystal structures. The in-plane mode is

more sensitive to the strain in the materials whereas the out-of-plane mode is known to be more sensitive to the doping effect in both the materials.[31,59,60]

Raman spectra were measured using a Renishaw inVia Reflex system, which comes with a sample stage capable of 100 nm positioning accuracy across three dimensions. A 532 nm laser (Renishaw DPSSL) filtered to 5% intensity was focused on the samples, with a 2400 lines/mm grating used to analyze Raman-scattered light.

2.3.6 Photoluminescence spectroscopy

Photoluminescence spectroscopy (PL) is another important analytical tool to characterize 2D materials. In this method, a laser beam is shined on a sample, which absorbs and then emits photons. The absorbed photons excite electrons in the material from the valence band to the conduction band. When these electrons return back to their original state, they emit energy in the form of light (photons). The energy of the emitted photons provides information about the electronic properties of the material.

The electron-hole pair generated during the excitation process may form quasi-particles, such as excitons, trions, bi-excitons etc. The formation of quasi-particles is less stable in bulk materials due to dielectric screening. However, in 2D materials, due to quantum confinement, the dielectric screening becomes negligible, and these quasi-particles become stable and play a major role in determining the electronic and optical properties of the 2D materials. Therefore, PL spectroscopy is an invaluable tool for understanding various properties of 2D materials, including the excitonic behavior, band gap, defect states etc.

In this study, the same Renishaw inVia Reflex system was used for PL measurements. The wavelength and the intensity of the laser were kept the same for PL measurements, and the grating was changed to 1800 lines/mm.

Chapter 3

Atmospheric pressure spatial atomic layer deposition of silicon oxide using DIPAS and ozone

3.1 Introduction

Thin-film silicon oxide (SiO_x) is a highly versatile material that finds use in many different areas of nanotechnology, including dielectric materials in microelectronic devices,[61] electrode materials for supercapacitors,[62] nanocoating films for barrier applications and many more.[63] However, its conventional growth and deposition methods often require very high temperature, or the use of plasma, as mentioned previously in section 1.2.1.

3.2 Precursor selection

Given the versatility of SiO_x, various silicon-based precursors have been investigated. Some of the important conventional precursors which have been widely studied using CVD and conventional ALD include heterosilanes like SiH_4[64] and halide-based precursors like $SiCl_4$,[65] SiH_2Cl_2,[66] and Si_2Cl_6.[67] While these precursors produce high-quality films, they pose risks of film contamination due to adsorption of by-products when deposited at low temperatures. The by-products released are also hazardous and thus should be avoided for open-air, high-throughput processes such as AP-SALD.

A preliminary screening was carried out to assess possible silicon precursors for use specifically in AP-SALD. The organosilanes class of Si precursors, such as tetraethoxyorthosilicate (TEOS),[68] bis(diisopropylamino)disilane (BDIPADS),[69] bis(dimethylaminosilane) (BDMAS),[70] and trivinylmethoxysilane (TVMS)[24] emerged as promising candidates. Diisopropylamino silane (DIPAS) (Figure 12), one of these amino silane organic precursors, has a high vapor pressure of ~23 torr at room temperature, is non-pyrophoric, and is not expected to produce any harmful reactive byproducts, making it well-suited for AP-SALD.[71] Therefore, DIPAS was synthesized in this work for the development of a plasma-free AP-SALD process.

Various conventional ALD studies have been conducted using DIPAS. For instance, the study by Nam et al. and another similar study[72,73] reported the deposition of SiO_x films using DIPAS and ozone. However, films could not be deposited below 100°C.[72,73] Plasma was required to reduce the deposition

temperature; for instance, Lee et. al. deposited SiO_x films using DIPAS and oxygen plasma at 60°C using conventional ALD.[74]

To address these challenges, in this study, I use a custom-built AP-SALD system to test the plasma-free deposition of SiO_x using DIPAS and either ozone or 30% hydrogen peroxide aqueous solution (peroxide-30) as the oxidant. I conduct a systematic study of this plasma-free process to understand the effect of various parameters such as temperature, precursor flow rate, and oxidant flow rates on the composition and morphology of the deposited materials.

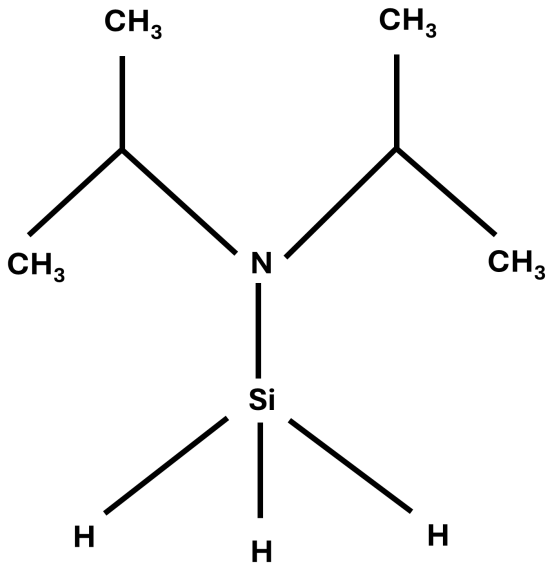


Figure 11. Diisopropylamino silane (DIPAS) molecular structure.

3.3 DIPAS synthesis

DIPAS was synthesized in a two-step process – $SiCl_4$ and diisopropylamine reacted to form 1,1,1-trichloro-N, N-diisopropylsilanamine ($C_6H_{14}Cl_3NSi$) which was then reduced to DIPAS ($C_6H_{17}NSi$) in a second step (Figure 13a).

An oven-dried, 3-neck, 3-L round-bottom flask was filled with 1.2 L of anhydrous pentane followed by the addition of 100 g of $SiCl_4$. 250 ml of diisopropylamine was added to the silicon chloride solution, resulting in vigorous evolution of HCl along with salt formation ($C_6H_{14}Cl_3NSi$) after continuous

overnight stirring. The excess pentane was distilled off. This salt mixture was dissolved in ~500 mL of dry tetrahydrofuran (THF).

Later, 18.5 grams of $LiAlH_4$ (Pellet form, Aldrich product 323403) was dissolved separately in 500 mL of THF to form a suspension. This suspension was added slowly to the $C_6H_{14}Cl_3NSi$ salt mixture at -1°C with temperature rising to 13°C later. The reaction mixture was a grey slurry. This mixture was stirred overnight at room temperature. The volatiles were distilled from this solution. Later, excess THF was removed by distillation, leaving behind 46.2 grams of colorless liquid, DIPAS. The ^1H NMR spectrum confirmed the formation of DIPAS with small amount of THF (~7%) (Figure 13b).

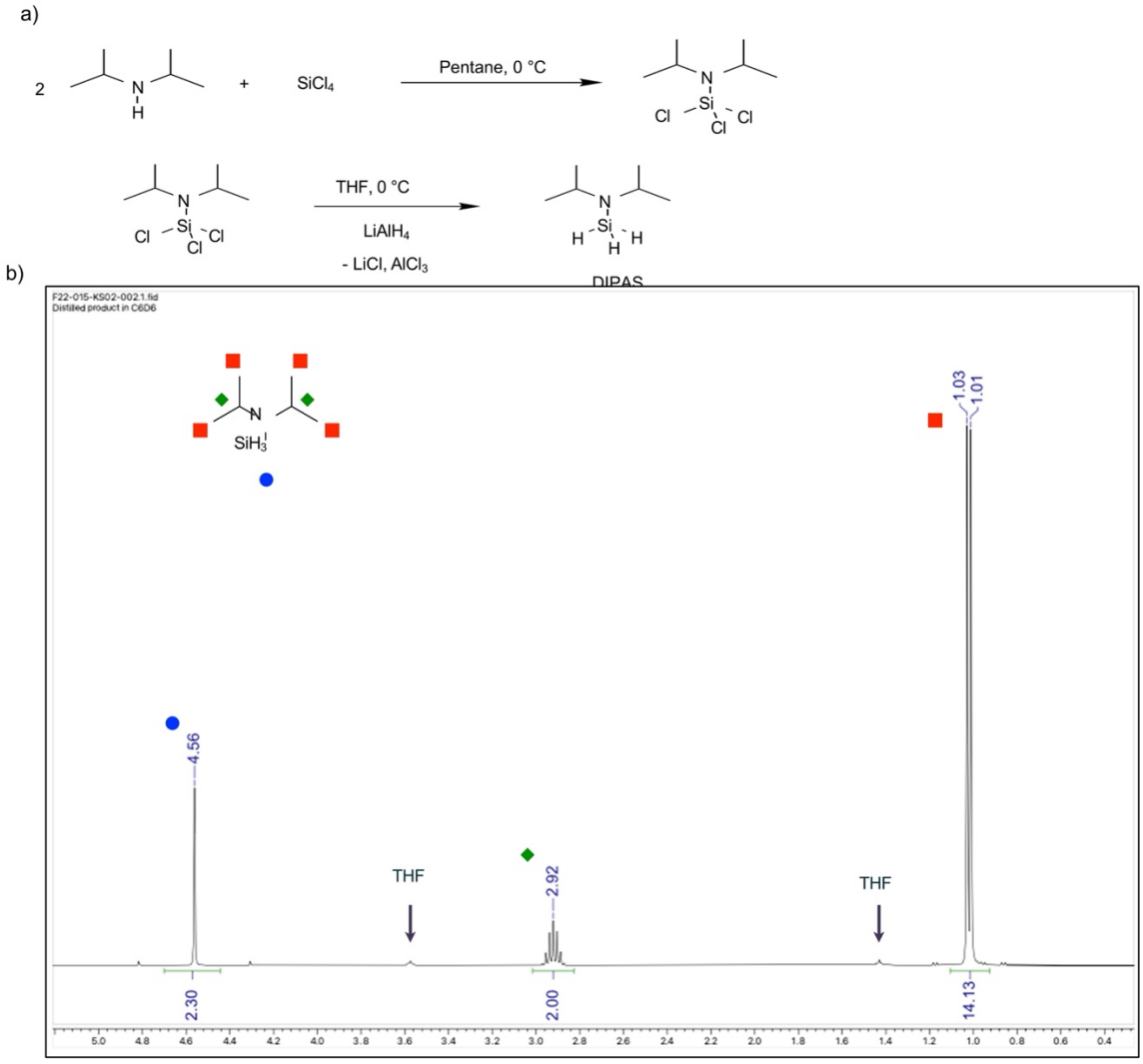


Figure 12. (a) Reaction scheme for DIPAS synthesis. (b)1H NMR spectrum for DIPAS.

3.4 Film Characterization

The ellipsometry, AFM, SEM/EDS measurements were performed on silicon wafer (76.2mm Si, N-type wafer, P doped <100>, 1-10ohms-cm, SSP prime). The XPS measurements were conducted on ITO/glass substrates from Delta Technologies Limited (polished float glass, 16 x 16 x 1.1 mm, SiO_2 passivated/indium tin oxide coated on polished surface).

3.5 Results and discussion

3.5.1 Peroxide-30 as an oxidant

As an initial step, I examined the interaction of DIPAS with peroxide-30, a mild oxidant. I found that DIPAS showed minimal reactivity with peroxide-30 at temperatures below 50°C. At room temperature, AFM analysis revealed that nano crystallites were deposited on a silicon substrate (Figure 14a). At this temperature, the deposition process is expected to be in the precursor-condensation regime. The precursor molecules were primarily physically adsorbed onto the substrate surface, which facilitated a degree of reactivity, leading to the formation of the nano crystallite phase. However, the lack of thermal energy is expected to lead to accumulation of contaminants, such as unreacted ligands from the precursor.

XPS was conducted to assess the composition of the nano crystallites deposited at room temperature. Figure 14b presents the XPS survey. The Si signals were weaker than those from SiO_x films grown using ozone, as discussed later, implying a smaller amount of Si was present in the nano crystallites. The broad Si 2p spectrum (Figure 14c) was deconvoluted into multiple peaks. The peak at 103.3 eV was attributed to SiO_2, while the peak at 102.11eV might correspond to aminosilane on SiO_2.[75] The peak at 105.8 eV was attributed to the presence of Si^{+3} of SiO_2 and SiO_x ($x<2$).[76,77] In Figure 14d, the deconvoluted peaks of the O 1s spectrum at 530.43 eV and 531.28 eV are related to the ITO/glass substrate,[78] and the peak at 532.88 eV was related to the strong Si-O bond in SiO_2.[79] The XPS survey also showed the presence of a high carbon content as compared to the amorphous film formed using ozone that will be discussed in Figure 19a. Similarly, I observed a very small peak at ~400 eV (inset of Figure 14b), which indicated the presence of nitrogen. It was observed that this peak was not present in the films deposited using ozone as the oxidant (Figure 19a). The excess carbon and nitrogen are consistent with condensation of the DIPAS. It was reported that the desorption energy of the primary by-product, di-isopropylamine (DIPA), is relatively high (~0.40 eV) due to the presence of a lone pair of electrons on the N atom, inhibiting the adsorption of new DIPAS molecules, depending on the configuration.[80] This makes the formation of a dense film difficult, leaving organic contaminants behind.

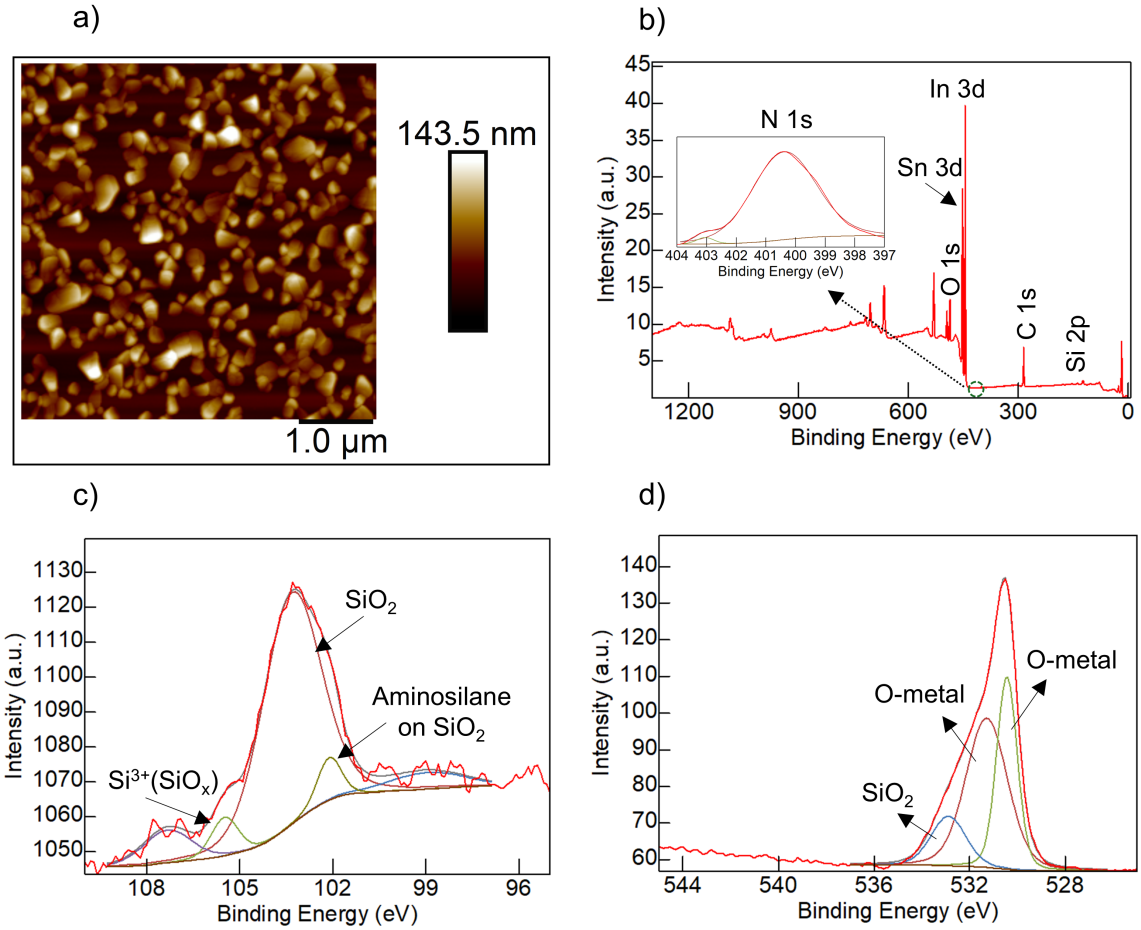


Figure 13. Nano crystallites deposited using DIPAS and peroxide-30 at room temperature. (a) AFM image on silicon substrate. (b) XPS survey, (c) Si 2p spectrum, and (d) O 1s spectrum on an ITO/glass substrate.

XRD was used to examine the structure of the nano crystallites (Figure 15). Additional diffraction peaks at 2θ angles of 24.9° and 34.4°, as compared to the XRD pattern of an amorphous SiO_x film deposited using ozone (Section 3.5.2), confirmed the formation of a crystalline phase. Most of the peaks that appear are from the substrate (Si- wafer); the peak at 29.05° might be due to the presence of SiO_x.[81] The peak at 24.9° was tentatively attributed to ethanolamine silicon oxide (JCPDS 00-051-1423), based on analysis using X'pert Pro software. However, the origin of the peak at 34.4° remains undetermined. As continuous SiO_x films are ultimately desired, I next investigated depositions at higher temperatures with DIPAS and peroxide-30.

As the substrate temperature was increased up to 50°C, no reaction occurred between DIPAS and peroxide-30. A transition from the precursor-condensation regime to the atomic layer deposition (ALD) regime is expected at higher temperatures. In the ALD regime, the precursor molecules may undergo a self-limiting chemical reaction with the substrate, resulting in the formation of a monolayer of silicon oxide. However, this reaction is highly sensitive to the oxidizing power of the oxidant used. The first-principles study by Lee et al stated that the Si-H bond cleavage (by oxidation) of SiH_3 adsorbate has a high activation energy of 1.19 eV and is the rate-determining step in the deposition process.[82] Therefore, we can conclude that hydrogen peroxide and water, due to their relatively weak oxidizing properties, are ineffective to oxidize the DIPAS molecule in the desired low-temperature ALD regime.

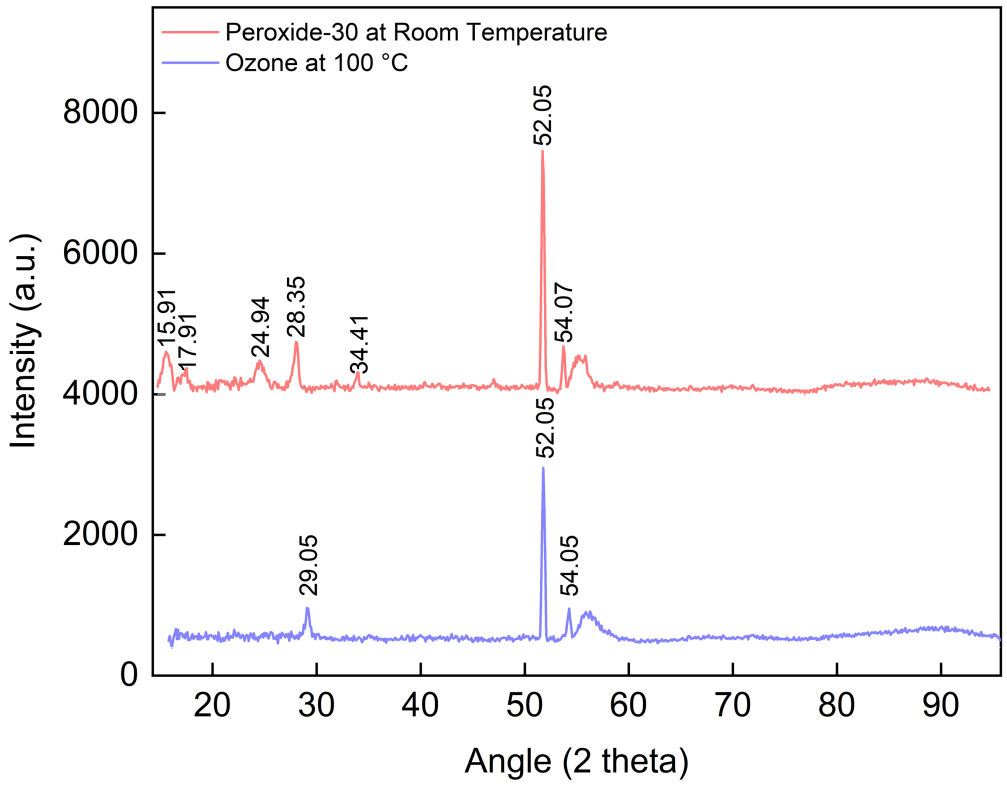


Figure 14. XRD data for depositions at room temperature using DIPAS and peroxide-30 and using DIPAS and ozone at 100°C.

3.5.2 Ozone as an oxidant

Due to the inability to get a continuous film with peroxide-30 at the low temperatures of interest, I transitioned to a more potent oxidizing agent, ozone. The effect of ozone concentration and temperature were studied (Figure 16a) by varying the ozone-generator voltage from 10V to 80V and the temperature from room temperature to 100°C. The DIPAS bubbling rate was kept constant at 100 sccm, and depositions were performed for 300 cycles.

At lower temperatures (i.e., 28°C and 50°C), a cloudy film texture was observed, similar to that seen with peroxide-30, and the film thickness increased with increasing ozone voltage, as shown in Figure 16a. However, ellipsometry analysis using the standard "silicon dioxide on Si" model showed a high fit error, indicating a complex film structure (Figure 17a). The continuous increase in GPC with ozone voltage at 28°C and 50°C suggested that ALD-type growth was not occurring. Indeed, the measured GPCs at the higher ozone voltages are larger than what is expected for ALD of SiO_x.

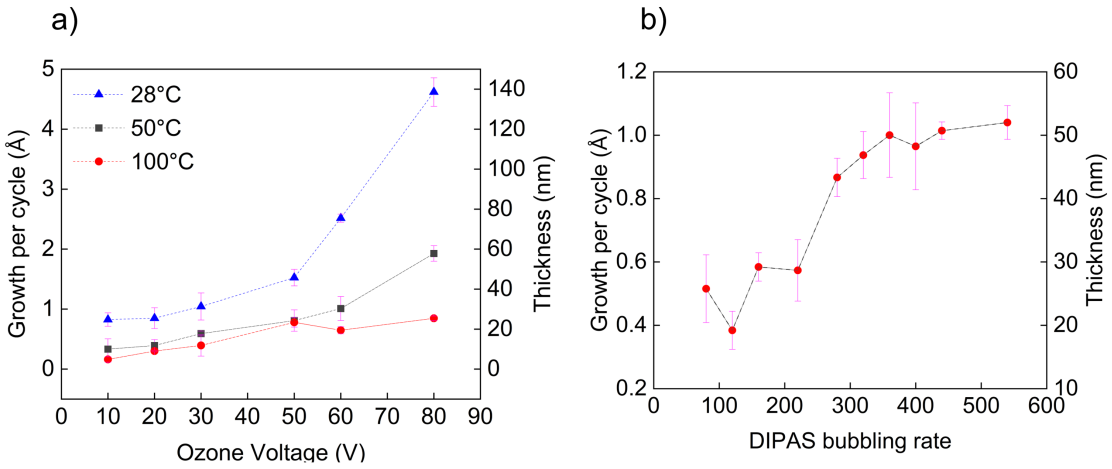


Figure 15. Depositions using DIPAS and ozone. (a) Thickness and GPC as a function of ozone-generator voltage and deposition temperature. (b) Thickness and GPC as a function of DIPAS bubbling rate.

At a substrate temperature of 100°C, an improved film texture was observed (Figure 17b). The GPC increased slightly as the voltage was increased from 10 V to 50 V. This was expected; as the oxidant concentration is increased, the probability of DIPAS molecules reacting with ozone molecules should increase, leading to a higher GPC. However, beyond 50 V, the GPC stabilized at approximately 0.8 Å/cycle. This is slightly less than the GPC of 1.2 Å/cycle at 150°C that has previously been reported

for SiO_x,[83] suggesting that the 100 sccm bubbling rate might not be delivering sufficient precursor to saturate the surface.

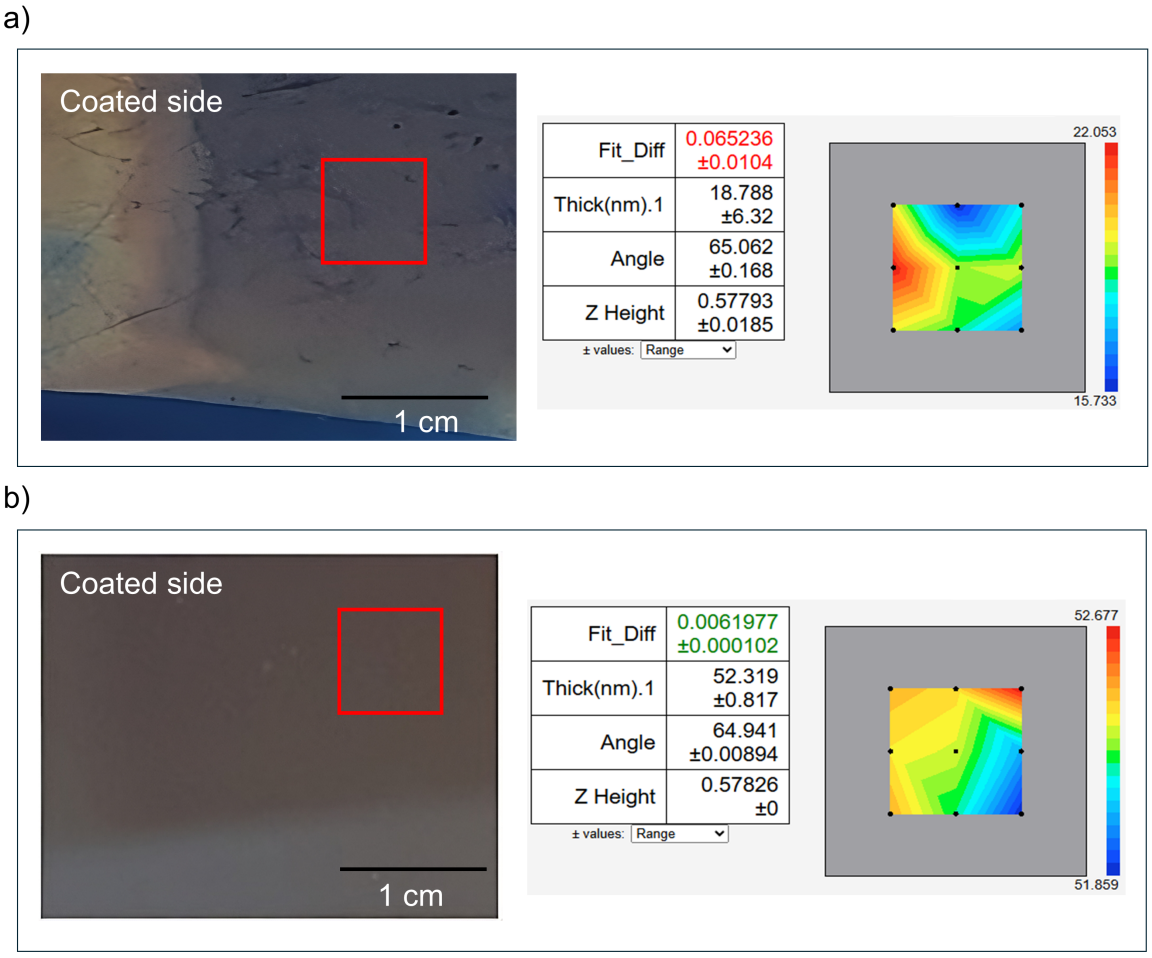


Figure 16. (a) Cloudy film texture as observed by eye at T= 28°C. b) Dark grey SiO_x film texture as observed by eye at T= 100°C.

Therefore, I fixed the ozone-generator voltage at 30 V and the deposition temperature at 100°C and systematically varied the DIPAS bubbling rate to verify if the deposition process was occurring under ALD conditions (Figure 16b). The number of cycles were kept constant at 500, and the DIPAS carrier-gas flow rate was adjusted accordingly to make sure the total flow from the DIPAS channel was kept constant at 800 sccm. It was observed that as the DIPAS bubbling rate was increased from 80 sccm, the growth per cycle increased, which implies that the surface was not fully saturated. At a DIPAS bubbling rate of 400 sccm, the GPC saturated at ~1 Å/cycle, implying complete saturation of the

surface. Notably, this GPC of ~1 Å /cycle achieved for AP-SALD with DIPAS and ozone is similar to what has been reported in the literature for temporal ALD.[83] However, the rate of deposition was ~0.5 Å /sec, based on a 2-second cycle duration, whereas temporal ALD studies employing DIPAS and ozone reported cycle times of 23 to 32 seconds, including purging time.[72,80] This deposition rate could be further optimized in the future and highlights the rapid nature of AP-SALD.

Having observed the ability to achieve ALD-type growth with DIPAS and ozone, I studied the microstructure of these films as a function of the deposition temperature (Figure 18) to better understand the growth window. The DIPAS bubbling rate was set to 80 sccm, the DIPAS carrier flow was set to 800 sccm, the ozone-generator voltage was set to 40V, and the depositions were carried out for 300 cycles. Figure 18e shows that at 100°C, an amorphous, smooth, pinhole-free SiO_x film with an average roughness of 0.3±0.03 nm was obtained. The lowest temperature to get an amorphous SiO_x film was observed to be 70°C (Figure 18d). The GPC was unchanged at 70°C (Figure 18f) and only a slight increase in surface roughness to 0.5±0.3 nm was observed. This deposition temperature is lower than what has been reported in the literature by Nam et al. Their study showed that the lowest temperature possible to deposit SiO_x via conventional ALD using DIPAS and ozone was 100°C. The ability to deposit at 70°C increases the range of temperature-sensitive substrates to which amorphous, ALD-quality SiO_x films can be applied.

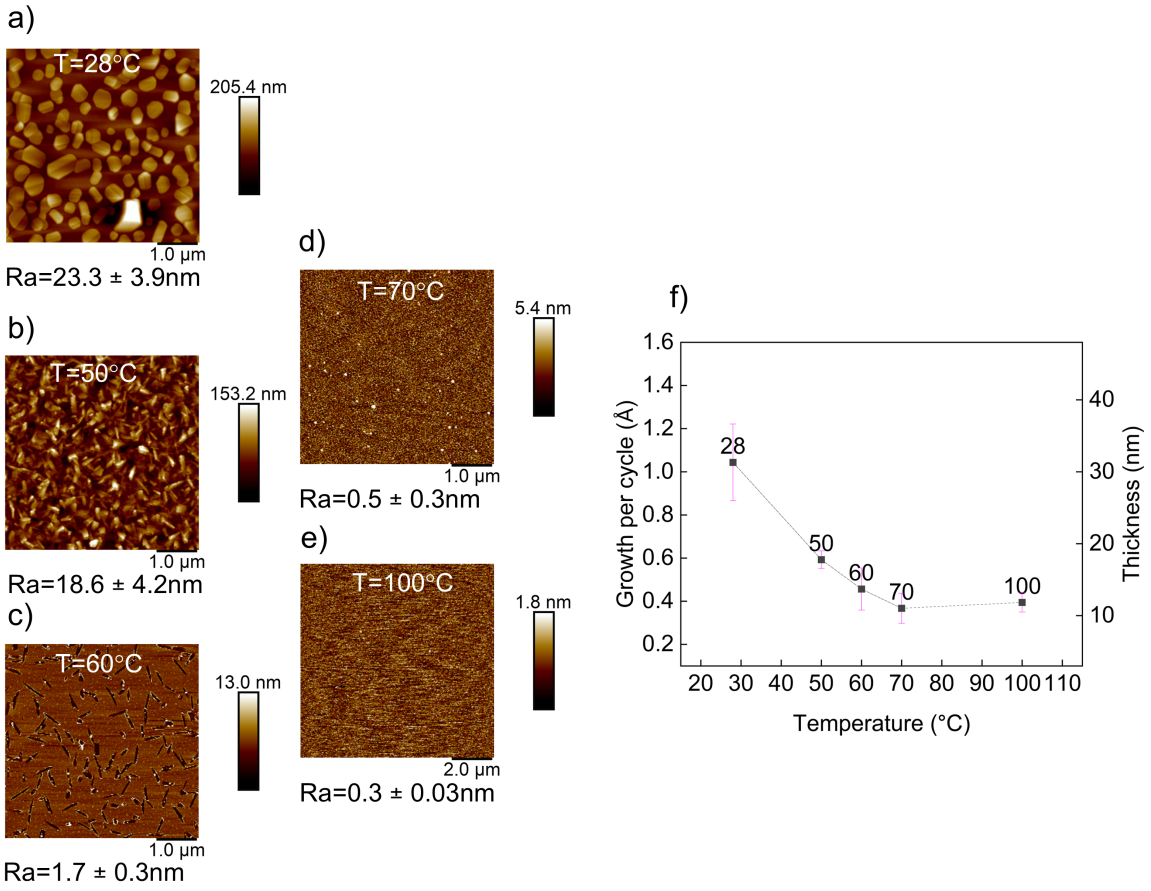


Figure 17. Microstructures produced using DIPAS and ozone at different temperatures.

It is seen in Figures 18a-c that at deposition temperatures below 70°C, the structure became more crystalline, similar to the nano crystallites produced using peroxide-30. I suspect that a similar phenomenon of precursor condensation was occurring. To confirm the composition of the amorphous films and the nano crystallites, XPS and EDX were conducted.

XPS of a film deposited on ITO/glass at 100°C with ozone as the oxidant is shown in Figure 19. The film was deposited in the same manner as those in Figure 18. The XPS survey in Figure 19a clearly indicates the presence of silicon oxide. It can also be seen that signals from In and Sn are almost negligible, implying that the SiO_x film entirely covers the substrate, as expected. In Figure 19b the Si 2p peak was deconvoluted. The peaks at 103.06 eV and 103.69 eV indicate the presence of SiO_2 thin

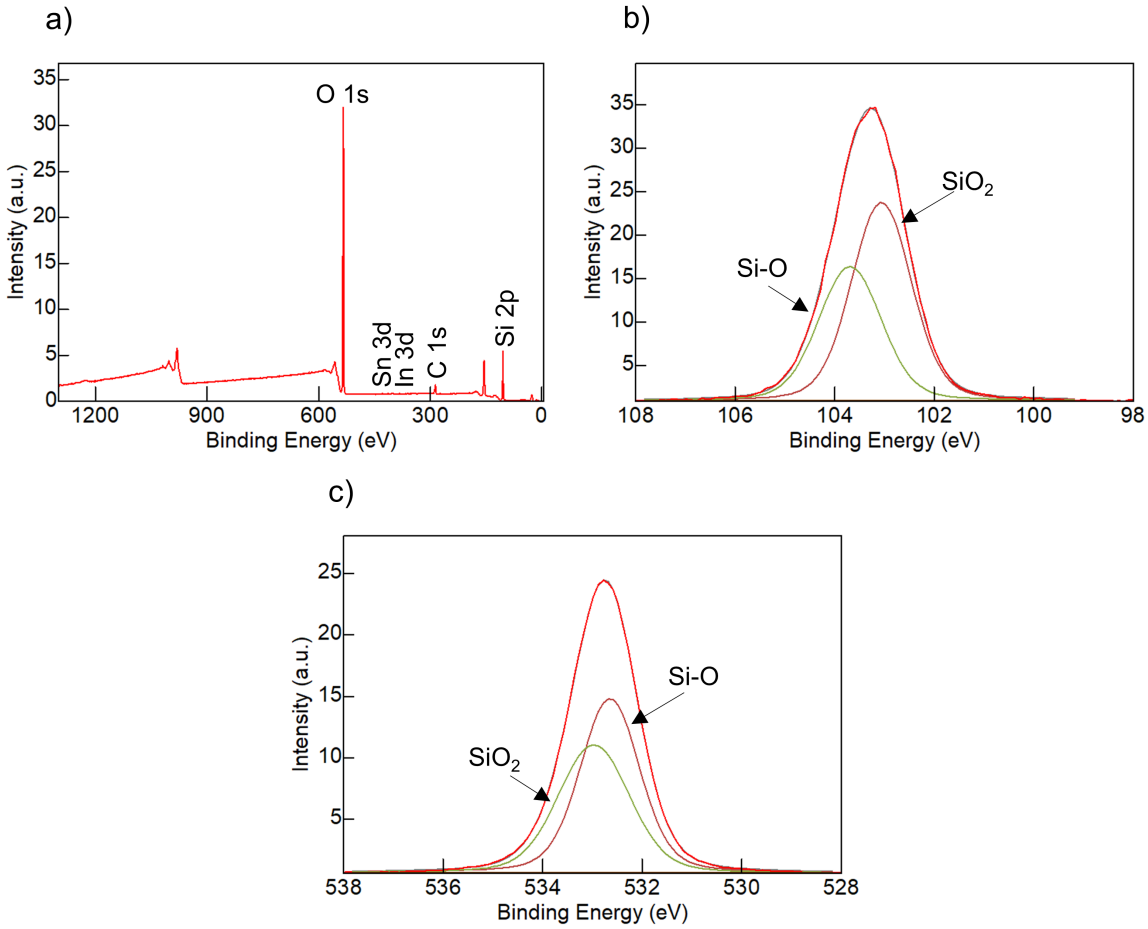
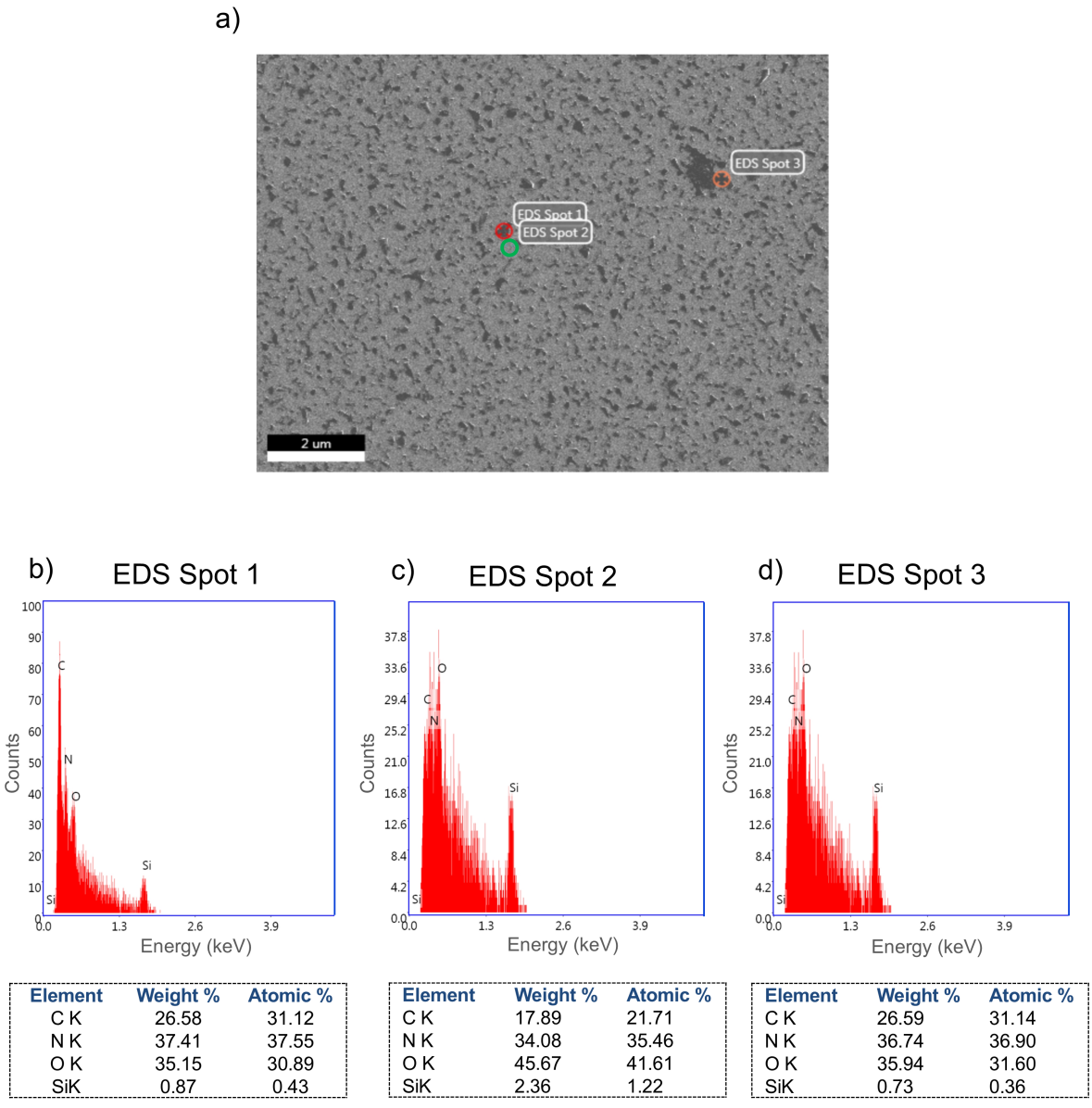


Figure 18. (a) XPS survey, (b) Si 2p spectrum, and (c) O 1s spectrum for a silicon oxide film deposited using DIPAS and ozone at 100°C on an ITO/glass substrate.

film and Si-O bond.[84,85] Similarly, the O 1s peaks at 532.6 eV and 532.9eV in Figure 19c show the presence of the non-bridging oxygen, Si-O, and SiO_2 bond respectively.[86,87] The carbon peak at ~285eV has a reduced intensity compared to that observed for the nano crystallites formed with peroxide-30 (Figure 14b), suggesting significant precursor condensation was avoided. XPS was not used for the samples deposited at low temperatures, as these had very small crystallite sizes (Figure 19a-c). This would result in the majority of the XPS signal originating from the ITO/glass substate. Hence EDS was used for compositional analysis of the nano crystallites.

Figure 20a shows a back-scattered SEM image of the nano crystallite phase formed at room temperature on a Si substrate using DIPAS and ozone. A 2 keV electron beam was used to reduce the depth of penetration and probe the sample and not the substrate. Spot 1 and spot 3 include areas covered

by the nano crystallite phase, whereas spot 2 is focused on the area not covered by this phase. Spot 1 and spot 3 show a high presence of carbon and nitrogen, exhibiting N:Si ratios of 43 and 50.3, respectively, compared to spot 2 which contains less carbon and nitrogen (N:Si ratio of 14.4). Hence, the nano crystallite features at spots 1 and 3 are contaminated with nitrogen-containing compounds, suggesting the presence of unreacted or partially reacted DIPAS. This suggests that at lower temperatures the by-product desorption is difficult, even with the use of ozone, which eventually leads to formation of a complex Si compound. As previously mentioned, this has been reported in various theoretical studies on DIPAS, which stated that the desorption of by-products and oxidation of the Si-H bond are the most-energy-consuming steps. [73,88]



Element	Weight %	Atomic %
C K	26.58	31.12
N K	37.41	37.55
O K	35.15	30.89
SiK	0.87	0.43

Element	Weight %	Atomic %
C K	17.89	21.71
N K	34.08	35.46
O K	45.67	41.61
SiK	2.36	1.22

Element	Weight %	Atomic %
C K	26.59	31.14
N K	36.74	36.90
O K	35.94	31.60
SiK	0.73	0.36

Figure 19. (a) Backscattered SEM image of nano crystallites deposited on a Si substrate at room temperature using DIPAS and ozone. EDS spectra at (b) spot 1 – nano crystallite phase, (c) spot 2 - substrate, and (d) spot 3 - nano crystallite phase.

Chapter 4

Rapid nucleation of ZnO deposited using an atmospheric-pressure spatial atomic layer deposition system on 2D -MoS_2 and WS_2

4.1 Introduction

Uniform deposition of metal oxides on 2D materials is essential to employ these materials in many applications, therefore in this chapter, I describe our study on the nucleation of zinc oxide on 2D TMDCs (MoS_2 and WS_2). ZnO was deposited using an AP-SALD system operated in AP-SCVD mode.

4.2 Results and discussion

4.2.1 ZnO nucleation on CVD-grown MoS_2 and WS_2

Figure 21a shows an AFM image of the pristine CVD-grown MoS_2 (CVD-MoS_2) with a flake edge and underlying Si substrate visible. Figures 21b-d show the nucleation and growth of ZnO on the CVD-MoS_2 as the number of AP-SCVD oscillations is increased from 25 to 60. A high density of nuclei is visible near the flake edge in Figures 21b-c, indicating that the nucleation initiated from these edges. The nucleation density and surface coverage increased with the increasing number of oscillations; however, the initial nucleation density was such that ZnO layer closure was not achieved after 60 oscillations (Figure 21d). The ZnO nuclei exhibited clustering on CVD-MoS_2. Figure 21b shows the AFM image and line scan after 25 oscillations of ZnO. Some initial clusters were visible, with lateral dimensions on the order of ~105 nm. After 35 oscillations, almost all ZnO nuclei were part of a cluster. This is evident from the AFM line scan in Figure 21c, as the lateral dimension of the clusters were now~175 nm. Furthermore, these clusters were seen to be connected together to form continuous ribbon structures (Figures 21c-d).

Figures 21e-h show equivalent AFM images and line scans for the nucleation and growth of ZnO on CVD-WS_2; however, the AFM scan size was reduced from 2 μm to 500 nm, as a higher density of smaller nuclei were observed than for CVD-MoS_2. This is evident by comparing the line scans (Figure 21b-c and 21f-g). The CVD-WS_2 line scans show ~17 peaks as compared to ~7 peaks in CVD-MoS_2. The smaller values of peak height, width and spacing between the peaks in the line scan suggest a

higher nuclei density of ZnO on CVD-WS_2. In contrast to the CVD-MoS_2, this higher initial nucleation density of ZnO on CVD-WS_2 led to complete layer closure for most of the CVD-WS_2 flakes after 60 AP-SCVD oscillations. A continuous ZnO layer is visible on the WS_2 surface in Figure 21h and the line scan from that sample is noticeably smoother than the line scan of the CVD-MoS_2 after 60 oscillations (Figure 21d).

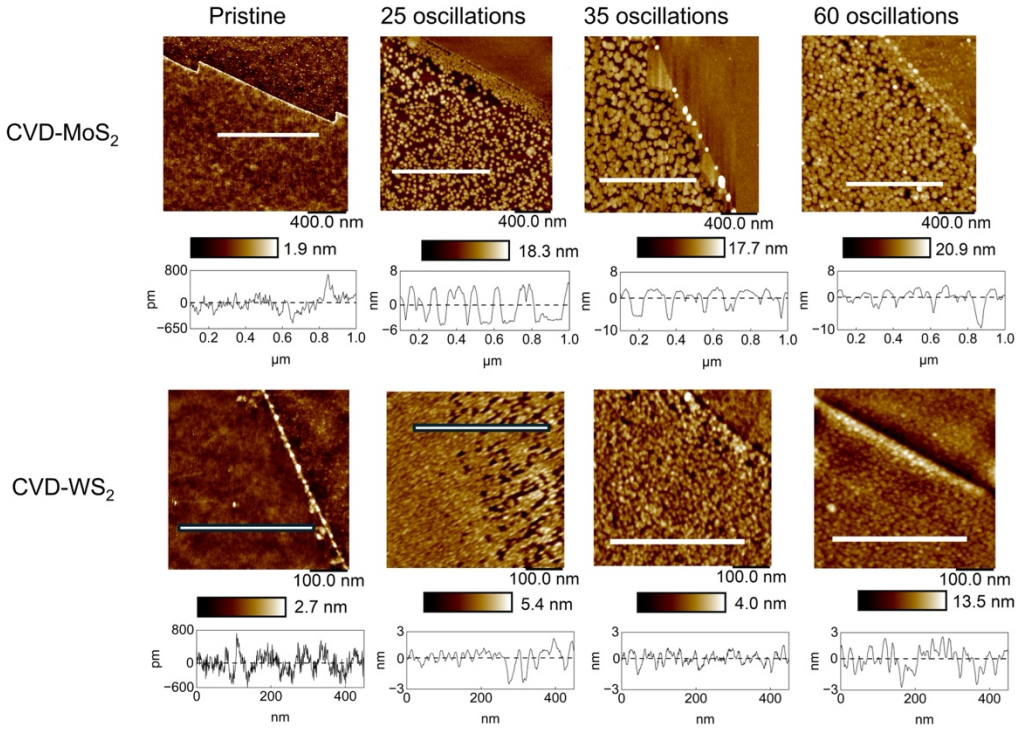


Figure 20. AFM images and line scans of CVD-grown (a-d) MoS_2 and (e-h) WS_2 with varying quantities of ZnO deposited via AP-SCVD.

Another notable difference from the nucleation on CVD-MoS_2 was the minimal nuclei clustering observed on the CVD-WS_2 in Figures 21e-h. This claim is supported by the line scan analysis, which showed nuclei clustering at irregular intervals and cluster widths that were ~8 times smaller than what was found for CVD-MoS_2. The ZnO clusters formed on CVD-WS_2 after 35 AP-SCVD oscillations, for example, were only ~20 nm in width (Figure 21g). To allow a more direct comparison, AFM scans for 35 oscillations of ZnO on CVD-MoS_2 and CVD-WS_2 are shown in Figure 22 under identical magnification. More significant nuclei clustering is clearly seen for CVD-MoS_2.

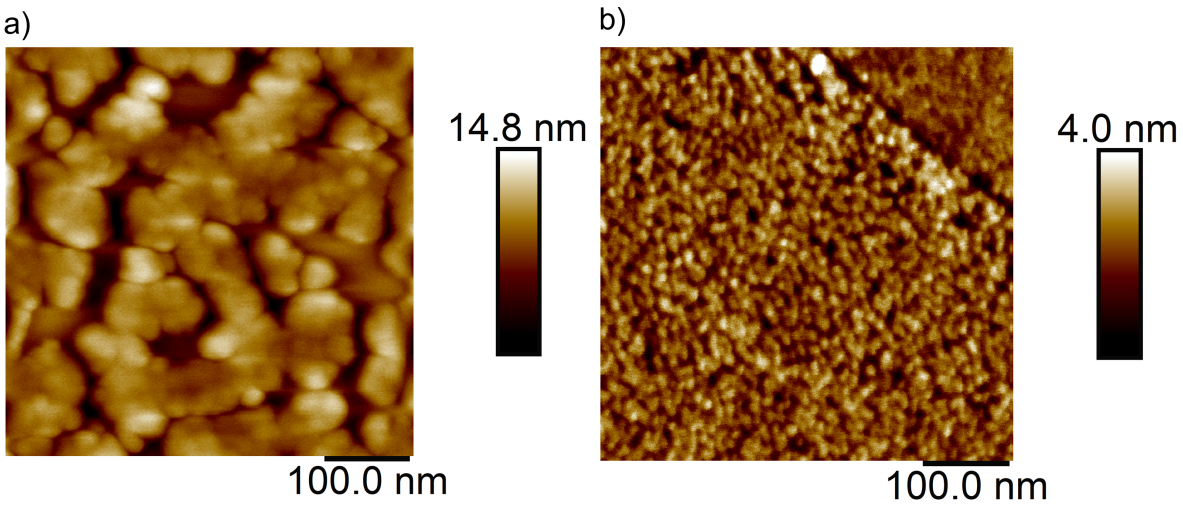


Figure 21. ZnO nucleation for 35 AP-SCVD oscillations on (a) CVD-MoS_2 and (b) CVD-WS_2. These measurements were done under similar conditions, i.e., similar deposition and AFM parameters (scan size, frequency etc.).

Park et.al showed that the adsorption energy of a precursor molecule has a strong dependance on the 2D material on which the deposition is performed. Since 2D materials have very low surface energy, the film formation is dominated by physisorption.[89] It was reported that van der Waal's physisorption of the adsorbate (precursor molecule) on a 2D material is primarily driven by a dipole-dipole interaction. The magnitude of the induced dipole polarization of the 2D material, caused by the adsorbate, governs the adsorption energy and thereby the film coverage.[89] It is known that the induced dipole polarization of a material is dependent on its electronic and atomic structure.[90] Therefore, in this case the heavy nucleus in W-based compounds is expected to exhibit a larger induced polarization than the lighter nucleus in Mo-based compounds, leading to higher adsorption energy and greater coverage.[89] This may explain the higher nucleation density and greater surface coverage observed for CVD-WS_2 (Figure 21h) than CVD-MoS_2 (Figure 21d).

The observed differences in nucleation density and ZnO film closure could also be influenced by different defects/impurities introduced in the CVD-WS_2 and CVD-MoS_2 samples during their respective synthesis processes. For example, exfoliated WS_2 (Figure 23) did not show complete ZnO coverage within 60 AP-SCVD oscillations. This may be attributable to the fact that the exfoliated

sample is expected to be better passivated, with less dangling bonds, making precursor adsorption difficult.

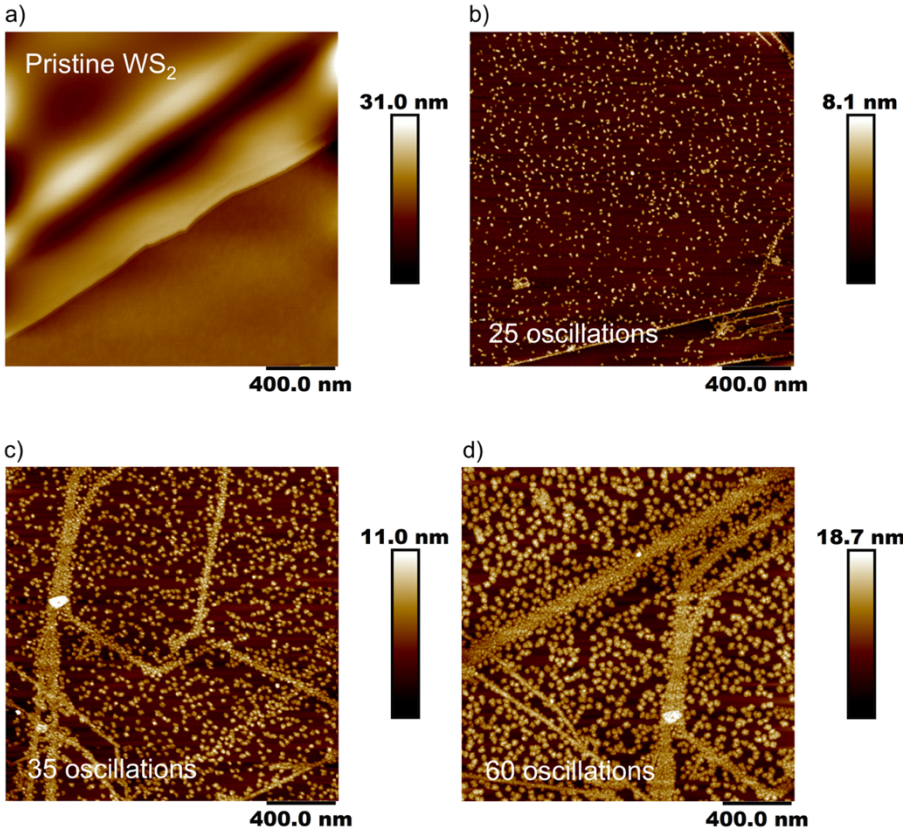


Figure 22. ZnO deposition on exfoliated WS_2 with varying numbers of AP-SCVD oscillations. (a) Pristine, (b) 25 oscillations, (c) 35 oscillations, and (d) 60 oscillations.

Apart from differences in nucleation density and layer closure, it was observed that the ZnO nuclei morphology was different on MoS_2 and WS_2. Larger clusters were formed on CVD-MoS_2, which grew into nanoribbons with a web-like network. A similar observation was reported by Zhang et al. for the nucleation of Al_2O_3 on MoS_2;[91] however, they used synthetic polycrystalline MoS_2 and the nucleation was predominantly observed on the grain boundaries and defects, leading to formation of nanoribbon structures, whereas single-crystal flakes were studied here.[18] The different ZnO clustering behavior observed here for AP-SCVD seemed to be material specific and not simply due to differences in defects/impurities, as it was also observed on exfoliated samples. ZnO nanoribbons were seen to be formed on exfoliated MoS_2 (Figure 24), whereas isolated nuclei were formed on exfoliated WS_2 (Figure

23). This might be due to a difference in the surface energy that makes nanoribbon formation more favorable on MoS_2. Other plausible reasons that can influence clustering could be different electronic properties at the ZnO-TMDC interface,[92] different surface interactions (e.g., van der Waal's forces) between the TMDCs and ZnO precursors, and local temperature variations arising from differences in thermal conductivity between CVD-grown MoS_2 (κ = 62.2W/m.K at room temperature on SiO_2/Si substrate) and WS_2 (15.4 ± 1.9 W/m.K at room temperature on SiO_2/Si substrate)[93] during deposition. Further investigation is required to understand the contributions of these factors.

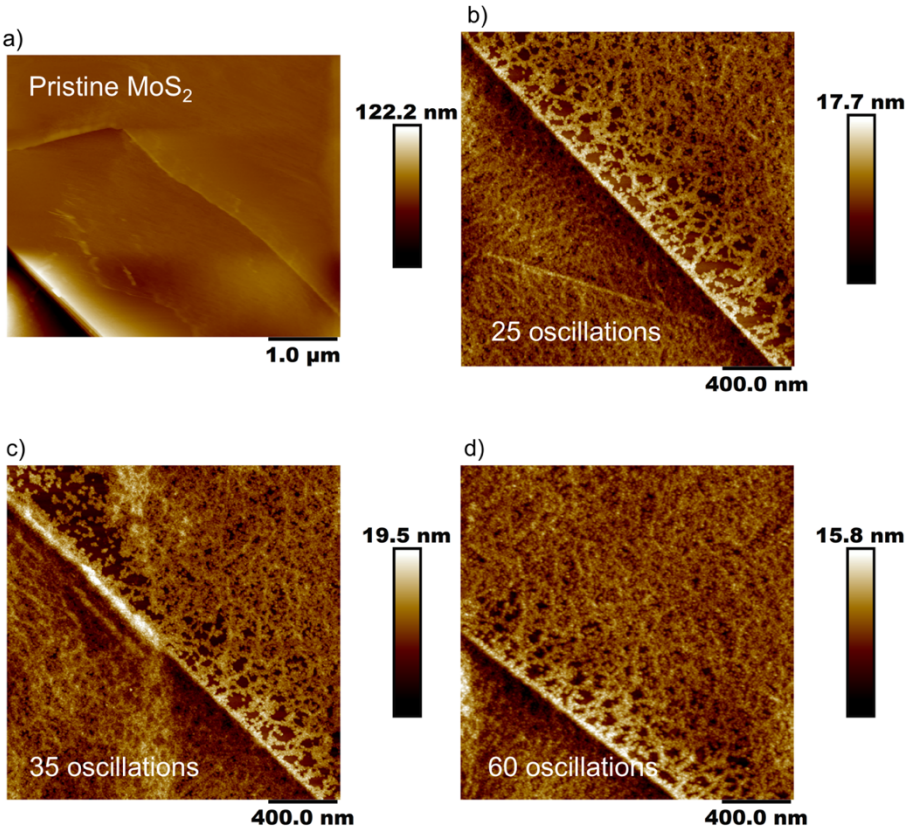


Figure 23. ZnO deposition on exfoliated MoS_2 with varying numbers of AP-SCVD oscillations. (a) Pristine, (b) 25 oscillations, (c) 35 oscillations, and (d) 60 oscillations.

To further investigate the early-stage nucleation, ZnO was deposited on a single-layered flake of CVD-MoS_2 using 5 AP-SCVD oscillations (Figure 25a) and a multilayered flake of CVD-WS_2 using 25 oscillations (Figure 25b). As noted earlier, the AP-SCVD nucleation is clearly seen to start at the edges of the CVD-grown TMDC flakes. This is consistent with previous reports for conventional ALD

and is attributed to the higher surface energy associated with the edges and defects, as compared to the more pristine basal plane.[91,94,95] ZnO nucleation might help to reduce the overall surface energy of these "defects", making the nucleation process energetically favorable at these sites.

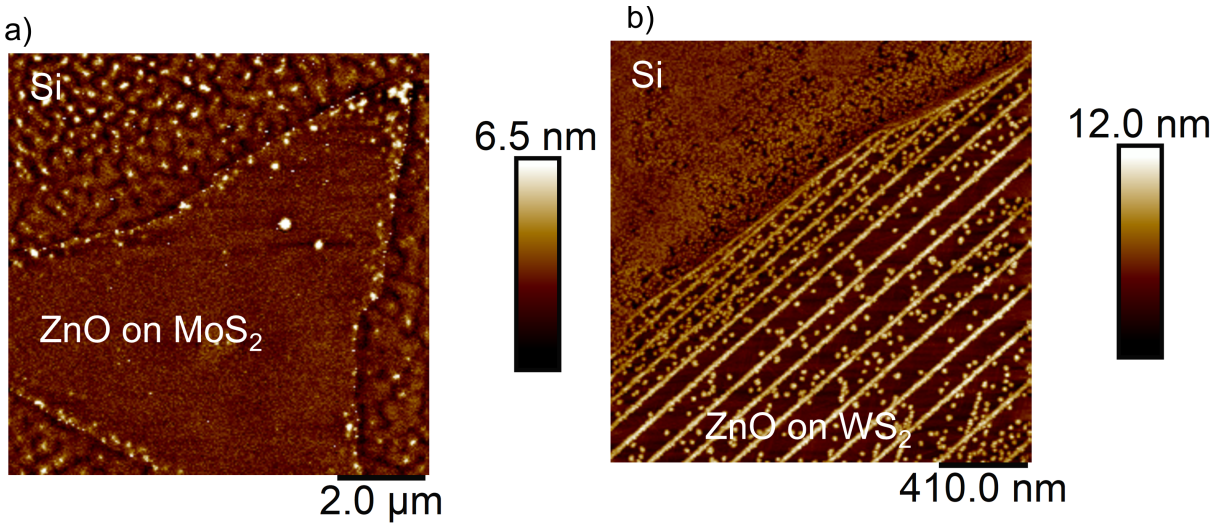


Figure 24. Preferential nucleation of ZnO on flake edges of (a) CVD-MoS_2 (5 AP-SCVD oscillations) and (b) CVD-WS_2 (25 AP-SCVD oscillations).

Notably, it is evident in Figures 21 and 25 that AP-SCVD yielded rapid nucleation of ZnO on what are expected to be passive 2D surfaces. This is supported by Table 1, which compares the ZnO nucleation behavior observed in this work to previous reports. I achieved comparatively faster nucleation without the requirement of any surface treatments. For example, in previous work by Walter et al., plasma-enhanced ALD (PEALD) of ZnO on MoS_2 reduced the ZnO nucleation period to ≤ 20 ALD cycles, whereas partial ZnO layer closure was observed after 25 AP-SCVD cycles on the CVD-WS_2 sample in Figure 21f.

Table 1. Nucleation of ZnO on MoS_2 and WS_2

ZnO deposition technique	2D material	Surface treatment	Process temperature (°C)	ALD cycles to initiate nucleation	Growth mode	[Ref]
Thermal ALD	MoS_2-exfoliated flake	No	125	200	Volmer-Weber (island) growth	[45]
PEALD	MoS_2-exfoliated flake	No	125	20	Layer-by-layer growth	[45]
Thermal ALD	MoS_2-exfoliated flake	UV-O_3	125	60	Layer-by-layer growth	[45]
ALD	CVD MoS_2	Perylene-3,4,9,10-tetracarboxylic acid (PTCA)	125	Not reported	Layer-by-layer growth	[96]
Magnetron Sputtering	Magnetron Sputtered - WS_2	No	100	NA	ZnO fills crevices, later forms film.	[97]
AP-SCVD	CVD MoS_2	No	100	<5	Island growth	This work
AP-SCVD	CVD WS_2	No	100	<5	Island growth	This work

The deposition rate was further increased by increasing the spacing between the reactor head and the substrate from ~110 µm to ~150 µm, keeping all the other parameters constant. This allowed for increased precursor crosstalk, meaning the precursors can mix on the substrate surface, allowing for higher deposition rate. Figure 26 shows ZnO deposited on CVD-MoS_2 and CVD-WS_2 with 5 AP-SCVD

oscillations using this larger reactor-substrate spacing. After only 5 oscillations, I could see significant nucleation with higher areal coverage as compared to Figures 21 and 25. While further optimization is warranted, the rapid nucleation facilitates layer closure at reasonably low film thicknesses. It is seen in the line scan of Figure 26a that the ZnO clusters had a height of approximately 5 nm when approaching layer closure. This rapid nucleation is attributed to the nature of the AP-SCVD process. There are various stages involved in thin film formation. This includes precursor delivery, which involves diffusion of precursor molecules to the substrate, physical adsorption of precursors on the substrate, followed by surface reaction and desorption of by-products. Since the reactor is held at atmospheric pressure, the effective diffusion coefficient of precursor molecules is very low. In many practical experimental conditions, Mameli et al. has shown that the precursor saturation dose is limited by the diffusion regime, which involves precursor delivery steps.[24] To offset this limitation, a high partial pressure of precursors is used in an AP-SALD/AP-SCVD system. Using a higher partial pressure shortens the time required for a precursor to saturate a substrate in two ways: it helps to increase the diffusion rate of the gaseous precursors and ensures a higher dose of precursor, thereby increasing the reaction rate. Operating the system in AP-SCVD mode, further increases the growth rate without compromising on film conformality. Improper precursor pressure and supply are considered to be a major roadblock to achieving conformal films in conventional CVD.[98] AP-SCVD addresses these issues by delivering the precursors gases in close proximity to the substrate, which ensures enough precursor delivery to form conformal films with high growth rates.

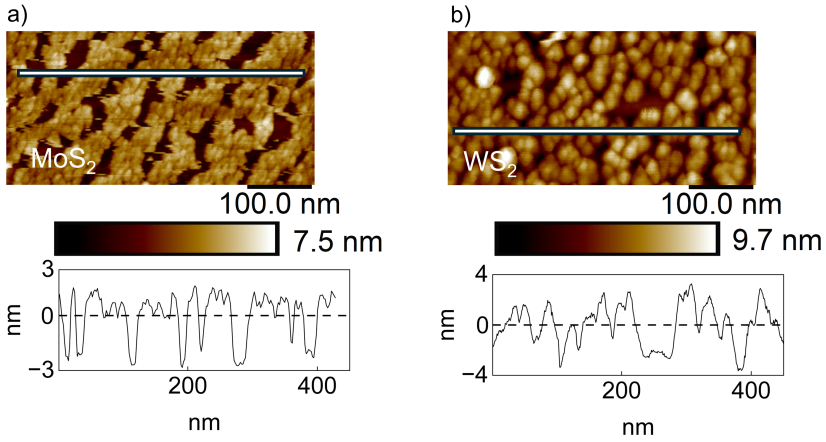


Figure 25. AFM images of ZnO deposited by 5 oscillations of AP-SCVD on (a) CVD-MoS_2 and (b) CVD-WS_2 at 100°C. A larger reactor-substrate spacing of 150 µm (compared to 110 µm in Figures 21 and 25) was used to further increase the deposition rate.

4.2.2 Structural and optical properties of CVD-grown monolayer MoS_2 and WS_2

To determine the impact of the AP-SCVD process on the TMDCs, Raman and photoluminescence spectroscopy measurements were conducted in three stages: (1) pristine conditions, (2) after exposure to simulate AP-SCVD deposition conditions, and (3) following the deposition of ZnO on the 2D materials. This allowed identification of whether any changes to the properties of the TMDCs are caused by the AP-SCVD processing conditions or the presence of the ZnO.

To simulate the deposition process without depositing any material, the 2D TMDCs were heated at 100°C in air for the time required to complete 100 oscillations (~10 minutes). Raman spectroscopy indicated no observable peak shift after subjecting the CVD-MoS_2 (Figure 27a) or CVD-WS_2 (Figure 27b) to AP-SCVD conditions. This suggests that no significant structural defects or strain were introduced into the 2D TMDC material and that the AP-SCVD process is relatively gentle and does not cause significant material degradation.

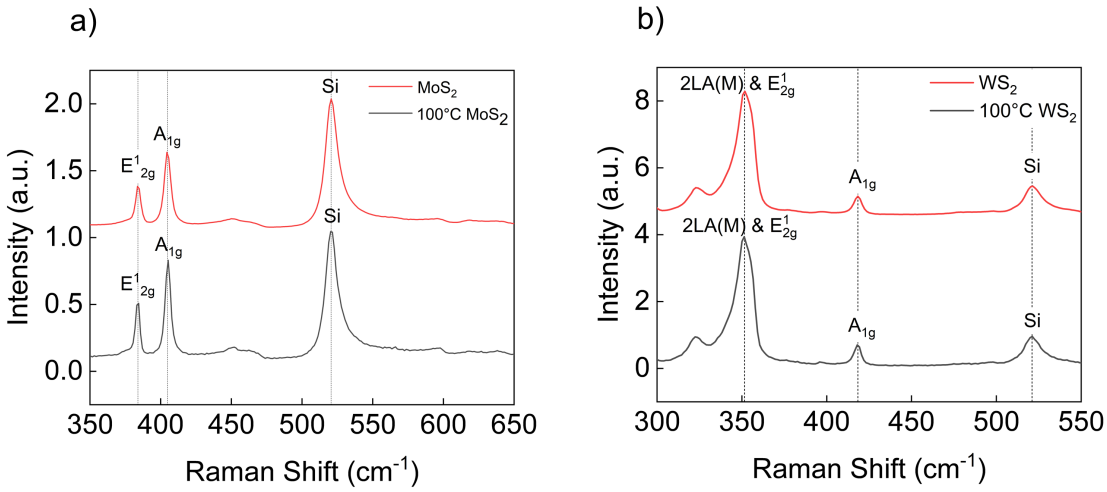


Figure 26. Raman spectra for (a) CVD-MoS_2 and (b) CVD-WS_2 before and after simulated AP-SCVD conditions.

The pristine CVD-MoS_2 and CVD-WS_2 showed strong PL emission at ~1.819 eV (Figure 28a) and ~1.962 eV (Figure 28d), respectively, consistent with previously reported values in literature for these materials.[37,40] After simulated AP-SCVD treatment, both TMDC spectra show a redshift with an increase in PL (Figure 28a and d). To quantify the relative changes, I compare the deconvoluted PL spectra. The deconvoluted spectra for the CVD-MoS_2 in its pristine form and after simulated AP-SCVD

processing are shown in Figures 28b and 28c. The PL spectrum for CVD-MoS_2 is known to consist mainly of A and B peaks. The A peak was deconvoluted into an A^- peak, which represents negatively charged trions, and an A^0 peak corresponding to neutral excitons.[37] The trion peak arises due to electron doping induced by the SiO_2 substrate.[99] The B peak represents the B excitons. Similarly, the CVD-WS_2 PL spectra were deconvoluted into an A^0 peak associated with neutral excitons and an A^- peak associated with trions, which are at a comparatively lower energy level (Figure 28e and f).[100] As the samples are heated in open atmosphere, O_2 and H_2O molecules from air are expected to be physically adsorbed on the CVD-TMDC surfaces. This should lead to depletion of electrons (p-type doping), generating neutral excitons (trion-to-neutral-exciton conversion), which radiatively recombine to give a sharp increase in PL.[40,101] As these adsorbed molecules, especially oxygen, act as p-type dopants, they are expected to slightly reduce the bandgap, resulting in the observed red shift for CVD-MoS_2[102,103] and CVD-WS_2.[100,104,105]

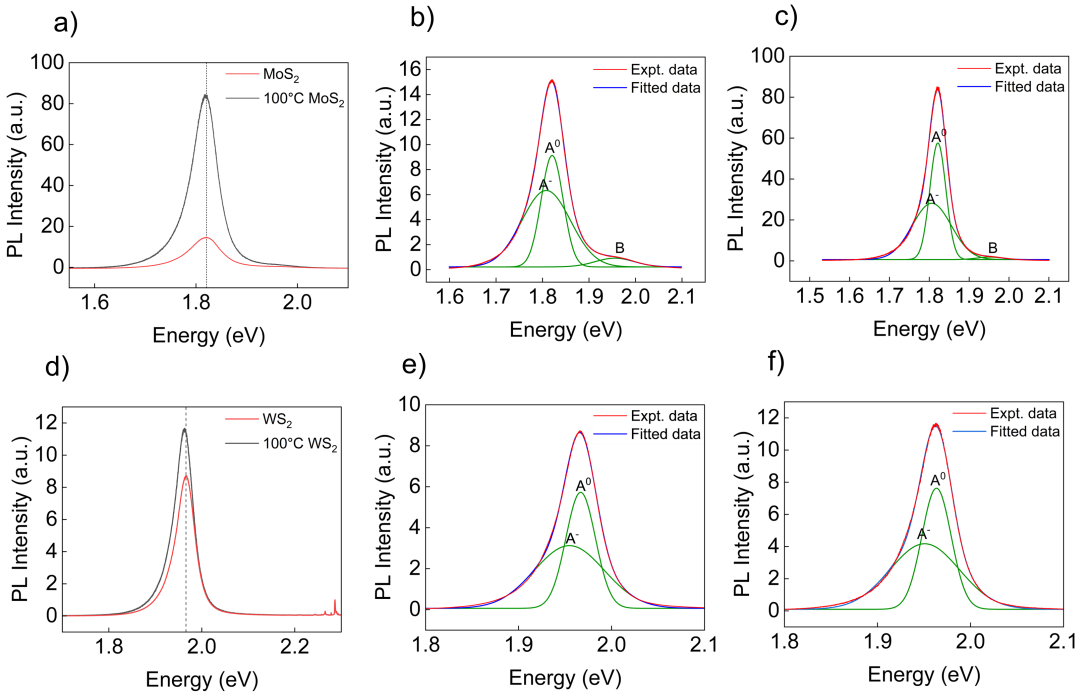


Figure 27. (a) PL spectra of CVD-MoS_2 (pristine vs. AP-SCVD simulated conditions). Deconvoluted spectra of (b) pristine CVD-MoS_2 and (c) CVD-MoS_2 after simulated AP-SCVD conditions. (d) PL spectra of CVD-WS_2 (pristine vs. AP-SCVD simulated conditions). Deconvoluted spectra of (e) pristine CVD-WS_2 and (f) CVD-WS_2 after simulated AP-SCVD conditions.

To quantify the trion-to-exciton conversion, I calculated the intensity ratios of neutral excitons to negatively charged trions in Table 2. Both the CVD-MoS_2 and CVD-WS_2 showed an increase in the ratio of excitons to trions after being subjected to AP-SCVD conditions, consistent with the enhanced PL intensity observed in Figure 28a and 28d.

Table 2. Intensity ratios of exciton (A^0) and trion (A^-) PL peaks for CVD-MoS_2 and CVD-WS_2 before and after simulated AP-SCVD treatment

	CVD-MoS_2	**CVD-WS_2**
Pristine **$I(A^0)/I(A^-)$**	8.91033 / 6.11186 = 1.457	5.6306 / 3.0598 = 1.840
AP-SCVD treated **$I(A^0)/I(A^-)$**	56.92736 / 27.50397 = 2.069	7.53065 / 4.07701 = 1.847

It was also observed that non-triangular CVD-MoS_2 flakes show a comparatively larger increase in PL than triangular flakes, after subjecting them to AP-SCVD conditions (Figure 29). This might be because of the presence of defects/imperfections that lead to depletion of excess electrons due to a higher probability of adsorbing O_2/ H_2O molecules.[101] Hence, I found that the AP-SCVD technique is not only a benign process but also helped in passivating the defects present in the 2D materials, suppressing non-radiative recombination that might occur at the defects.[40]

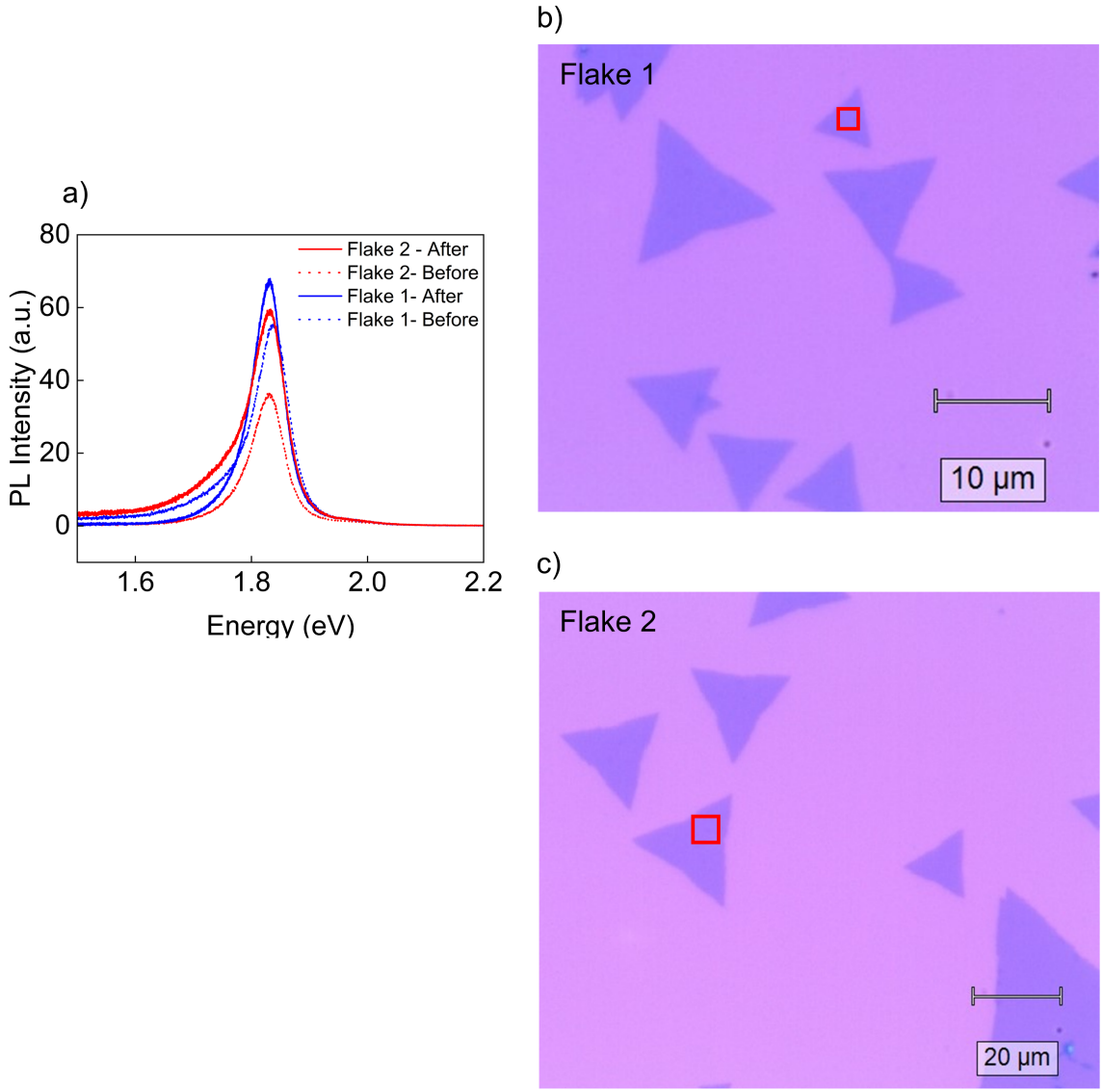


Figure 28. (a) PL spectra of differently shaped flakes before and after simulated AP-SCVD processing. Non-triangular CVD-MoS_2 flakes (e.g., "Flake 2" in c)) show a comparatively larger increase in PL than triangular flakes (e.g., "Flake 1" in b)).

I then investigated the effect of a ZnO surface layer on CVD-TMDCs. Figure 30 shows the Raman and PL spectroscopy of CVD-MoS_2 and CVD-WS_2 before and after deposition of a ZnO layer using 60 AP-SCVD oscillations and the original reactor spacing of ~110µm (i.e., surface coverage similar to that shown in Figures 21d and 21h). Raman spectra analysis of the MoS_2 – ZnO structure in Figure 30a

revealed a red shift and a slight broadening of the out-of-plane A_{1g} mode. This could be attributed to increased electron concentration after the deposition of ZnO, which is a n-type material. These changes in the Raman mode due to electron doping are consistent with literature.[40,59]

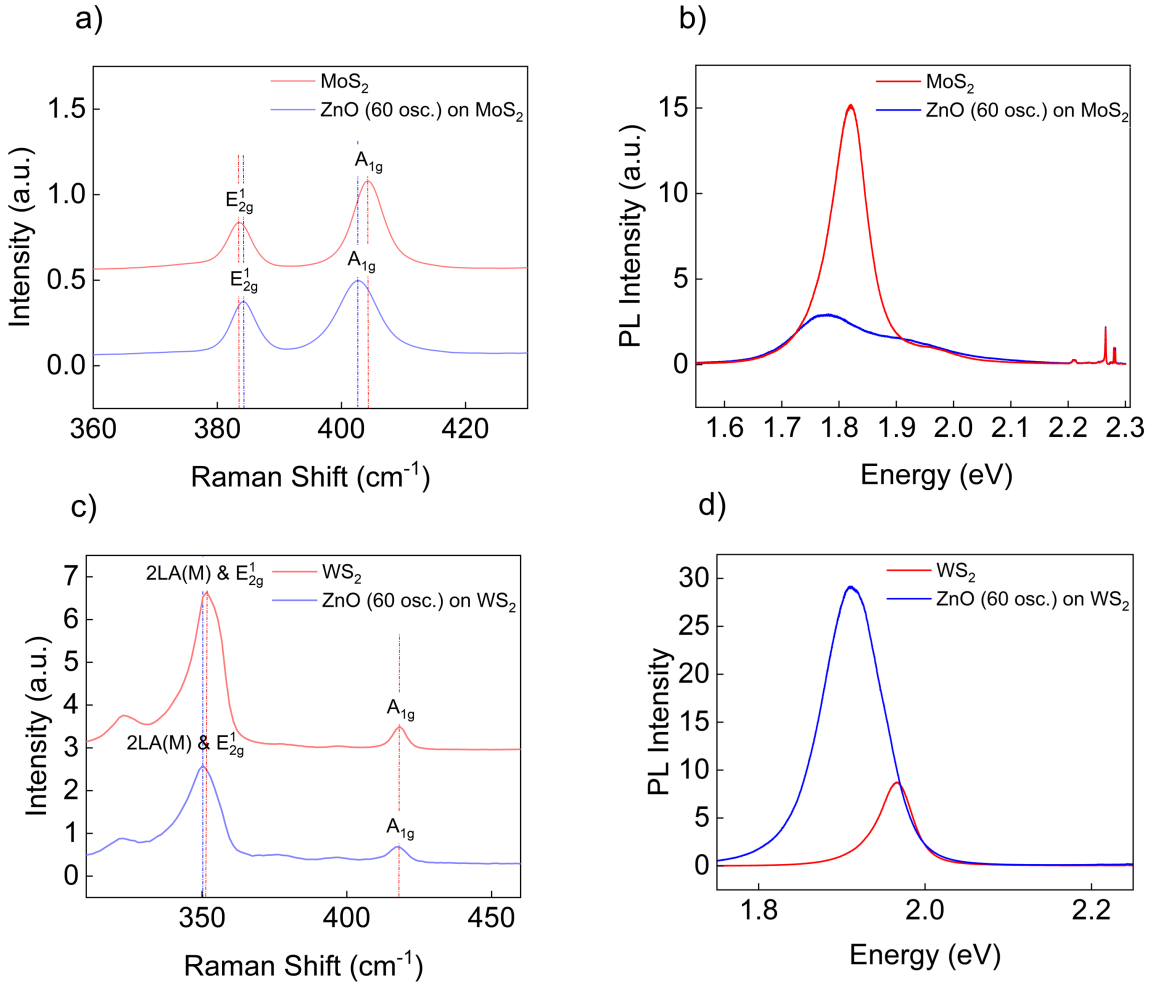


Figure 29. (a) Raman and (b) PL spectra of CVD-MoS_2 before and after ZnO deposition; (c) Raman and (d) PL spectra of CVD-WS_2 before and after ZnO deposition.

The in-plane E^1_{2g} mode in CVD-MoS_2 showed a blue shift after ZnO deposition, potentially due to a change in lateral strain. [40,59] E. Pollmann et al reported a transformation matrix to quantify the strain- and doping-dependent Raman shift in MoS_2 experimentally and by calculations, which is presented in Equations (1) and (2).[106]

$$T = \begin{pmatrix} -0.490\ \%/\mathrm{cm} & 0.073\ \%/\mathrm{cm} \\ 0.088 \times 10^{13}\mathrm{cm}^{-2}/\mathrm{cm}^{-1} & -0.464 \times 10^{13}\mathrm{cm}^{-2}/\mathrm{cm}^{-1} \end{pmatrix} \quad (1)$$

$$T\begin{pmatrix} \Delta E^1_{2g} \\ \Delta A_{1g} \end{pmatrix} = \begin{pmatrix} \Delta\ \mathrm{Strain} \\ \Delta\ \mathrm{Doping} \end{pmatrix} \quad (2)$$

Calculating the Raman shift from Figure 30a:

$$\Delta E^1_{2g} = \Delta E^1_{2g\,(\mathrm{ZnO\ coating})} - \Delta E^1_{2g\,(\mathrm{pristine})} \sim (384.33\text{-}383.02) = 1.31$$

$$\Delta A_{1g} = \Delta A_{1g(\mathrm{ZnO\ coating})} - \Delta A_{1g(\mathrm{pristine})} \sim (402.59 - 403.9) = -1.31$$

After solving the matrix using (1) and (2):

$$\begin{pmatrix} \Delta\ \mathrm{Strain} \\ \Delta\ \mathrm{Doping} \end{pmatrix} = \begin{pmatrix} -0.737\ \%/\mathrm{cm} \\ 0.723 \times 10^{13}\mathrm{cm}^{-2}/\mathrm{cm}^{-1} \end{pmatrix}$$

The positive Δ Doping indicates that the number of charge carriers in the MoS_2, namely electrons, have increased in number. A negative Δ Strain can be interpreted in two ways: the most straightforward explanation could be that the ZnO deposition led to a reduction in strain in tensile-strained CVD-MoS_2, or it could also mean that the material was initially compressively strained and that after depositing ZnO on top, the compressive strain increased. As-grown CVD-MoS_2 is reported to be under strain (e.g., compared to exfoliated CVD-MoS_2) and with ZnO coating the strain is decreasing, either reducing tension or increasing compression, depending on the initial strain state.[106] However, further experiments are warranted to investigate the strain relationship between the TMDCs and deposited oxide films. After the deposition of ZnO on CVD-MoS_2, I observed PL quenching along with a red shift and broadening of the PL emission (Figure 30b.). This can be explained by a possibility of charge transfer occurring from ZnO (n-type) to CVD-MoS_2, converting neutral excitons to trions, which lead to non-radiative recombination at the monolayer flake. [40,107] This is consistent with the Raman findings in Figure 30a, where broadening of the A_{1g} mode was attributed to electron doping of the MoS_2. [27,37] Possible PL absorption by the ZnO layer was considered; however, the observed enhancement in PL for the ZnO-WS_2 system confirms that the PL emission is not significantly absorbed by the ZnO layer.

For ZnO deposition on CVD-WS_2, the Raman spectra in Figure 30c show a red shift in the E^1_{2g} mode, which overlaps with the longitudinal acoustic phonon 2LA (M) mode. This could suggest the presence of tensile strain in the WS_2-ZnO system.[108] The A_{1g} mode, however, shows negligible change. Since this peak mainly describes the doping state of CVD-WS_2,[108] we can say that the doping effect is not very prominent at the PL excitation wavelength used. The PL spectra of the WS_2 and WS_2 - ZnO system are shown in Figure 30d. A red shift in the PL was again observed; however, in contrast to what was observed for CVD-MoS_2, a prominent increase in PL intensity was seen with the addition of ZnO on WS_2. In this system, there are several competing mechanisms at play, namely dielectric screening, doping, and strain effects. The ZnO deposition is expected to lead to charge transfer from ZnO to CVD-WS_2, creating a n-doped region at the interface, generating trions that might non-radiatively recombine to reduce the PL intensity. However, from the nucleation studies, we know that ZnO forms a complete layer on the WS_2 (Figure 21h). This complete layer of ZnO might cause dielectric screening, suppressing the trion formation and enhancing emission from neutral excitons,[60] which could explain the enhanced PL intensity. A similar effect has been reported for MoS_2 as well.[109–111] Both tensile strain, as indicated by the Raman shift in Fig 30c, and dielectric screening could contribute to the PL redshift observed in Fig 30d.[60,112,113] Therefore, the Raman and PL analysis of the WS_2 - ZnO system are consistent and suggest that the strain effect is more prominent than doping.

Therefore, the different photoexcited behavior observed here for the MoS_2-ZnO and WS_2-ZnO systems can be attributed to the competing effects of doping, strain, and dielectric screening. For the MoS_2-ZnO system, photoexcitation facilitates electron transfer from ZnO to MoS_2, resulting in n-type doping. The ZnO deposition also induces strain in the flake, introduced after the deposition of the material and not due to the conditions during the process, as confirmed from the Raman analysis. Nanoribbon are formed on the MoS_2 and these nanoribbons, which do not fully cover the MoS_2 flake, do not appear to result in a significant dielectric screening effect that impacts the PL. In the absence of strong dielectric screening, trions created by n-doping remain stable, leading to PL quenching. While depositing the ZnO at 100°C in air helps to passivate defects and enhance the PL, this is offset by the impacts of the strain and doping, resulting in a net decrease in PL with the addition of ZnO at 100°C. Also, the discontinuous MoS_2-ZnO interface formed due to incomplete nanoribbon ZnO coverage on the MoS_2, and intrinsic defects in the materials, may cause carriers to transfer at trapped states, further contributing to PL quenching.[89]

In contrast, ZnO almost completely covered the CVD-WS_2, and Raman analysis showed that the strain induced by the ZnO is more prominent than the doping effect. Upon photoexcitation, charges from ZnO might transfer to CVD-WS_2, creating a n-doped region, however this region also experiences dielectric screening due to the significant coverage of ZnO, thereby reducing trion formation and instead promoting the formation of neutral excitons, which radiatively recombine leading to an increase in PL. Therefore, in the case of CVD-WS_2, strain along with dielectric screening appear to play a major role in influencing its properties. Furthermore, the smooth interface between CVD-WS_2 and ZnO due to complete coverage might also aid in the reduction/passivation of trapped states, thus reducing non-radiative recombination.

To investigate the AP-SCVD temperature window for which these results are valid, ZnO was deposited on CVD-WS_2 at temperatures ranging from 50°C to 250°C. Fig 31 shows the PL spectra for each temperature, including measurements for pristine samples, samples annealed in air to simulate the AP-SCVD processing conditions, and samples after the deposition of ZnO at that temperature using 300 AP-SCVD oscillations.

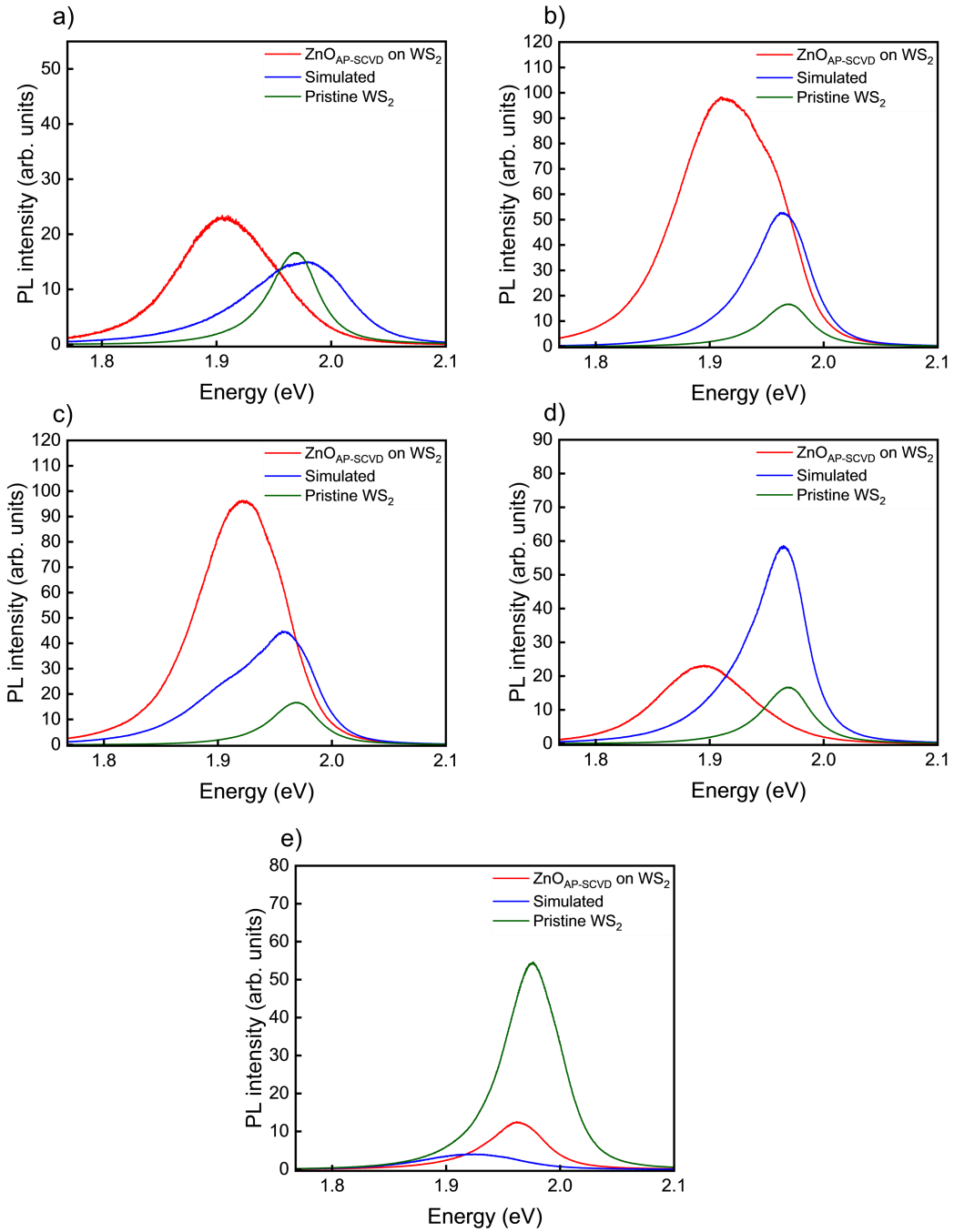


Figure 30. PL spectra for pristine CVD-WS_2, CVD-WS_2 annealed in air, and CVD-WS_2 after the deposition of ZnO using 300 AP-SCVD oscillations, at annealing and deposition temperatures of (a) 50°C, (b) 100°C, (c) 150°C, (d) 200°C and (e) 250°C

The change in PL intensity resulting from the simulated AP-SCVD conditions and ZnO depositions are summarized in Figure 32 as a function of temperature. The increase in PL intensity due to annealing in air was seen to increase gradually with annealing temperature (blue trendline), consistent with a gradual increase in the adsorption of O_2 and H_2O molecules and p-type doping. At 200°C, the PL for simulated samples was seen to slightly decrease, indicating the initiation of degradation of the 2D layer, which is further supported by the sudden drop in PL at 250°C. The PL of the ZnO-coated samples is observed to be enhanced, as compared to pristine samples, for deposition temperatures ranging from 50°C to 200°C. The 300 AP-SCVD oscillations are expected to result in complete coverage of the flake with ZnO, such that the dielectric screening effect is still expected to be present. However, the increase in PL intensity for the ZnO – WS_2 samples initially increased with temperature up until 100°C and then was reduced at higher ZnO deposition temperatures. This trend may be attributable to different competing effects such as varying crystallinity of the ZnO film,[114] increased carrier concentration that affects doping[115], reduced thickness of the ZnO layer due to thermal desorption of precursor at higher temperatures [89,116,117] resulting in a decrease in the dielectric constant[118], and the induced strain in the material. Thus, while further study of the deposition-temperature-dependent behavior of the TMDC - ZnO heterostructures is warranted, it is clear that the behavior observed here occurs across a range of typical AP-SCVD deposition temperatures.

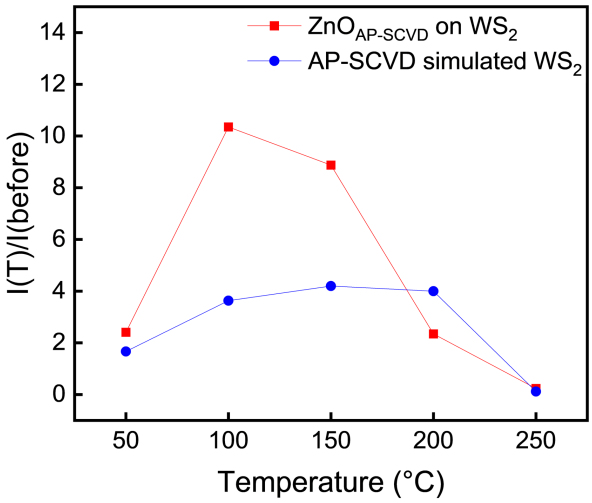


Figure 31. Change in PL intensity of CVD-WS2 after annealing or ZnO deposition at different temperatures.

Chapter 5
Conclusions and Future Work

5.1 Conclusions

The first goal of this thesis was to develop an AP-SALD process for the deposition of silicon oxide. Initial attempts with peroxide-30 showed limited reactivity between the precursors, which yielded Si-based nano crystallites because of precursor condensation, and it was concluded that the oxidation of the Si-H bond was the limiting factor. As a result, a more potent oxidizing agent, ozone, was selected. I used ozone to create ALD-quality SiO_x films on silicon and ITO/glass substrates at a temperature as low as 70°C and at high growth rates of 0.5 Å/sec. AFM and XPS measurements confirmed that the films were amorphous with the SiO_x film covering the entire substrate. The microstructure was temperature-dependent; changing from an amorphous film to nano crystallites as the deposition temperature was reduced, which was attributed to precursor condensation. I believe that the open-air, plasma-free AP-SALD technique described herein will pave the way for future improvements in SiO_x depositions at lower temperatures, potentially broadening their applications in a variety of areas.

The second goal was to investigate the nucleation and growth of ZnO on 2D TMDCs. This was demonstrated successfully and AP-SCVD exhibited a very high potential for the development of heterostructures with 2D TMDCs. It was observed that AP-SCVD leads to comparatively rapid nucleation of a metal oxide on top of 2D materials without any need for surface treatment. This was attributed to the nature of the process itself. High precursor dosage is usually used when compared to conventional ALD to compensate for the low effective diffusion coefficient of the precursor molecules, as the system operates in open air. This leads to a low saturation time and high possibility of adsorption of precursors on the 2D surface, leading to rapid nucleation, growth, and layer closure. Also, from PL and Raman spectroscopy, it was confirmed that the AP-SCVD process is "soft" when compared to other processes for depositing oxides on 2D TMDCs, such as spin coating, thermal ALD, and plasma-enhanced ALD,[108,119–121] as it doesn't affect the structure and properties of the 2D materials when operated in the right temperature window. In fact, the AP-SCVD process, which uses modest deposition temperatures (~100°C) in air, was found lead to passivation of defects by O_2 and/or moisture adsorption. Deposition of ZnO by AP-SCVD was found to quench the PL of CVD-MoS_2, whereas it

enhanced the PL of CVD-WS_2. This was attributed to the competing effects of strain, doping, and dielectric screening. For the MoS_2-ZnO, doping and strain dominate, whereas for the WS_2-ZnO, strain and dielectric screening have a larger impact on the properties of the 2D TMDC. Greater ZnO surface coverage was observed on the WS_2, which would contribute to the greater dielectric screening.

5.2 Future work

Suggestions for the development of silicon oxide films:

- Investigate the reaction mechanism of DIPAS with advanced techniques such as in-situ FTIR to understand the chemistry and kinetics of the ALD reactions in more detail.
- Investigate the use of additional precursors such as Trimethylalumnium (TMA) alongside DIPAS to deposit composite oxides like $Al_xSi_yO_z$.[122]
- Understand the effect of other uncontrollable parameters such as humidity on the reaction mechanism.
- The use of ozone is undesirable since it is known to have many hazards and therefore, future study can focus and explore new precursors for the synthesis of silicon oxide films at low temperature or even room temperature without the use of ozone.

Suggestions for the nucleation of metal oxides on 2D materials:

- Test the performance of ZnO/TMDC heterostructures in devices and analyze the impact of the interface formed by a discontinuous nucleation layer.
- Analyze the effect of depositing continuous-thick layer of metal oxides on the TMDCs
- Expand the study with different metal oxides such as Al_2O_3, SiO_2, HfO_2 with other 2D materials such as graphene, $MoSe_2$, WSe_2 etc.

References

(1) Wu, H. Y.; Liu, T. X.; Hsu, C. H.; Cho, Y. S.; Xu, Z. J.; Liao, S. C.; Zeng, B. H.; Jiang, Y. L.; Lien, S. Y. Thin-Film Coated Plastic Wrap for Food Packaging. *Materials* **2017**, *10* (7). https://doi.org/10.3390/ma10070821.

(2) Dias, V.; Maciel, H.; Fraga, M.; Lobo, A. O.; Pessoa, R.; Marciano, F. R. Atomic Layer Deposited TiO 2 and Al 2 O 3 Thin Films as Coatings for Aluminum Food Packaging Application. *Materials* **2019**, *12* (4). https://doi.org/10.3390/ma12040682.

(3) Lee, D. T.; Zhao, J.; Oldham, C. J.; Peterson, G. W.; Parsons, G. N. UiO-66-NH2 Metal-Organic Framework (MOF) Nucleation on TiO2, ZnO, and Al2O3 Atomic Layer Deposition-Treated Polymer Fibers: Role of Metal Oxide on MOF Growth and Catalytic Hydrolysis of Chemical Warfare Agent Simulants. *ACS Appl Mater Interfaces* **2017**, *9* (51). https://doi.org/10.1021/acsami.7b15397.

(4) Brozena, A. H.; Oldham, C. J.; Parsons, G. N. Atomic Layer Deposition on Polymer Fibers and Fabrics for Multifunctional and Electronic Textiles. *Journal of Vacuum Science & Technology A: Vacuum, Surfaces, and Films* **2016**, *34* (1). https://doi.org/10.1116/1.4938104.

(5) Wang, X.; Yushin, G. Chemical Vapor Deposition and Atomic Layer Deposition for Advanced Lithium Ion Batteries and Supercapacitors. *Energy and Environmental Science*. 2015. https://doi.org/10.1039/c5ee01254f.

(6) Elam, J. W.; Dasgupta, N. P.; Prinz, F. B. ALD for Clean Energy Conversion, Utilization, and Storage. *MRS Bull* **2011**, *36* (11). https://doi.org/10.1557/mrs.2011.265.

(7) Zhao, Y.; Zhang, L.; Liu, J.; Adair, K.; Zhao, F.; Sun, Y.; Wu, T.; Bi, X.; Amine, K.; Lu, J.; Sun, X. Atomic/Molecular Layer Deposition for Energy Storage and Conversion. *Chemical Society Reviews*. 2021. https://doi.org/10.1039/d0cs00156b.

(8) Leskelä, M.; Mattinen, M.; Ritala, M. Review Article: Atomic Layer Deposition of Optoelectronic Materials. *Journal of Vacuum Science & Technology B, Nanotechnology and Microelectronics: Materials, Processing, Measurement, and Phenomena* **2019**, *37* (3). https://doi.org/10.1116/1.5083692.

(9) Hirvikorpi, T.; Laine, R.; Vähä-Nissi, M.; Kilpi, V.; Salo, E.; Li, W. M.; Lindfors, S.; Vartiainen, J.; Kenttä, E.; Nikkola, J.; Harlin, A.; Kostamo, J. Barrier Properties of Plastic Films Coated with an Al2O 3 Layer by Roll-to-Toll Atomic Layer Deposition. *Thin Solid Films* **2014**, *550*. https://doi.org/10.1016/j.tsf.2013.10.148.

(10) Puurunen, R. L. A Short History of Atomic Layer Deposition: Tuomo Suntola's Atomic Layer Epitaxy. *Chemical Vapor Deposition*. 2014. https://doi.org/10.1002/cvde.201402012.

(11) Johnson, R. W.; Hultqvist, A.; Bent, S. F. A Brief Review of Atomic Layer Deposition: From Fundamentals to Applications. *Materials Today*. 2014. https://doi.org/10.1016/j.mattod.2014.04.026.

(12) Chen, M.; Nijboer, M. P.; Kovalgin, A. Y.; Nijmeijer, A.; Roozeboom, F.; Luiten-Olieman, M. W. J. Atmospheric-Pressure Atomic Layer Deposition: Recent Applications and New Emerging Applications in High-Porosity/3D Materials. *Dalton Transactions*. 2023. https://doi.org/10.1039/d3dt01204b.

(13) van de Poll, M. L.; Jain, H.; Hilfiker, J. N.; Utriainen, M.; Poodt, P.; Kessels, W. M. M.; Macco, B. Excellent Conformality of Atmospheric-Pressure Plasma-Enhanced Spatial Atomic Layer Deposition with Subsecond Plasma Exposure Times. *Appl Phys Lett* **2023**, *123* (18). https://doi.org/10.1063/5.0168768.

(14) Li, R.; Jiang, X.; Zhou, C.; Topsakal, M.; Nykypanchuk, D.; Attenkofer, K.; Stacchiola, D. J.; Hybertsen, M. S.; Stavitski, E.; Qu, X.; Lu, D.; Liu, M. *Deciphering Phase Evolution in Complex Metal Oxide Thin Films via High-Throughput Materials Synthesis and Characterization*.

(15) Girtan, M.; Negulescu, B. A Review on Oxide/Metal/Oxide Thin Films on Flexible Substrates as Electrodes for Organic and Perovskite Solar Cells. *Optical Materials: X* **2022**, *13*. https://doi.org/10.1016/j.omx.2021.100122.

(16) Williams, A. T.; Rangel-Buitrago, N. The Past, Present, and Future of Plastic Pollution. *Mar Pollut Bull* **2022**, *176*. https://doi.org/10.1016/j.marpolbul.2022.113429.

(17) *UN: Department of Economic and Social Affairs Sustainable Development*.

(18) Ortiz, A. A.; Sucozhañay, D.; Vanegas, P.; Martínez-Moscoso, A. A Regional Response to a Global Problem: Single Use Plastics Regulation in the Countries of the Pacific Alliance. *Sustainability (Switzerland)* **2020**, *12* (19). https://doi.org/10.3390/su12198093.

(19) Zhao, Y.; Huang, C.; Huang, X.; Huang, H.; Zhao, H.; Wang, S.; Liu, S. Effectiveness of PECVD Deposited Nano-Silicon Oxide Protective Layer for Polylactic Acid Film: Barrier and Surface Properties. *Food Packag Shelf Life* **2020**, *25*. https://doi.org/10.1016/j.fpsl.2020.100513.

(20) *SiO 2 Chemical Vapor Deposition at Room Temperature Using SiCl 4 and H 2 O with an NH 3 Catalyst*; 2000.

(21) Lee, Y. S.; Lee, S. H.; Kwon, J. D.; Ahn, J. H.; Park, J. S. Silicon Oxide Film Deposited at Room Temperatures Using High-Working-Pressure Plasma-Enhanced Chemical Vapor Deposition: Effect of O2 Flow Rate. *Ceram Int* **2017**, *43* (13), 10628–10631. https://doi.org/10.1016/j.ceramint.2017.05.095.

(22) Lee, Y.-S.; Han, J.-H.; Park, J.-S.; Park, J. Low Temperature SiOx Thin Film Deposited by Plasma Enhanced Atomic Layer Deposition for Thin Film Encapsulation Applications. *Journal of Vacuum Science & Technology A: Vacuum, Surfaces, and Films* **2017**, *35* (4). https://doi.org/10.1116/1.4985140.

(23) 1. Musselman, K. P.; Uzoma, C. F.; Miller, M. S. Nanomanufacturing: High-Throughput, Cost-Effective Deposition of Atomic Scale Thin Films via Atmospheric Pressure Spatial Atomic Layer Deposition. *Chemistry of Materials* **2016**, 8443–8452.

(24) Poodt, P.; Mameli, A.; Schulpen, J.; Kessels, W. M. M. (Erwin); Roozeboom, F. Effect of Reactor Pressure on the Conformal Coating inside Porous Substrates by Atomic Layer Deposition. *Journal of Vacuum Science & Technology A: Vacuum, Surfaces, and Films* **2017**, *35* (2). https://doi.org/10.1116/1.4973350.

(25) Mione, M. A.; Vandalon, V.; Mameli, A.; Kessels, W. M. M.; Roozeboom, F. Atmospheric-Pressure Plasma-Enhanced Spatial ALD of SiO2Studied by Gas-Phase Infrared and Optical Emission Spectroscopy. *Journal of Physical Chemistry C* **2021**, *125* (45), 24945–24957. https://doi.org/10.1021/acs.jpcc.1c07980.

(26) Nguyen, V. H.; Sekkat, A.; Masse De La Huerta, C. A.; Zoubian, F.; Crivello, C.; Rubio-Zuazo, J.; Rubio-Zuazo, J.; Jaffal, M.; Bonvalot, M.; Vallée, C.; Aubry, O.; Rabat, H.; Hong, D.; Muñoz-Rojas, D. Atmospheric Plasma-Enhanced Spatial Chemical Vapor Deposition of SiO2Using Trivinylmethoxysilane and Oxygen Plasma. *Chemistry of Materials* **2020**, *32* (12), 5153–5161. https://doi.org/10.1021/acs.chemmater.0c01148.

(27) Novoselov, K. S.; Mishchenko, A.; Carvalho, A.; Castro Neto, A. H. 2D Materials and van Der Waals Heterostructures. *Science*. American Association for the Advancement of Science July 29, 2016. https://doi.org/10.1126/science.aac9439.

(28) Lin, J.; Zhou, W. Defect in 2D Materials beyond Graphene. In *Defects in Advanced Electronic Materials and Novel Low Dimensional Structures*; Elsevier, 2018; pp 161–187. https://doi.org/10.1016/B978-0-08-102053-1.00006-5.

(29) Li, H.; Shi, Y.; Chiu, M. H.; Li, L. J. Emerging Energy Applications of Two-Dimensional Layered Transition Metal Dichalcogenides. *Nano Energy*. Elsevier Ltd November 1, 2015, pp 293–305. https://doi.org/10.1016/j.nanoen.2015.10.023.

(30) Li, W.; Zhou, J.; Cai, S.; Yu, Z.; Zhang, J.; Fang, N.; Li, T.; Wu, Y.; Chen, T.; Xie, X.; Ma, H.; Yan, K.; Dai, N.; Wu, X.; Zhao, H.; Wang, Z.; He, D.; Pan, L.; Shi, Y.; Wang, P.; Chen, W.; Nagashio, K.; Duan, X.; Wang, X. Uniform and Ultrathin High-κ Gate Dielectrics for Two-Dimensional Electronic Devices. *Nat Electron* **2019**, *2* (12), 563–571. https://doi.org/10.1038/s41928-019-0334-y.

(31) He, X.; Li, H.; Zhu, Z.; Dai, Z.; Yang, Y.; Yang, P.; Zhang, Q.; Li, P.; Schwingenschlogl, U.; Zhang, X. Strain Engineering in Monolayer WS2, MoS2, and the WS2/MoS2 Heterostructure. *Appl Phys Lett* **2016**, *109* (17). https://doi.org/10.1063/1.4966218.

(32) Zhao, Y.; Ouyang, G. Thickness-Dependent Photoelectric Properties of MoS2/Si Heterostructure Solar Cells. *Sci Rep* **2019**, *9* (1). https://doi.org/10.1038/s41598-019-53936-2.

(33) Wakabayashi, N.; Smith, H. G.; Nicklow, R. M. Lattice Dynamics of Hexagonal MoS2 Studied by Neutron Scattering. *Phys Rev B* **1975**, *12* (2). https://doi.org/10.1103/PhysRevB.12.659.

(34) Lan, C.; Li, C.; Ho, J. C.; Liu, Y. 2D WS2: From Vapor Phase Synthesis to Device Applications. *Advanced Electronic Materials*. 2021. https://doi.org/10.1002/aelm.202000688.

(35) Schutte, W. J.; De Boer, J. L.; Jellinek, F. Crystal Structures of Tungsten Disulfide and Diselenide. *J Solid State Chem* **1987**, *70* (2). https://doi.org/10.1016/0022-4596(87)90057-0.

(36) Yehia, H. M.; Ali, A. I.; Abd-Elhameed, E. Effect of Exfoliated MoS2 on the Microstructure, Hardness, and Tribological Properties of Copper Matrix Nanocomposite Fabricated via the Hot Pressing Method. *Transactions of the Indian Institute of Metals* **2023**, *76* (1). https://doi.org/10.1007/s12666-022-02740-0.

(37) Kim, H. J.; Yun, Y. J.; Yi, S. N.; Chang, S. K.; Ha, D. H. Changes in the Photoluminescence of Monolayer and Bilayer Molybdenum Disulfide during Laser Irradiation. *ACS Omega* **2020**, *5* (14), 7903–7909. https://doi.org/10.1021/acsomega.9b04202.

(38) Ding, Y.; Wang, Y.; Ni, J.; Shi, L.; Shi, S.; Tang, W. First Principles Study of Structural, Vibrational and Electronic Properties of Graphene-like MX2 (M=Mo, Nb, W, Ta; X=S, Se, Te) Monolayers. *Physica B Condens Matter* **2011**, *406* (11). https://doi.org/10.1016/j.physb.2011.03.044.

(39) Lebègue, S.; Eriksson, O. Electronic Structure of Two-Dimensional Crystals from Ab Initio Theory. *Phys Rev B Condens Matter Mater Phys* **2009**, *79* (11). https://doi.org/10.1103/PhysRevB.79.115409.

(40) Kim, S. Y.; Yang, H. I.; Choi, W. Photoluminescence Quenching in Monolayer Transition Metal Dichalcogenides by Al2O3 Encapsulation. *Appl Phys Lett* **2018**, *113* (13). https://doi.org/10.1063/1.5048052.

(41) Gutiérrez, H. R.; Perea-López, N.; Elías, A. L.; Berkdemir, A.; Wang, B.; Lv, R.; López-Urías, F.; Crespi, V. H.; Terrones, H.; Terrones, M. Extraordinary Room-Temperature Photoluminescence in Triangular WS 2 Monolayers. *Nano Lett* **2013**, *13* (8). https://doi.org/10.1021/nl3026357.

(42) Li, N.; Wei, Z.; Zhao, J.; Wang, Q.; Shen, C.; Wang, S.; Tang, J.; Yang, R.; Shi, D.; Zhang, G. Atomic Layer Deposition of Al2O3 Directly on 2D Materials for High-Performance Electronics. *Adv Mater Interfaces* **2019**, *6* (10). https://doi.org/10.1002/admi.201802055.

(43) Oh, I. K.; Tanskanen, J.; Jung, H.; Kim, K.; Lee, M. J.; Lee, Z.; Lee, S. K.; Ahn, J. H.; Lee, C. W.; Kim, K.; Kim, H.; Lee, H. B. R. Nucleation and Growth of the HfO2 Dielectric Layer for

Graphene-Based Devices. *Chemistry of Materials* **2015**, *27* (17), 5868–5877. https://doi.org/10.1021/acs.chemmater.5b01226.

(44) Kümmell, T.; Andrzejewski, D.; Beckmann, Y.; Abdelbaky, M.; Yeow, T.; Grundmann, A.; Heuken, M.; Kalisch, H.; Vescan, A.; Musselman, K.; Bacher, G. WS2 Monolayer Based Light Emitting Devices Fabricated by Scalable Deposition Techniques; SPIE-Intl Soc Optical Eng, 2020; p 24. https://doi.org/10.1117/12.2544926.

(45) Walter, T. N.; Lee, S.; Zhang, X.; Chubarov, M.; Redwing, J. M.; Jackson, T. N.; Mohney, S. E. Atomic Layer Deposition of ZnO on MoS 2 and WSe 2. *Appl Surf Sci* **2019**, *480*, 43–51. https://doi.org/10.1016/j.apsusc.2019.02.182.

(46) Shin, W. C.; Bong, J. H.; Choi, S. Y.; Cho, B. J. Functionalized Graphene as an Ultrathin Seed Layer for the Atomic Layer Deposition of Conformal High- k Dielectrics on Graphene. *ACS Appl Mater Interfaces* **2013**, *5* (22), 11515–11519. https://doi.org/10.1021/am4039807.

(47) Xiao, M.; Qiu, C.; Zhang, Z.; Peng, L. M. Atomic-Layer-Deposition Growth of an Ultrathin HfO2 Film on Graphene. *ACS Appl Mater Interfaces* **2017**, *9* (39), 34050–34056. https://doi.org/10.1021/acsami.7b09408.

(48) Yeow, T. W.-K.; Mistry, K.; Shahin, A.; Yavuz, M.; Musselman, K. P. Atmospheric-Pressure Spatial Chemical Vapor Deposition of Tungsten Oxide. *Journal of Vacuum Science & Technology A: Vacuum, Surfaces, and Films* **2020**, *38* (5). https://doi.org/10.1116/6.0000347.

(49) Asgarimoghaddam, H.; Chen, Q.; Ye, F.; Shahin, A.; Song, B.; Musselman, K. P. Effect of Different Oxygen Precursors on Alumina Deposited Using a Spatial Atomic Layer Deposition System for Thin-Film Encapsulation of Perovskite Solar Cells. *Nanotechnology* **2024**, *35* (9). https://doi.org/10.1088/1361-6528/ad1059.

(50) Binnig, G.; Quate, C. F.; Gerber, C. Atomic Force Microscope. *Phys Rev Lett* **1986**, *56* (9). https://doi.org/10.1103/PhysRevLett.56.930.

(51) *AFM*.

(52) *https://www.jawoollam.com/resources*.

(53) *Spectroscopic Ellipsometry: Basic Principles*; 2022.

(54) Stevie, F. A.; Donley, C. L. Introduction to X-Ray Photoelectron Spectroscopy. *Journal of Vacuum Science & Technology A: Vacuum, Surfaces, and Films* **2020**, *38* (6). https://doi.org/10.1116/6.0000412.

(55) Leng, Y. *Materials Characterization: Introduction to Microscopic and Spectroscopic Methods: Second Edition*; 2013. https://doi.org/10.1002/9783527670772.

(56) Hodoroaba, V. D. Energy-Dispersive X-Ray Spectroscopy (EDS). In *Characterization of Nanoparticles: Measurement Processes for Nanoparticles*; 2019. https://doi.org/10.1016/B978-0-12-814182-3.00021-3.

(57) Bumbrah, G. S.; Sharma, R. M. Raman Spectroscopy – Basic Principle, Instrumentation and Selected Applications for the Characterization of Drugs of Abuse. *Egyptian Journal of Forensic Sciences*. 2016. https://doi.org/10.1016/j.ejfs.2015.06.001.

(58) Berkdemir, A.; Gutiérrez, H. R.; Botello-Méndez, A. R.; Perea-López, N.; Elías, A. L.; Chia, C. I.; Wang, B.; Crespi, V. H.; López-Urías, F.; Charlier, J. C.; Terrones, H.; Terrones, M. Identification of Individual and Few Layers of WS2 Using Raman Spectroscopy. *Sci Rep* **2013**, *3*. https://doi.org/10.1038/srep01755.

(59) Velický, M.; Rodriguez, A.; Bouša, M.; Krayev, A. V.; Vondráček, M.; Honolka, J.; Ahmadi, M.; Donnelly, G. E.; Huang, F.; Abrunã, H. D.; Novoselov, K. S.; Frank, O. Strain and Charge Doping Fingerprints of the Strong Interaction between Monolayer MoS2and Gold. *Journal of Physical Chemistry Letters* **2020**, *11* (15), 6112–6118. https://doi.org/10.1021/acs.jpclett.0c01287.

(60) Tugchin, B. N.; Doolaard, N.; Barreda, A. I.; Zhang, Z.; Romashkina, A.; Fasold, S.; Staude, I.; Eilenberger, F.; Pertsch, T. Photoluminescence Enhancement of Monolayer WS2 by N-Doping with an Optically Excited Gold Disk. *Nano Lett* **2023**, *23* (23), 10848–10855. https://doi.org/10.1021/acs.nanolett.3c03053.

(61) Kim, D. H.; Lee, H. J.; Jeong, H.; Shong, B.; Kim, W. H.; Park, T. J. Thermal Atomic Layer Deposition of Device-Quality SiO2 Thin Films under 100 °c Using an AminodisilanePrecursor. *Chemistry of Materials* **2019**, *31* (15), 5502–5508. https://doi.org/10.1021/acs.chemmater.9b01107.

(62) Sajjad, M. Recent Advances in SiO2 Based Composite Electrodes for Supercapacitor Applications. *J Inorg Organomet Polym Mater* **2021**, *31* (8), 3221–3239. https://doi.org/10.1007/s10904-021-01899-1.

(63) Lee, Y.; Seo, S.; Oh, I. K.; Lee, S.; Kim, H. Effects of O2 Plasma Treatment on Moisture Barrier Properties of SiO2 Grown by Plasma-Enhanced Atomic Layer Deposition. *Ceram Int* **2019**, *45* (14), 17662–17668. https://doi.org/10.1016/j.ceramint.2019.05.332.

(64) Han, S. M.; Aydil, E. S. Study of Surface Reactions during Plasma Enhanced Chemical Vapor Deposition of SiO2 from SiH4, O2, and Ar Plasma. *Journal of Vacuum Science & Technology A: Vacuum, Surfaces, and Films* **1996**, *14* (4), 2062–2070. https://doi.org/10.1116/1.580082.

(65) *SiO 2 Chemical Vapor Deposition at Room Temperature Using SiCl 4 and H 2 O with an NH 3 Catalyst*; 2000.

(66) Lee, J. H.; Kim, U. J.; Han, C. H.; Rha, S. K.; Lee, W. J.; Park, C. O. Investigation of Silicon Oxide Thin Films Prepared by Atomic Layer Deposition Using SiH2Cl2 and O3 as the Precursors. *Japanese Journal of Applied Physics, Part 2: Letters* **2004**, *43* (3 A). https://doi.org/10.1143/jjap.43.l328.

(67) Lee, S. W.; Park, K.; Han, B.; Son, S. H.; Rha, S. K.; Park, C. O.; Lee, W. J. Atomic Layer Deposition of Silicon Oxide Thin Films by Alternating Exposures to Si2Cl6and O3. *Electrochemical and Solid-State Letters* **2008**, *11* (7). https://doi.org/10.1149/1.2908201.

(68) Chaudhary, S.; Head, A. R.; Sánchez-De-Armas, R.; Tissot, H.; Olivieri, G.; Bournel, F.; Montelius, L.; Ye, L.; Rochet, F.; Gallet, J. J.; Brena, B.; Schnadt, J. Real-Time Study of CVD Growth of Silicon Oxide on Rutile TiO2(110) Using Tetraethyl Orthosilicate. *Journal of Physical Chemistry C* **2015**, *119* (33), 19149–19161. https://doi.org/10.1021/acs.jpcc.5b04985.

(69) Kim, D. H.; Lee, H. J.; Jeong, H.; Shong, B.; Kim, W. H.; Park, T. J. Thermal Atomic Layer Deposition of Device-Quality SiO2 Thin Films under 100 °c Using an Aminodisilane Precursor. *Chemistry of Materials* **2019**, *31* (15), 5502–5508. https://doi.org/10.1021/acs.chemmater.9b01107.

(70) Kamiyama, S.; Miura, T.; Nara, Y. Comparison between SiO2 Films Deposited by Atomic Layer Deposition with SiH2[N(CH3)2]2 and SiH[N(CH3)2]3 Precursors. *Thin Solid Films* **2006**, *515* (4), 1517–1521. https://doi.org/10.1016/j.tsf.2006.04.033.

(71) *DIPAS [Di-isopropylamino Silane]*. https://www.upchem.co.kr/m/eng/product/dram.php?ptype=view&prdcode=1706210029&catcode=111211&page=& (accessed 2024-10-21).

(72) Lee, Y. S.; Choi, D. won; Shong, B.; Oh, S.; Park, J. S. Low Temperature Atomic Layer Deposition of SiO2 Thin Films Using Di-Isopropylaminosilane and Ozone. *Ceram Int* **2017**, *43* (2), 2095–2099. https://doi.org/10.1016/j.ceramint.2016.10.186.

(73) Nam, T.; Lee, H.; Choi, T.; Seo, S.; Yoon, C. M.; Choi, Y.; Jeong, H.; Lingam, H. K.; Chitturi, V. R.; Korolev, A.; Ahn, J. H.; Kim, H. Low-Temperature, High-Growth-Rate ALD of SiO2 Using Aminodisilane Precursor. *Appl Surf Sci* **2019**, *485*, 381–390. https://doi.org/10.1016/j.apsusc.2019.03.227.

(74) Lee, Y.-S.; Han, J.-H.; Park, J.-S.; Park, J. Low Temperature SiOx Thin Film Deposited by Plasma Enhanced Atomic Layer Deposition for Thin Film Encapsulation Applications. *Journal of Vacuum Science & Technology A: Vacuum, Surfaces, and Films* **2017**, *35* (4). https://doi.org/10.1116/1.4985140.

(75) Bousiakou, L. G.; Karapetis, S. Determination of Au Film Thiolation and Silane Bonding onto SiO2 Films within the Frame of Biosensor Surface Functionalization - An Analysis of Best Practices and Techniques. *Croatica Chemica Acta*. 2020. https://doi.org/10.5562/CCA3640.

(76) Dahle, S.; Wegewitz, L.; Qi, F.; Weber, A. P.; Maus-Friedrichs, W. Silicon Dioxide Coating of Titanium Dioxide Nanoparticles from Dielectric Barrier Discharge in a Gaseous Mixture of Silane and Nitrogen. *Plasma Chemistry and Plasma Processing* **2013**, *33* (5). https://doi.org/10.1007/s11090-013-9472-6.

(77) Joo, S. Y.; Loka, C.; Jo, Y. W.; Reddyprakash, M.; Moon, S. W.; Choi, Y. S.; Lee, S. E.; Cho, G. S.; Lee, K. S. ITO/SiO2/ITO Structure on a Sapphire Substrate Using the Oxidation of Ultra-Thin Si Films as an Insulating Layer for One-Glass-Solution Capacitive Touch-Screen Panels. *Coatings* **2020**, *10* (2). https://doi.org/10.3390/coatings10020134.

(78) Yang, S.; Zhong, J.; Sun, B.; Zeng, X.; Luo, W.; Zhao, X.; Shu, Y.; Chen, J.; He, J. Influence of Base Pressure on Property of Sputtering Deposited ITO Film. *Journal of Materials Science: Materials in Electronics* **2019**, *30* (14), 13005–13012. https://doi.org/10.1007/s10854-019-01662-w.

(79) Joo, S. Y.; Loka, C.; Jo, Y. W.; Reddyprakash, M.; Moon, S. W.; Choi, Y. S.; Lee, S. E.; Cho, G. S.; Lee, K. S. ITO/SiO2/ITO Structure on a Sapphire Substrate Using the Oxidation of Ultra-Thin Si Films as an Insulating Layer for One-Glass-Solution Capacitive Touch-Screen Panels. *Coatings* **2020**, *10* (2). https://doi.org/10.3390/coatings10020134.

(80) Yang, J. H.; Baek, S. Bin; Kim, Y. C. Initial Surface Reaction of Di-Isopropylaminosilane on a Fully Hydroxyl-Terminated Si (001) Surface. *J Nanosci Nanotechnol* **2014**, *14* (10), 7954–7960. https://doi.org/10.1166/jnn.2014.9474.

(81) He, X.; Wu, J.; Wu, L.; Zhao, L.; Gao, X.; Li, X. Structure, Morphology and Optical Properties of SiO 2-x Thin Films Prepared by Plasma-Assisted Pulsed Laser Deposition. *Appl Surf Sci* **2008**, *254* (6), 1730–1735. https://doi.org/10.1016/j.apsusc.2007.07.127.

(82) Lee, K.; Shim, Y. First-Principles Study of the Surface Reactions of Aminosilane Precursors over WO3(001) during Atomic Layer Deposition of SiO2. *RSC Adv* **2020**, *10* (28). https://doi.org/10.1039/d0ra01635g.

(83) Lee, Y. S.; Choi, D. won; Shong, B.; Oh, S.; Park, J. S. Low Temperature Atomic Layer Deposition of SiO2 Thin Films Using Di-Isopropylaminosilane and Ozone. *Ceram Int* **2017**, *43* (2). https://doi.org/10.1016/j.ceramint.2016.10.186.

(84) Fang, H.; Liu, Q.; Feng, X.; Yan, J.; Wang, L.; He, L.; Zhang, L.; Wang, G. Carbon-Coated Si Nanoparticles Anchored on Three-Dimensional Carbon Nanotube Matrix for High-Energy Stable Lithium-Ion Batteries. *Batteries* **2023**, *9* (2). https://doi.org/10.3390/batteries9020118.

(85) Barr, T. L. An XPS Study of Si as It Occurs in Adsorbents, Catalysts, and Thin Films. *Applications of Surface Science* **1983**, *15* (1–4). https://doi.org/10.1016/0378-5963(83)90003-X.

(86) Prabhakaran, K.; Kobayashi, Y.; Ogino, T. Chemically Prepared Oxides on Si(001): An XPS Study. *Surf Sci* **1993**, *290* (3). https://doi.org/10.1016/0039-6028(93)90707-Q.

(87) Nyamtara, K. J.; Song, J. K.; Karima, N. C.; Kim, S. H.; Nguyen, M. C.; Duong, T. P. M.; Lee, K. J.; Ahn, W. Two Step Pyrolysis Synthesis Method of Graphite-Enhanced Nano-Si/Pitch Composite as Long Cycle Life Anode for Lithium-Ion Batteries. *J Alloys Compd* **2024**, *976*. https://doi.org/10.1016/j.jallcom.2023.173229.

(88) Huang, L.; Han, B.; Fan, M.; Cheng, H. Design of Efficient Mono-Aminosilane Precursors for Atomic Layer Deposition of SiO2 Thin Films. *RSC Adv* **2017**, *7* (37), 22672–22678. https://doi.org/10.1039/c7ra02301d.

(89) Park, T.; Kim, H.; Leem, M.; Ahn, W.; Choi, S.; Kim, J.; Uh, J.; Kwon, K.; Jeong, S. J.; Park, S.; Kim, Y.; Kim, H. Atomic Layer Deposition of Al2O3 on MoS2, WS2, WSe2, and h-BN: Surface Coverage and Adsorption Energy. *RSC Adv* **2017**, *7* (2). https://doi.org/10.1039/c6ra24733d.

(90) Girard, C.; Labani, B.; Vigoureux, J. M. Van Der Waals Induced Polarization of Physisorbed Atoms and Molecules: A Discrete Solid Theory. *Surf Sci* **1989**, *222* (1). https://doi.org/10.1016/0039-6028(89)90347-6.

(91) Zhang, H.; Chiappe, D.; Meersschaut, J.; Conard, T.; Franquet, A.; Nuytten, T.; Mannarino, M.; Radu, I.; Vandervorst, W.; Delabie, A. Nucleation and Growth Mechanisms of Al2O3 Atomic Layerdeposition on Synthetic Polycrystalline MoS2. *Journal of Chemical Physics* **2017**, *146* (5). https://doi.org/10.1063/1.4967406.

(92) Justin Kunene, T.; Kwanda Tartibu, L.; Ukoba, K.; Jen, T. C. Review of Atomic Layer Deposition Process, Application and Modeling Tools. *Mater Today Proc* **2022**, *62*. https://doi.org/10.1016/j.matpr.2022.02.094.

(93) Zhang, Y.; Lv, Q.; Fan, A.; Yu, L.; Wang, H.; Ma, W.; Lv, R.; Zhang, X. Reduction in Thermal Conductivity of Monolayer WS2 Caused by Substrate Effect. *Nano Res* **2022**, *15* (10). https://doi.org/10.1007/s12274-022-4560-7.

(94) Lee, T.-T.; Chiranjeevulu, K.; Pedaballi, S.; Cott, D.; Delabie, A.; Dee, C.-F.; Chang, E. Y. Nucleation and Growth Mechanism for Atomic Layer Deposition of Al2O3 on Two-Dimensional WS2 Monolayer. *Journal of Vacuum Science & Technology A* **2023**, *41* (1). https://doi.org/10.1116/6.0001913. WS2

(95) Kropp, J. A.; Cai, Y.; Yao, Z.; Zhu, W.; Gougousi, T. Atomic Layer Deposition of Al2O3 and TiO2 on MoS2 Surfaces. *Journal of Vacuum Science & Technology A: Vacuum, Surfaces, and Films* **2018**, *36* (6). https://doi.org/10.1116/1.5043621.

(96) Lv, W.; Liu, J.; He, Y.; You, J. Atomic Layer Deposition of ZnO Thin Film on Surface Modified Monolayer MoS2 with Enhanced Photoresponse. *Ceram Int* **2018**, *44* (18), 23310–23314. https://doi.org/10.1016/j.ceramint.2018.09.063.

(97) Wang, X.; Jiang, G. Q.; Yao, C. B.; Wang, Z. M.; Wang, L. Y.; Liu, Y.; Jiang, C. H. Excitonic Effects in the Linear and Nonlinear Optical Properties of ZnO@WS2 Heterojunction Films under Photoexcitation. *Optik (Stuttg)* **2022**, *260*. https://doi.org/10.1016/j.ijleo.2022.169096.

(98) Yanguas-Gil, A.; Yang, Y.; Kumar, N.; Abelson, J. R. Highly Conformal Film Growth by Chemical Vapor Deposition. I. A Conformal Zone Diagram Based on Kinetics. *Journal of Vacuum Science & Technology A: Vacuum, Surfaces, and Films* **2009**, *27* (5). https://doi.org/10.1116/1.3207745.

(99) Mak, K. F.; He, K.; Lee, C.; Lee, G. H.; Hone, J.; Heinz, T. F.; Shan, J. Tightly Bound Trions in Monolayer MoS 2. *Nat Mater* **2013**, *12* (3). https://doi.org/10.1038/nmat3505.

(100) Bianchi, M. G.; Risplendi, F.; Re Fiorentin, M.; Cicero, G. Engineering the Electrical and Optical Properties of WS2 Monolayers via Defect Control. *Advanced Science*. John Wiley and Sons Inc January 26, 2024. https://doi.org/10.1002/advs.202305162.

(101) Nan, H.; Wang, Z.; Wang, W.; Liang, Z.; Lu, Y.; Chen, Q.; He, D.; Tan, P.; Miao, F.; Wang, X.; Wang, J.; Ni, Z. Strong Photoluminescence Enhancement of MoS2 through Defect Engineering and Oxygen Bonding. *ACS Nano* **2014**, *8* (6). https://doi.org/10.1021/nn500532f.

(102) Kc, S.; Longo, R. C.; Wallace, R. M.; Cho, K. Surface Oxidation Energetics and Kinetics on MoS2 Monolayer. *J Appl Phys* **2015**, *117* (13). https://doi.org/10.1063/1.4916536.

(103) Shakya, J.; Kumar, S.; Mohanty, T. Role of Oxygen Adsorption in Modification of Optical and Surface Electronic Properties of MoS2. *J Appl Phys* **2018**, *123* (16). https://doi.org/10.1063/1.5023022.

(104) Luo, Z.; Zheng, W.; Luo, N.; Liu, B.; Zheng, B.; Yang, X.; Liang, D.; Qu, J.; Liu, H.; Chen, Y.; Jiang, Y.; Chen, S.; Zou, X.; Pan, A. Photoluminescence Lightening: Extraordinary

Oxygen Modulated Dynamics in WS2 Monolayers. *Nano Lett* **2022**, *22* (5). https://doi.org/10.1021/acs.nanolett.2c00462.

(105) Bianchi, M. G.; Risplendi, F.; Re Fiorentin, M.; Cicero, G. Addressing the Effects of Gas Adsorption on Monolayers beyond Charge Population Analysis: The Case of WS2. *NPJ Comput Mater* **2024**, *10* (1). https://doi.org/10.1038/s41524-024-01246-1.

(106) Pollmann, E.; Madauß, L.; Schumacher, S.; Kumar, U.; Heuvel, F.; vom Ende, C.; Yilmaz, S.; Güngörmüs, S.; Schleberger, M. Apparent Differences between Single Layer Molybdenum Disulphide Fabricated via Chemical Vapour Deposition and Exfoliation. *Nanotechnology* **2020**, *31* (50). https://doi.org/10.1088/1361-6528/abb5d2.

(107) Tsai, P. C.; Huang, H. C.; Huang, C. W.; Chang, S. J.; Lin, S. Y. Luminescence Enhancement and Dual-Color Emission of Stacked Mono-Layer 2D Materials. *Nanotechnology* **2020**, *31* (36). https://doi.org/10.1088/1361-6528/ab95b5.

(108) Bora, A.; Mawlong, L. P. L.; Mia, A. K.; Giri, P. K. Manipulating Trion and Biexciton Emissions in Monolayer WS2 by Sandwiching with Ultrathin ZnO Layers for Excitonic Light Emission Applications. *ACS Appl Nano Mater* **2024**, *7* (8), 8612–8623. https://doi.org/10.1021/acsanm.3c06043.

(109) Sunwoo, H.; Choi, W. Enhanced Performance of Multilayer MoS2 Transistors Encapsulated with a Photoresist. *Nanotechnology* **2021**, *32* (42). https://doi.org/10.1088/1361-6528/ac1542.

(110) Lin, Y.; Ling, X.; Yu, L.; Huang, S.; Hsu, A. L.; Lee, Y. H.; Kong, J.; Dresselhaus, M. S.; Palacios, T. Dielectric Screening of Excitons and Trions in Single-Layer MoS2. *Nano Lett* **2014**, *14* (10). https://doi.org/10.1021/nl501988y.

(111) Huang, Z. Improved Electrical Performance for Multilayer MoS2 Transistors by Using a Fully Encapsulated Al2O3 Dielectric Layer; 2018. https://doi.org/10.2991/iceep-18.2018.52.

(112) McCreary, K. M.; Hanbicki, A. T.; Singh, S.; Kawakami, R. K.; Jernigan, G. G.; Ishigami, M.; Ng, A.; Brintlinger, T. H.; Stroud, R. M.; Jonker, B. T. The Effect of Preparation Conditions on Raman and Photoluminescence of Monolayer WS2. *Sci Rep* **2016**, *6*. https://doi.org/10.1038/srep35154.

(113) Su, L.; Yu, Y.; Cao, L.; Zhang, Y. Effects of Substrate Type and Material-Substrate Bonding on High-Temperature Behavior of Monolayer WS2. *Nano Res* **2015**, *8* (8), 2686–2697. https://doi.org/10.1007/s12274-015-0775-1.

(114) Boryło, P.; Matus, K.; Lukaszkowicz, K.; Kubacki, J.; Balin, K.; Basiaga, M.; Szindler, M.; Mikuła, J. The Influence of Atomic Layer Deposition Process Temperature on ZnO Thin Film Structure. *Appl Surf Sci* **2019**, *474*. https://doi.org/10.1016/j.apsusc.2018.03.169.

(115) Kang, K. M.; Park, H. H. Effect of Atomic Layer Deposition Temperature on the Growth Orientation, Morphology, and Electrical, Optical, and Band-Structural Properties of ZnO and Fluorine-Doped ZnO Thin Films. *Journal of Physical Chemistry C* **2018**, *122* (1). https://doi.org/10.1021/acs.jpcc.7b08943.

(116) Wyndaele, P. J.; de Marneffe, J. F.; Sergeant, S.; de la Rosa, C. J. L.; Brems, S.; Caro, A. M.; De Gendt, S. Enhancing Dielectric Passivation on Monolayer WS2 via a Sacrificial Graphene Oxide Seeding Layer. *NPJ 2D Mater Appl* **2024**, *8* (1). https://doi.org/10.1038/s41699-024-00464-x.

(117) Cheng, L.; Qin, X.; Lucero, A. T.; Azcatl, A.; Huang, J.; Wallace, R. M.; Cho, K.; Kim, J. Atomic Layer Deposition of a High-k Dielectric on MoS2 Using Trimethylaluminum and Ozone. *ACS Appl Mater Interfaces* **2014**, *6* (15), 11834–11838. https://doi.org/10.1021/am5032105.

(118) Li, X. D.; Chen, T. P.; Liu, P.; Liu, Y.; Liu, Z.; Leong, K. C. A Study on the Evolution of Dielectric Function of ZnO Thin Films with Decreasing Film Thickness. *J Appl Phys* **2014**, *115* (10). https://doi.org/10.1063/1.4868338.

(119) Woo, W. J.; Oh, I. K.; Park, B. E.; Kim, Y.; Park, J.; Seo, S.; Song, J. G.; Jung, H.; Kim, D.; Lim, J. H.; Lee, S.; Kim, H. Bi-Layer High-k Dielectrics of Al2O3/ZrO2 to Reduce Damage to MoS2 Channel Layers during Atomic Layer Deposition. *2d Mater* **2019**, *6* (1). https://doi.org/10.1088/2053-1583/aaef1e.

(120) Price, K. M.; Schauble, K. E.; McGuire, F. A.; Farmer, D. B.; Franklin, A. D. Uniform Growth of Sub-5-Nanometer High-κ Dielectrics on MoS2 Using Plasma-Enhanced Atomic Layer Deposition. *ACS Appl Mater Interfaces* **2017**, *9* (27). https://doi.org/10.1021/acsami.7b00538.

(121) Schilirò, E.; Panasci, S. E.; Mio, A. M.; Nicotra, G.; Agnello, S.; Pecz, B.; Radnoczi, G. Z.; Deretzis, I.; La Magna, A.; Roccaforte, F.; Lo Nigro, R.; Giannazzo, F. Direct Atomic Layer Deposition of Ultra-Thin Al2O3 and HfO2 Films on Gold-Supported Monolayer MoS2. *Appl Surf Sci* **2023**, *630*. https://doi.org/10.1016/j.apsusc.2023.157476.

(122) Cho, J.; Kim, T.; Seegmiller, T.; Chang, J. P. Mechanistic Study of Atomic Layer Deposition of AlxSiyO Thin Film via In-Situ FTIR Spectroscopy . *Journal of Vacuum Science & Technology A: Vacuum, Surfaces, and Films* **2015**, *33* (5). https://doi.org/10.1116/1.4927318.